Modeling and Transient Analysis for the Pebble Bed Advanced High Temperature Reactor (PB-AHTR)

M.S. PROJECT REPORT
UCBTH-07-001

Alain Griveau

University of California at Berkeley
Department of Nuclear Engineering

Research Advisor: Per F. Peterson

A Élise

Table of contents

1. Introduction – General Description of the AHTR system

The Advanced High Temperature Reactor (AHTR) is an innovative reactor design that uses conventional TRISO high temperature fuel, but with a low-pressure liquid salt coolant rather than high-pressure helium [1]. This report presents design and analysis information on a pebble-fueled variant of the AHTR. The baseline 2400 MWt PB-AHTR design presented here has a 704°C core outlet temperature uses a well understood and qualified fuel (TRISO-based pebble fuel) and available ASME code qualified materials for all high-temperature components (Alloy 800H clad with Hastelloy N), to prevent the need for any materials and fuel development programs. Power up-rates to 3600 MWt and 4800 MWt are also studied, as well as a high-temperature 2400 MWt version with a 859°C core outlet temperature.

The primary advantages of the AHTR involve the ability to operate at higher power density than helium cooled high temperature reactors while achieving comparable power conversion efficiency, as shown in Fig. 1-1, which creates the potential for substantial reductions in the plant capital cost. Likewise, the lower neutron leakage provided by the large PB-AHTR core allows improved fuel utilization, reduced spent fuel generation, and lower fuel cycle costs than those for modular helium reactors.

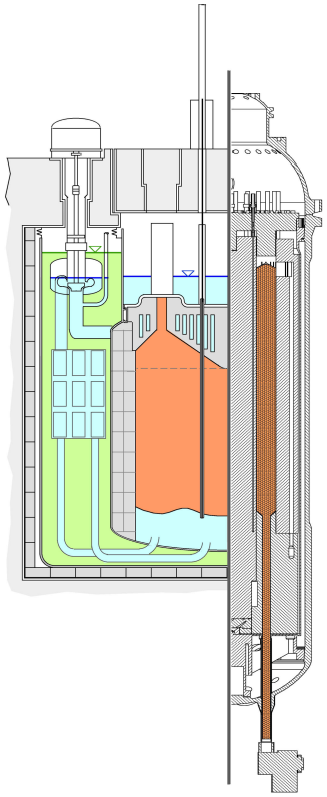

2400-4800 MWt PB-AHTR **400 MWt PBMR**

Figure 1-1: Scaled comparison of the 2400 MWt (with possible power up rate to 4800 MWt) PB-AHTR, with the 400 MWt PBMR.

This report reviews the major features of the AHTR design, identifies key operating and accident transients that the AHTR must be designed to accommodate, selects the safety related parameters to be predicted in modeling these transients, and presents RELAP5-3D models and modeling results for these transients. This chapter provides an overview of the various concepts for Generation IV high temperature reactors, and then introduces the PB-AHTR and identifies the transients that the PB-AHTR should be designed to accommodate.

A. Review of Gen IV high temperature reactors concepts

To replace the current fleet of Gen II/III reactors and the Gen III+ reactors that will be built in the near term, a broad range of reactors concepts are currently investigated under the auspices of the Gen IV International Forum (GIF), as Fig. 1-2 illustrates. All these concepts can broaden the opportunity of use of nuclear energy and therefore share at one or more of these primary goals [2]:

- Economics: reduced capital and energy production costs, diminution of financial risks, possibility of production of hydrogen, process heat, desalinated water and other products
- Safety and Reliability: improved safety systems, minimization of off-site consequences, higher reliability minimizing costs
- Sustainability: better fuel utilization, minimization of waste, effective use of resources
- Proliferation resistance and physical protection: minimization of the risks of diverting weapons-usable material from any point of the fuel cycle, and theft of materials or radiological sabotage of facilities.

The different Gen IV concepts are classified according to their coolants. To introduce the AHTR design, three reactor concepts that provide the technological underpinnings for the AHTR are discussed first in the next sections.

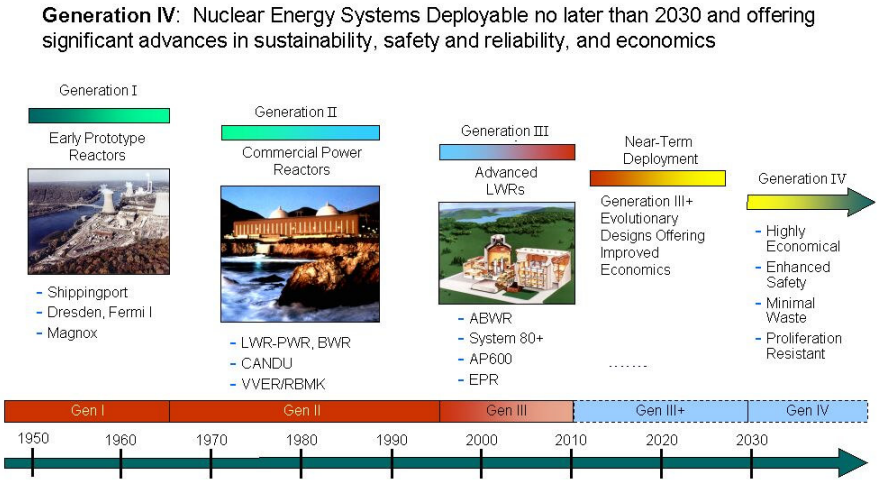

Figure 1-2: Evolution of nuclear energy systems, from Generation I to IV

1) Molten salt reactor (MSR)

The first prototypical molten salt reactor was the Aircraft Reactor Experiment, which began to operate in 1954. It was a 2.5 MW_{th} molten-salt fueled reactor designed to attain a sufficiently high power density to be usable as an aircraft engine. It used a molten fluoride salt NaF-ZrF_4-UF_4 as a fuel and was moderated by BeO: its peak temperature was 860ºC.

Subsequent efforts to develop a commercial MSR were carried on by ORNL in the form of the Molten Salt Reactor Experiment, which was a 7.4 MW_{th} molten-salt fueled reactor and went critical in 1965. The fuel was LiF-BeF_2-ZrF_4-UF_4, the core was moderated by graphite and 2LiF-BeF_2 (flibe) was used as a secondary coolant. Its peak temperature was 650ºC.

The U.S. MSR program developed code qualified materials (Hastelloy N) for use with molten salts, performed extensive corrosion and materials compatibility testing between graphite and metallic materials and molten salts, measured salt thermophysical properties, demonstrated long-term pump operation with molten salts, and developed designs for prototypical scale pumps and other primary loop components.

The MSR is still investigated as a part of the Gen IV International Forum [3]. It is important to remark that all these concepts relied on a fuel dissolved in a liquid salt coolant. This fuel form gives several advantages, such as online refueling and reprocessing, but also introduces several issues, such as corrosion, since the primary coolant and the fuel are in the same homogeneous mixture. The PB-AHTR uses liquid salts (this designation emphasizes that the salts are clean, rather than having dissolved fuel), for which corrosion rates are known to be very low with the materials used in the PB-AHTR (graphite and Hastelloy N cladding).

2) Helium cooled very high temperature reactor (VHTR)

There has been a recent resurgence of interest for helium cooled high temperature reactors, with for instance the commissioning of the pebble bed research reactor HTR-10 in China in 2002 and the operation of the 30 MW_t hexagonal fuel block HTTR in Japan since 1998. These research programs were built on the experience gained by previous reactor experiments such as Fort Saint-Vrain in the US from 1976 to 1989 and the THTR-300 in Germany from 1983 to 1989.

These recent designs are all based on TRISO particle fuels, which limit greatly the release of fission products even at temperatures greater than 1600ºC (see for instance [4] and [5]). These small TRISO particles have traditionally been formed into either 6 cm graphite-layer pebbles or cylindrical compacts inserted into larger hexagonal graphite fuel blocks.

New commercial scale HTRs use modular designs, which allow passive decay heat removal following loss of coolant accidents, via conduction heat transfer to the reactor vessel. Examples include the Pebble Bed Modular Reactor, which is planned to be built in South Africa starting in 2007, or the General Atomics GT-MHR, which is one of the designs being considered for the Next Generation Nuclear Plant project. Also of

interest for HTRs are the studies on the Gas cooled Fast Reactor, which also continue in the framework of the Gen IV efforts.

3) Sodium fast reactor (SFR)

The sodium fast reactor is similar to the AHTR because it uses a low volatility liquid coolant and operates at relatively high temperatures (but significantly lower than the AHTR). Many SFRs use large coolant pools like the AHTR, such as the EBR-II, S-PRISM, Superphenix, and European Fast Reactor. Thus these reactors share many similarities with the AHTR, in particular in potential approaches to decay heat removal, including Reactor Vessel Auxiliary Cooling System (RVACS) and Direct Reactor Auxiliary Cooling System (DRACS), where a DRACS has been selected for the AHTR.

Likewise, several key area of difference exist between the SFR and the AHTR. These include the much higher volumetric heat capacity of liquid salts compared to sodium which results in pumps, primary piping, and heat exchangers being more compact in the AHTR; the opacity of sodium compared to the transparency of liquid salts, which complicates in service inspection; and the high chemical reactivity, which requires that SFR reactors and containment structures be designed to sustain strong pressure pulses from rapid chemical reactions with water and air that cannot occur with liquid salts.

B. The Pebble-Bed Advanced High Temperature Reactor (PB-AHTR)

The Advanced High Temperature Reactor is a high-temperature reactor that uses conventional TRISO coated particle fuel together with a liquid fluoride salt coolant. The initial AHTR design followed closely an earlier sodium-pool reactor design, the S-PRISM, but used liquid salt as the coolant (see [1]). Some simplified thermal hydraulics studies were performed for several variations of this early design, including using hexagonal fuel blocks similar to those in the GT-MHR [6], as well as a pebble-bed design [7].

All these previous studies used a Reactor Vessel Auxiliary Cooling System (RVACS) to remove decay heat in case of a loss of forced cooling, where decay heat is removed from the reactor vessel surface to a reactor cavity cooling system. More recently, UC Berkeley introduced a design update that made several key changes to this earlier preliminary design [8]. The work presented here stems from this effort to make the passive decay heat removal system more modular and robust: this is done by using a modified modular Direct Reactor Auxiliary Cooling System (DRACS). More precisely, the current design uses a closed primary loop immersed in a separate buffer salt tank: with this configuration, the AHTR shares many similarities with pressurized water reactors (PWRs) and gains some important advantages compared to the open-loop approach based on sodium fast reactor designs.

1) Overview of the current AHTR design

The flow diagram in Fig. 1-2 provides a simple overview of the current 2400 MWt baseline PB-AHTR design. The primary loop is represented by a line flowing between the core and the Intermediate Heat exchanger (IHX) modules. The primary loop has a core outlet temperature of 704°C and is built with ASME code qualified metallic components; hence the design has been named the AHTR-MI (Metallic Internals). This design minimizes the inventory of the relatively expensive primary salt and permits an inexpensive sodium fluoroborate buffer salt to be used outside of the primary loop, which provides additional cooling and thermal inertia without neutronics constraints.

During steady state operation, the primary loop operates in forced circulation (with a baseline flow rate of 9200 kg/s) using 4 primary pumps that take primary coolant from the core outlet plenum. Table 1-1 shows the resulting pump design [8], which has a similar specific speed as typical PWR primary pumps and thus similar potential impeller designs, but which are physically smaller and require significantly less power than a corresponding PWR pump for the same net reactor electrical power output. On the other hand, this pump must operate in a similar environment to pumps designed for the MSR, which allows a pump previously designed for the earlier ORNL Molten Salt Breeder Reactor (MSBR) project to be used for the AHTR-MI.

To cope with the large power output of the reactor, high power density Heatrix-type compact heat exchangers are used for the intermediate heat exchangers (IHXs). Eight similar IHX modules are coupled to the four primary pumps, and occupy 49 m^3 in

the buffer salt, yielding a power density of 50 MW/m^3 and a log mean temperature difference of 30ºC.

During a loss of forced cooling (LOFC) transient (i.e. after a primary pump trip), a natural circulation flow loop is formed between the hot core and a set of Pool Reactor Auxiliary Cooling System (PRACS) heat exchangers (PHX modules), first suggested by Forsberg [9]. During forced cooling the PRACS flow path is partially blocked for reversed flow by passive fluidic diodes, which have much larger loss coefficients (K values) for reversed versus forward flows (up to a factor of a few hundred).

The eight PHX modules use conventional tube bundles with a square tube lattice, which transfer heat from the primary salt to the large volume of buffer salt in the tank (see Fig. 1-4 for an elevation view and Fig. 1-5 for a top view of the PB-AHTR). Baffles are used around the PHX in the buffer salt side to create a chimney effect and enhance natural circulation mixing in the buffer tank.

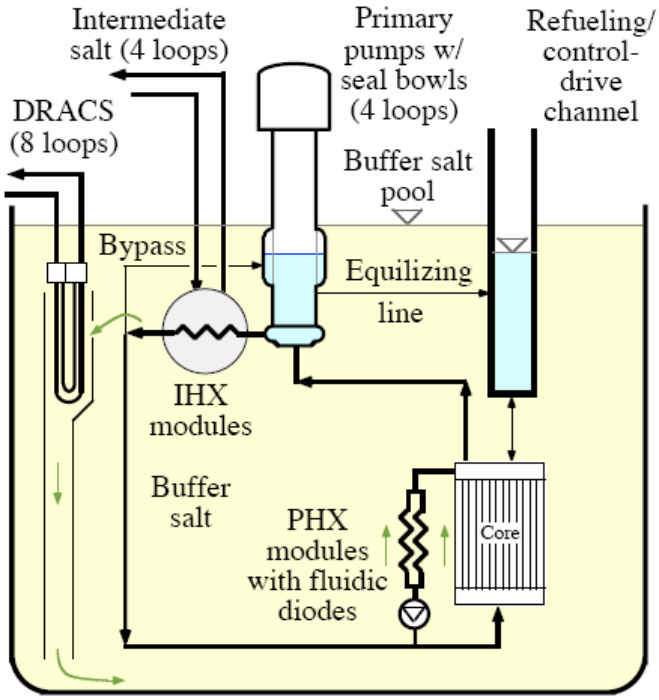

Figure 1-3: Simplified flow diagram of the AHTR-MI (hexagonal fuel), from [8]

The buffer salt is cooled by a set of eight DRACS heat exchanger modules, which are similar in design to the PHX system. The DRACS heat exchangers transfer heat by natural circulation flow from the buffer salt to heat exchangers cooled by outside ambient air; they are sized to match decay power within approximately 24 hours after scram. This type of DRACS design was used in EBR-II in Idaho, and has also been adopted for the European Fast Reactor (EFR).

Further details and design parameters for the current baseline thermal hydraulics design of the AHTR can be found in Tables 1-1 and 1-2, and Annex A gives a complete table of design parameters relevant to the LOFC transients.

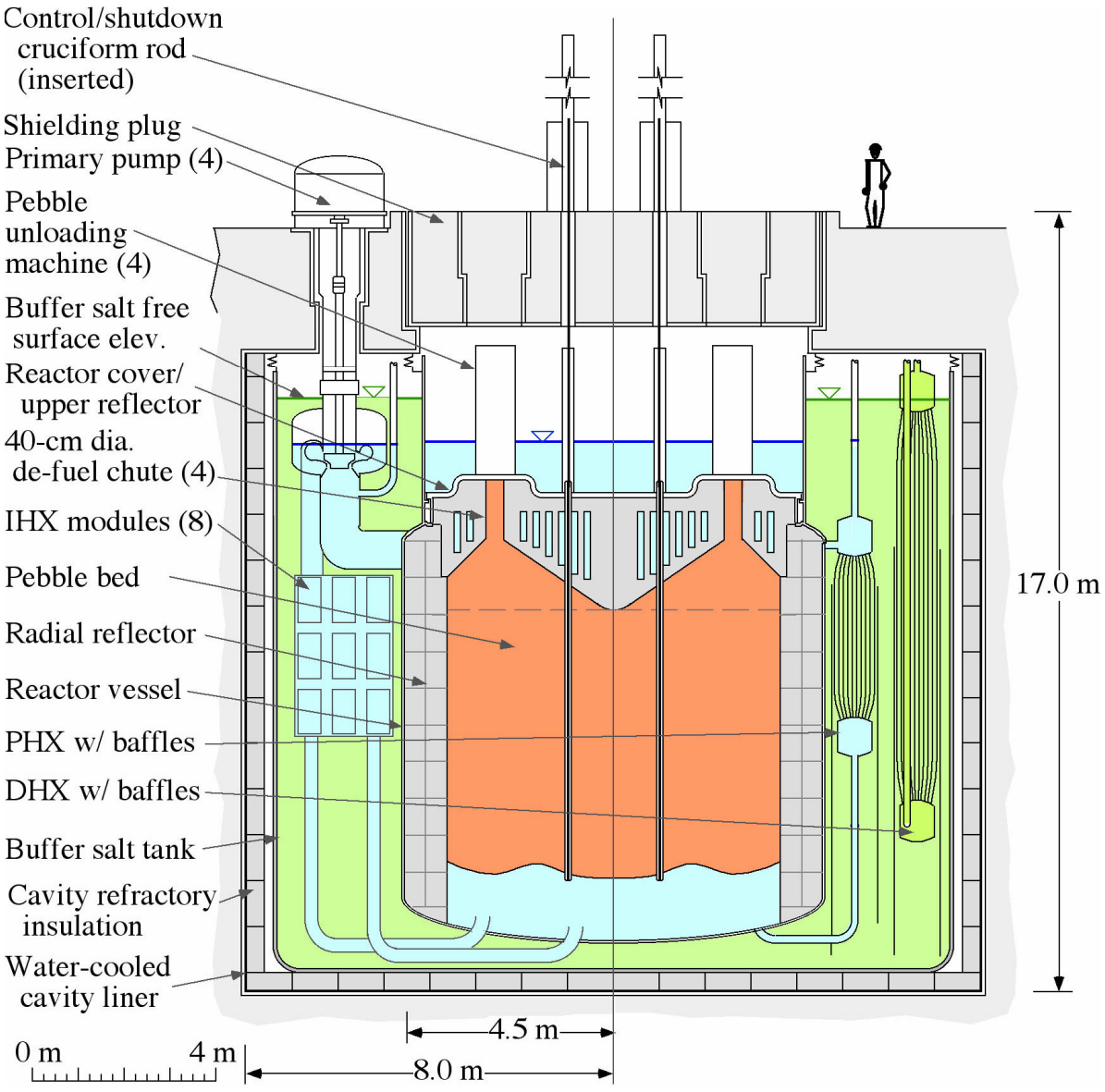

Figure 1-3: Elevation view of the Pebble Bed AHTR, on the left the loop used during forced circulation, on the right the PRACS/DRACS system, from [8]

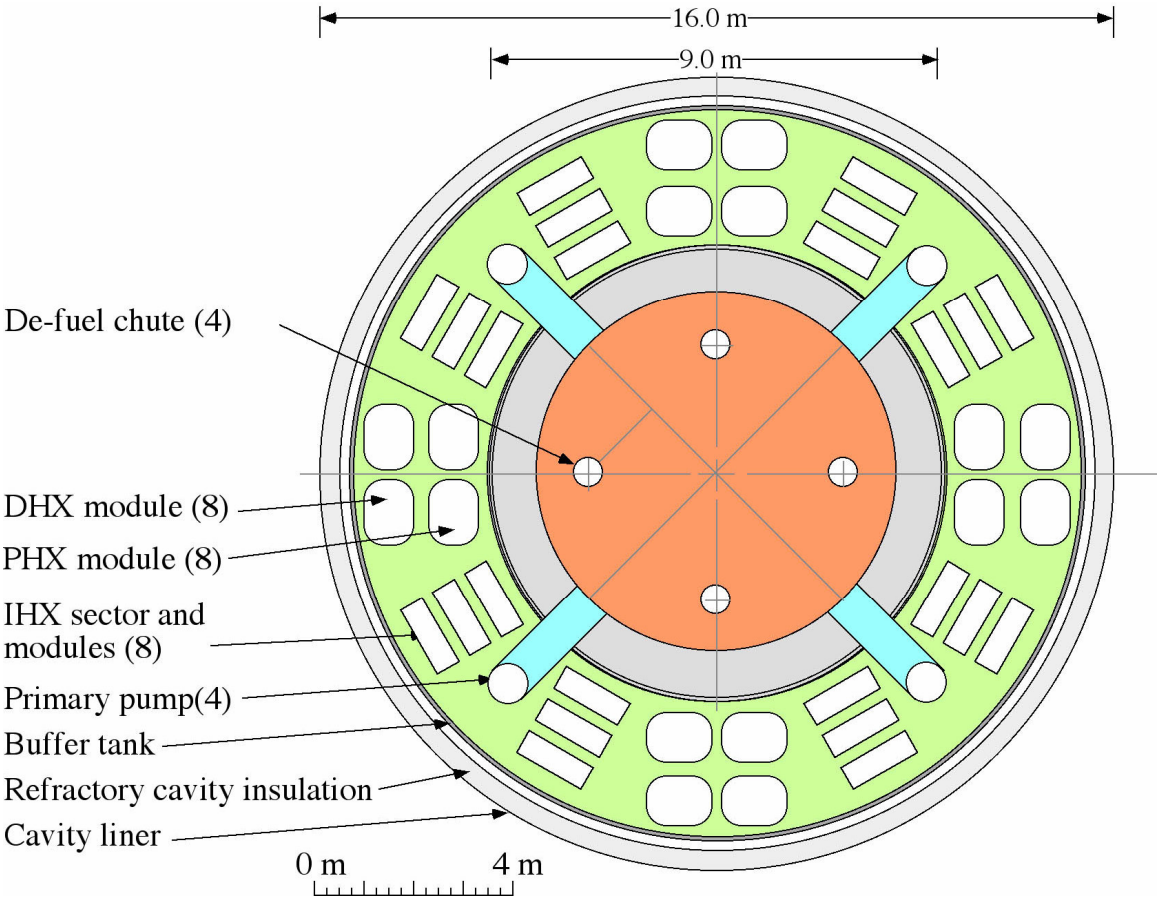

Figure 1-5: Plan view of the primary components in the buffer tank, from [8]

Thermal Power	2400 MW_t
Inlet temperature	600ºC
Outlet temperature	704ºC
Core power density	10.2 MW/m^3
Primary mass flow	9200 kg/s
Primary pump head	20 m
Primary pump specific speed	4500 rpm $(1/s)^{1/2}m^{-3/4}$
Pumping power	1.5 kW/MW_t
IHX power density	50 MW_t/m^3

Table 1-1: Key characteristics of the primary loop elements used during steady state operation

PHX length	3.2 m
DHX length	6.4 m
PHX/DHX pipe d/pitch	2.5 cm/3.5 cm
PHX/DHX pipes #	4000
PHX/DHX total horizontal footprint	4.9 m^2
PHX total heat transfer area	1005 m^2
DHX total heat transfer area	2010 m^2

Table 1-2: Key characteristics of the passive safety system used during LOFC transients

2) Liquid salt coolants and their advantages

Using clean liquid salt as a primary coolant provides several advantages at high temperatures compared to other available heat transfer fluids. From the perspective of thermal hydraulics, liquid salts have high volumic heat capacity, allowing substantially more compact equipment designs that possible with helium or sodium.

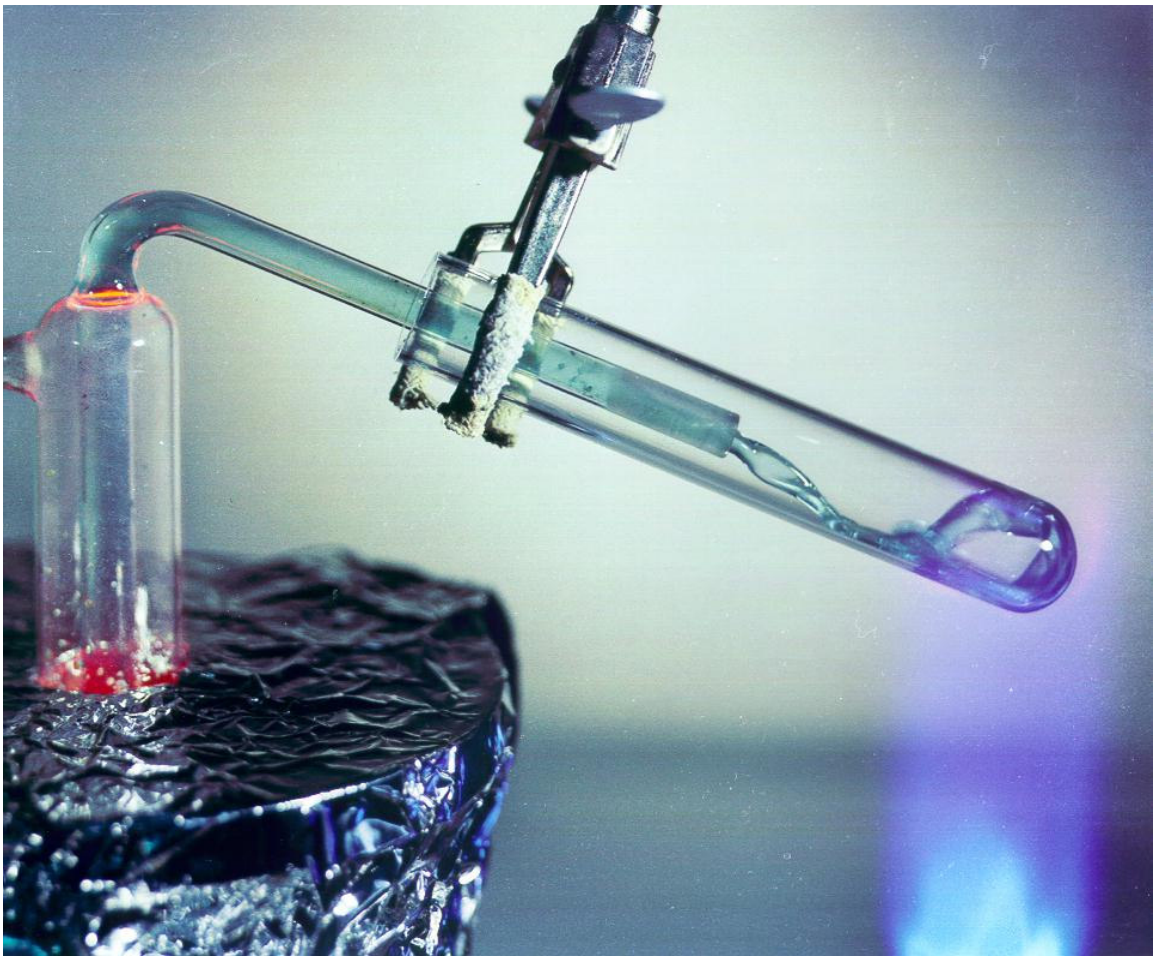

Figure 1-6: Liquid flibe heated in air, flowing in a test tube

Their high boiling point (>1300ºC) permits operation at temperatures that are only limited by material constraints (600 - 980ºC for candidate metallic materials), which yields improved thermodynamic efficiency. Table 1-3 contrasts the thermophysical properties of flibe with those of other coolants such as water, helium and sodium.

Liquid fluoride salts have very low chemical reactivity with air and water in this temperature range, and are compatible with graphite and several nickel-based alloys. As shown in Fig. 1-6, they also are transparent to visible light, allowing for optical in-service inspection.

	Flibe	Water	Sodium	Helium
$T\ (°C)$	700	300	550	700
$p\ (bar)$	1	150	1	100
$\rho C_p\ (MJ/m^3K)$	4.65	3.97	0.99	0.026
$k\ (W/mK)$	1.1	0.54	62	0.35
$\nu.10^7\ (m^2/s)$	28	1.2	2.8	91
Pr	13	0.86	0.004	0.67

Table 1-3: Thermophysical properties of selected primary coolants at their typical temperature of use (from [10] **and** [11])

Recent investigation by ORNL [10] has shown that, of all the possible salt mixtures, flibe (2^7LiF-BeF_2) is a good candidate as a primary coolant due to its superior heat transfer capabilities. This comparison was done using several figures of merit that sum up the behavior of the salts under different conditions, such as forced convection and laminar or turbulent natural convection (excerpts shown Table 1-4). Furthermore, flibe can also show interesting neutronics properties, if the lithium is enriched with more than 99.995% ^{7}Li, thanks to a large moderating ratio ($\xi\Sigma_s/\Sigma_c$) and small coolant parasitic capture probability.

	2^7LiF-BeF_2	NaF-BeF_2	NaF-ZrF_4	^{7}LiF-NaF-ZrF_4
Forced convection	**0.7**	0.91	1.82	1.42
Size of heat exchanger	**21.5**	25.2	37.4	35.9
Laminar natural convection	10.12	13.45	**7.9**	9.01
Forced natural convection	**13.9**	16.5	14.7	**13.9**
Moderating ratio	**60**	15	10	13
Coolant parasitic capture	**8**	28	24	20

Table 1-4: FOM for a short list of possible primary salts. For the thermal hydraulics FOM, smaller values are better, higher moderating ratios are better, and smaller parasitic capture is better (from [10])

Other favorable properties of flibe include low vapor pressure and the possibility of using redox buffers to maintain a highly reducing environment in this salt and keep a very low corrosivity. However, flibe also has several drawbacks, a main one being its high cost of production: because of the presence of highly enriched ^{7}Li, estimates of the price per liter are $50-100, which means that the primary coolant could contribute to a significant part of the costs of construction. Another concern is the toxicity of the beryllium in the salt, although in a nuclear facility where contamination by leakage of

radioactive primary coolant would be controlled in any case, the additional cost and difficulty of beryllium safety controls is likely to be acceptable.

The binary mixture NaF-$NaBF_4$ (8-92) was chosen for the buffer salt due to its favorable heat transfer capabilities and low cost. It also has the attractive properties of containing boron and having lower density than flibe at their respective operating temperatures (see Table 1-5), reducing the possibility of positive buoyancy on the primay loop components. The boron contained in the buffer salt means it can provide mitigation in case of a breach of the reactor vessel, as a boron-rich salt will tend to be injected into the core and the strong neutron capture in boron will assure subcriticality. For the intermediate loop the liquid salt flinak (LiF/NaF/KF) is selected as the baseline salt due to its excellent thermophysical properties and low vapor pressure.

Liquid salts are also of interest as a potential fluid for the NGNP/National Hydrogen Initiative intermediate heat transfer loop. Another ORNL report [12] identifies flinak as the most promising salt in term of heat transfer performances (as selected for the AHTR baseline), while $MgCl_2$-based salts may provide sufficiently good or even superior properties for a much lower cost.

Table 1-5 provides a summary of the relevant thermophysical properties for these liquid salts. Furthermore, as pointed out by Hauk [11], most of these salts display very high Pr, for which heat transfer studies are lacking. This could be an important factor, as significant buoyancy effects may affect flows treated with forced convection correlations. However, experiments to study this mixed convection heat transfer can be done with relative simplicity and low cost using heat transfer oils as simulant fluids.

	Melting point (ºC)	Density (g/cm^3)	Heat capacity (J/kg K)	Viscosity (cP)	Th. conductivity (W/m K)	Pr (at T=600º C)
LiF-BeF_2 (66-34)	458	$2.28-4.884E-4\times T$	2380	$0.116\exp\left(\frac{3755}{T+273}\right)$	1.1	20.4
NaF-$NaBF_4$ (8-92)	385	$2.2521-7.11E-4\times T$	1500	$0.0877\exp\left(\frac{2240}{T+273}\right)$	0.5	3.4
LiF-NaF-KF (flinak)	454	$2.53-7.3E-4\times T$	1880	$0.04\exp\left(\frac{4170}{T+273}\right)$	1	10

Table 1-5: Summary of properties of the salt used in the current design (T is in ºC)

3) Possible fuel geometries for a liquid salt cooled reactor

Three different fuel forms have been studied for potential application to the AHTR. They all fit into the 6.8 m diameter, 6.4 m high active core volume of the baseline design, and operate at power densities around 10.2 MW/m^3, compared to around 6.5 MW/m^3 for typical helium cooled HTRs. This is larger than the MSBR reactor design, but is a similar geometry, so that most of the reflector/plenums geometry can be taken out from this previous design.

Hexagonal fuel blocks with embedded TRISO particles

This was the design that was first proposed for the AHTR [1], and it followed closely the previous examples of helium cooled reactor such as the HTTR or the GT-MHR concepts. Fig. 1-7 illustrates the principle of such fuel forms. This fuel can be considered on three different scale levels:

– the approximately 0.5-mm diameter TRISO particles (acronym for Tri-Structural Isotropic). They can use various fuel compositions (U, Pu or TRU), as well as a wide range of enrichments (typically up to 20%). They are typically composed of oxide or oxi-carbide fuel, pyrolitic carbon and silicon carbide layers, for instance as shown in Table 1-6.

Layer	Fuel kernel	Porous C	Pyrolitic C	SiC	Pyrolitic C
Radius (mm)	0.25	0.34	0.38	0.42	0.45
Density (g/cc)	10.5	1.0	1.85	3.16	1.85

Table 1-6: Typical TRISO particle geometry and composition

Figure 1-7: Prismatic fuel from 0.5 mm TRISO particles to the hexagonal fuel blocks (from [13])

– these particles are put into a graphite matrix of density of approximately 1.7 g/cc formed into cm scale cylindrical fuel elements
– fuel elements are inserted into large graphite hexagonal blocks, which play the role of moderator. More precisely, they are fitted in an hexagonal honeycomb-like configuration:

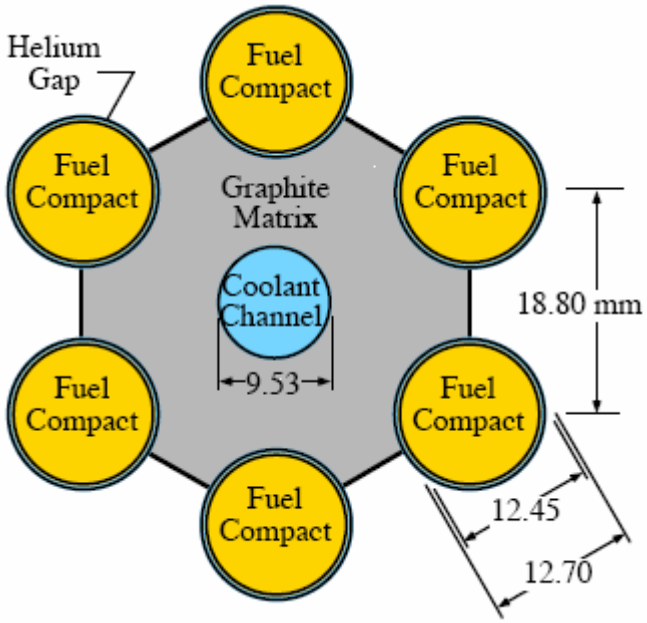

The liquid salt primary coolant flows in 0.953-cm channels (baseline design from [13]) situated at the center of the hexagonal unit cell.

The prismatic fuel form has several advantages, including its relative similarity to a known design, used in the Fort Saint-Vrain reactor. Thus, control rods and reserve shutdown channels can be taken from this previous project [8]. On the other hand, prismatic has two main drawbacks: first, the relative complexity of defueling and refueling operations, when a major fraction of the $325 \times 8 = 2600$ graphite blocks must be taken out of the core. Second, given the relatively low density of graphite, the average density of the fuel element materials is around 1.72 g/cc, which means the fuel elements would typically float in flibe coolant at 700ºC ($\rho = 1.94$ g/cc). This likely requires that the blocks be ballasted with a heavier material like zirconium, which introduces difficult trade-offs with neutronics efficiency and fuel element design.

Stringer fuel

This design uses cylindrical UO_2 fuel pellets enclosed in metallic or carbon-carbon composite clad material. According to recent design effort by Areva NP for a metallic-clad fuel pin design [14], these fuel pins could have a radius of 0.483 cm, similar to PWR pins. They are placed in clusters around into a coolant channel (yellow color in Fig. 1-8), forming a fuel assembly. These fuel assemblies are then organized in a square or circular array surrounded by moderator blocks.

This configuration has some advantages over the prismatic fuel blocks: first, it minimizes the volume of material taken out during refueling and probably allows for on-line refueling, as the assemblies are the only removable parts in this design. Second, this pin fuel form is much more common in the industry than the prismatic fuel, although some uncertainties remain on the material selection for the cladding around the pellets, because the zirconium commonly used for light water reactor fuel corrodes readily in liquid salts. Thus it is likely that a large fuel development and qualification process will be needed that may be quite time consuming, and if iron is used in the cladding, a significant neutronics penalty may occur. Most important is the fact that the stringer fuel design solves the buoyancy problem of the prismatic blocs, because the moderator graphite can be securely fastened in the core, and the removable assemblies are then much denser than the coolant.

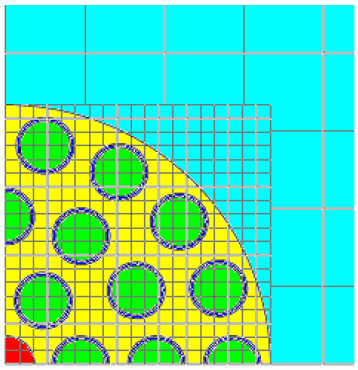

Figure 1-8: Cluster of fuel pins (green & blue cylinders), into a coolant channel (yellow). These clustered assemblies are separated by fixed graphite moderator blocks (cyan). From [14]

`*Pebble fuel*

The pebble fuel geometry shares the same TRISO particles with the hexagonal blocks fuel. Depending on the desired fuel loading in one pebble, TRISO particles are embedded in a graphite matrix with a given packing fraction to obtain a 2.5 cm radius spherical fuel zone, which is protected by a 0.5-cm thick coating of graphite (see Fig. 1-9).

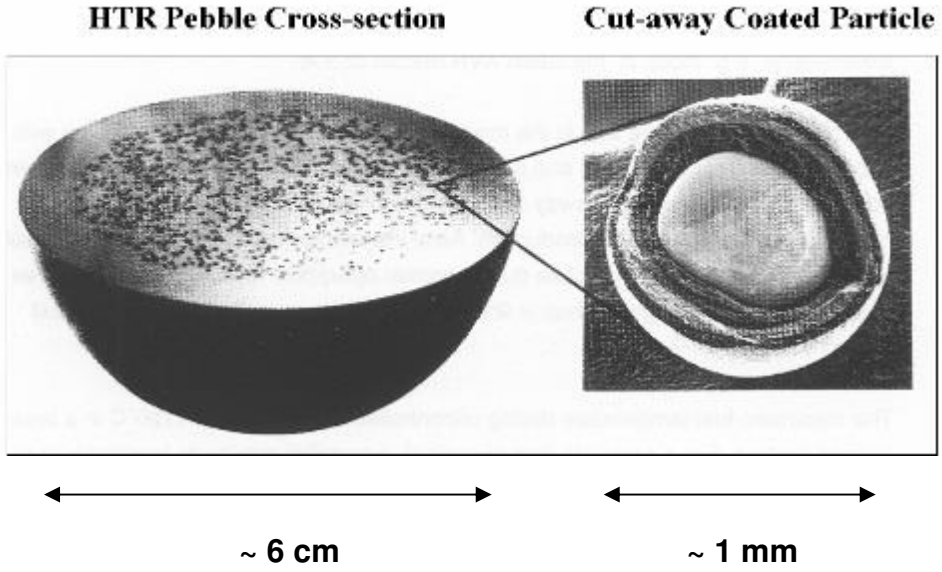

Figure 1-9: Pebble fuel [15]

The resulting pebbles are assembled into a randomly packed bed; in the 2400 MW_t PB-AHTR design, there are typically around 1.2 million pebbles in the active core. Because this design is fitted for online refueling, pebble injection ports and pebble defueling chutes are included into the bottom inlet and top outlet plenums designs (as shown in Fig. 1-4). As the pebbles have positive buoyancy in flibe, the locations of these injection and defueling systems are reversed compared to the helium cooled pebble bed reactor (e.g. the PBMR), meaning the injection ports are at the bottom of the reactor in the inlet plenum, and the pebbles "defueling chutes" are at the top in the outlet plenum.

Compared to the hexagonal fuel, this pebble-bed option provides a more flexible refueling approach, but raises several issues that require study, such as the neutronics behavior of pebble fuel cooled with flibe, pebble recirculation methods and dynamics, as well as the correct thermohydraulic correlations to be used for heat transfer and pressure drop in the pebble bed for fluids with high Prandtl number like liquid salts. The neutronics and thermal hydraulics study reported here focuses on this pebble-bed variant of the AHTR design, including review of the design parameters and initial results from the scaled Pebble Recirculation Experiment (PREX), which has demonstrated the viability of pebble recirculation in the PB-AHTR.

C. Scope of this study – CSAU framework

1) The Code Scaling, Applicability, and Uncertainty methodology

At the end of the 1980's, the US Nuclear Regulatory Commission decided to allow the use of best estimate methods with uncertainty quantification for reactor safety analysis, in lieu of the earlier licensing practice that used deterministic methods with conservative assumptions to address uncertainties. To have a reliable estimate of the overall uncertainty of the models used for best estimate licensing, the NRC imposed a requirement for systematic estimation of all sources of uncertainty. The Code Scaling, Applicability, and Uncertainty methodology is a systematic approach proposed by the NRC that can be used to identify and quantify these uncertainties.

This approach has been successfully used in many aspects of analysis of the safety of light water reactors. The CSAU method was first used in efforts to better understand severe accidents, and subsequently was applied to large break loss of coolant (LB-LOCA) accidents, and according to Levy [16] led to "an increased understanding of complex two-phase flow phenomena involved." Likewise CSAU was used in the conception and design of the ESBWR, so that the pre-certification review of the NRC and the associated approval of codes and supporting experiments only took 6 months.

The CSAU method fits well in the objectives of the Generation IV Roadmap, by providing a better approach to safety estimation, and by providing a systematic process to identify separate effect test (SET), integral effect test (IET), and component test (CT) experiments that are required to develop and license a given reactor design. CSAU has been used in several innovative reactor designs both by US national laboratories and vendors, where the helium cooled VHTR concept offers a good example of such efforts [17]. The NRC is currently recommending CSAU as the method to tackle design certification for non-water cooled reactors, as stated in its policy issue information [18].

Figure 1-10 provides an overview of the different steps of the CSAU methodology. This study focuses on the top half of this flowchart, from step 1 to 8. More precisely:

- steps 1-3 represent the definition of a Phenomena Identification & Ranking Table (PIRT) for a chosen scenario. This involves addressing the correct phenomena when modeling the system: it is therefore closely related to the design of an adapted scaled IET to provide integral test data for model validation. Here it is important to note the methods for systematically identifying scenarios for operating and accident transients do not as yet exist; in this study for the PB-AHTR a systematic approach was developed to select the two transients studied
- steps 4-5 determine the basis of the code applicability by looking at the validity of the physical models in the particular situation of the scenario. Separate Effect Tests (SET's) can be used to assess the validity of these models, for instance by testing the agreement of a correlation used in the code with experimental data at relevant physical conditions.

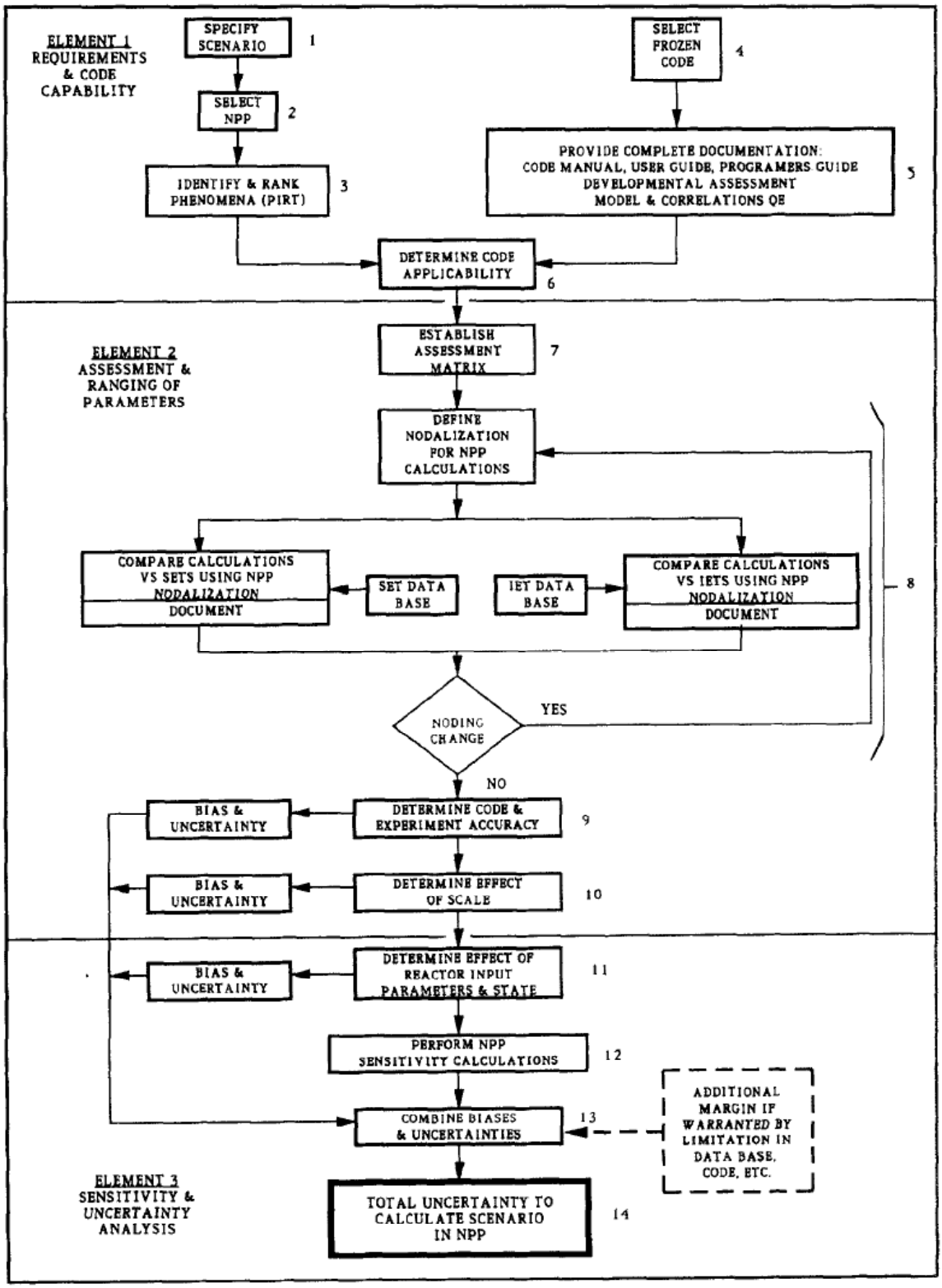

Figure 1-10: CSAU methodology (from [16])

- steps 6-8 concern the beginning of the construction of a numerical model to simulate the transient, and the comparison of results with IET/SET data. In this case, due the early stage of development of the AHTR concept, this numerical model will mainly provide an estimation of the viability of the design and an assessment of some possible optimization, but cannot yet be compared against IET data because such data is not yet available. Chapter 3 of this report provides a brief summary and two examples of approaches to the design of SET's and IET's using simulant fluids that would be relatively inexpensive and would enable PB-AHTR model validation to support licensing of the PB-AHTR.

In summary, this report uses the CSAU method as a framework to assess experimental needs and create an adapted numerical description for two key scenarios for assessment of the safety of the PB-AHTR pebble-bed safety system design.

2) The role of Loss of Forced Cooling (LOFC) transients

The current PB-AHTR design provides in the primary system four successive physical barriers which isolate the fuel and its byproducts from the environment:

- The TRISO particles and in particular the successive layers of carbon and ceramics around the fuel kernel. According to [19], the failure mechanism at high temperature starts with the decomposition of the SiC layer, followed by the diffusion of fission products such as Cs, Xe, Kr or iodine through the underlying PyC layer. [3] gives a temperature of 1600ºC as the onset of Cs diffusion out of failed TRISO particles for irradiated fuel developed for the Japanese HTTR test reactor. This estimation is confirmed by [5] which post-irradiation heating experiments on fuel developed by the German program give less than one TRISO particle failure per pebble at 1600ºC. In general, peak fuel temperatures under transients and accidents are several hundred degrees lower than this in the PB-AHTR.

- The liquid salt coolant, which has a high capacity to absorb most fission products that might be released from the fuel.

- Metallic alloy components that form the primary loop boundary. For high-temperature primary loop components, the baseline PB-AHTR design uses Alloy 800H clad with Hastelloy N to provide corrosion resistance, which limits the maximum acceptable temperature to 980ºC, according to ASME code. In practice, it is preferable to design for lower peak reactor outlet temperatures, due to the very low strength of Alloy 800H at high temperature.

- The reactor containment building, designed to limit the release of any radionuclide exiting the primary system. For the AHTR the containment design is simplified due to the lack of stored energy sources (chemical reactions, high pressure fluids, steam explosions) that could generate significant internal pressures in the AHTR.

Furthermore, it is undesirable to have the temperature of the salt exceeding its boiling point (nominally 1400ºC in Flibe). These three constraints translate into three temperature limits for operational transients and accidents in this reactor design:

$$T_{fuel} < 1600ºC \quad T_{outlet} < 980ºC \quad T_{flibe} < 1400ºC$$

The boiling limit on the flibe temperature may be redundant with the limit on the outlet coolant temperature, as the outlet is expected to be the location where the flibe coolant has its peak temperature.

One transient that can cause increased coolant and fuel temperatures is the interruption of forced cooling by a trip of all primary pumps, referred to here as a Loss of Forced Cooling (LOFC) transient. Two possible flow paths appear for the primary coolant: the natural circulation loop provided by the PHX system, and the loop created by the IHX modules.

Comparing the potential total pressure losses through the PHX and the IHX loops at the same flow rate provides an estimate of their relative flow resistances. Considering the IHX as an assembly of 1 mm diameter semicircular channels with a flow length of 1m and a total area of 7 m^2, with a flow rate of 100 kg/s, we have the following pressure losses inside the IHX modules:

$$\mathrm{Re} = 1.1, \quad f = \frac{64}{\mathrm{Re}} = 41, \quad \Delta p = 3400\ Pa$$

In the PHX loop with the same flow rate, including the laminar losses in the PHX module and the form losses through the loop (in particular in the fluidic diode):

$$\mathrm{Re} = 230, \quad f = \frac{64}{\mathrm{Re}} = 0.28, \quad \Delta p_{phx} = 23\ Pa$$
$$K = 4 \quad \Delta p_{form} = 630\ Pa$$

This means that the flow resistance of the IHX loop is at least 5 times larger than the total flow resistance through the PHX natural circulation loop. Here it is also assumed that heat removal from the IHX's stops. Thus the combination of relatively high flow resistance in the IHX loops, and low natural circulation driving head in the IHX loops due to the absence of heat removal, results in a negligible flow rate through the IHX's.

Heat removal would then occur by natural circulation and forced convection through the PHX modules to the buffer salt. The buffers salt in turn is cooled by the DHX modules. Two different scenarios can be considered, depending on whether reactor scram does, or does not, occur:

– LOFC. Scram occurs and radioactive decay alone heats the core. This is the more probable of the two transients, as failure to scram has a very low probability given the reliability of control rod and reserve shutdown mechanisms. This transient would also be a normal transient for the core, as it may be used as a normal shut-down method for the reactor. It will be referred to as the LOFC transient

– ATWS. For liquid cooled reactors, the anticipated transient without scram (ATWS) has the potential to be a more severe transient than it is in modular helium reactors, as negativity reactivity feedback may not be sufficient to minimize the total power output before substantial increases in coolant temperatures occur. Furthermore, recent studies underline the possibility of a small positive void reactivity feedback with Flibe cooled fuel, balanced by a larger negative fuel Doppler feedback (see [7] and [10]). On the other hand, more recent and specific neutronics studies of the PB-AHTR fuel show that negative coolant reactivity are attainable, with the right fuel loading per pebble (see [20]). This transient will be referred to as the ATWS.

3) Objectives and organization of this work

The primary objective of this work is to provide a preliminary assessment of the safe behavior of the PB-AHTR during both LOFC and ATWS transients. Using the general framework of the CSAU method, this study can be divided into four successive parts:

– Evaluation of relevant pressure losses and heat transfer correlations, and assessment of the need for SET to obtain more experimental data. The original association of liquid salt coolant and pebble fuel calls for an investigation of thermal hydraulics correlations for pebble bed. The use of a high Pr coolant implies the study of convection regimes where buoyancy and inertia forces have similar magnitudes: this is significant for the study of heat transfer in the PHX system and the pebble bed core.

– Phenomena identification and ranking tables (PIRT) for steady state and for LOFC/ATWS transients. This will lead to the identification of SET experiment requirements and the design of scaled IET experiments to correctly reproduce the different coupled phenomena of the reactor

– Calculation of reactivity feedbacks of the pebble core with change of coolant and fuel temperatures. This computation provides the basis for further study of the ATWS scenario

– Description of a RELAP5 model for the pebble bed AHTR. Steady-state operation and LOFC and ATWS transients are studied with this model and some modifications of the PB-AHTR design are also studied parametrically.

Bibliography

[1] C.W. Forsberg, P. Pickard, and P.F. Peterson, *Molten-Salt-Cooled Advanced High-Temperature Reactor for Production of Hydrogen and Electricity*, Nuclear Technology **144**, 289-302 (2003).

[2] Generation IV International Forum, *http://www.gen-4.org/Technology/evolution.htm*.

[3] Generation IV International Forum, *http://www.gen-4.org/Technology/systems/msr.htm*.

[4] K. Minato, T. Ogawa, K. Fukuda, H. Sekino, H. Miyanishi, S. Kado, and I., Takahashi, *Release behavior of metallic fission products from HTGR fuel particles at 1600 to 1900 degree C*, Journal of Nuclear Materials **202**, 47-53 (1993).

[5] H Nickel, H Nabielek, G Pott, AW Mehner, *Long time experience with the development of HTR fuel elements in Germany*, Nuclear engineering and design **217**, 141-151 (2002).

[6] Cliff B. Davis and Grant L. Hawkes, *Thermal-Hydraulic Analyses of the LS-VHTR*, in International Congress on Advances in Nuclear Power Plants, Reno, June 4-8, 2006

[7] S.J. de Zwaan, *The Liquid Salt Pebble Bed Reactor, A new high-temperature nuclear reactor*, Delft University of Technology (2006), PNR-131-2005-008.

[8] Per F. Peterson and Haihua Zhao, *A Flexible Baseline Design for the Advanced High Temperature Reactor Using Metallic Internals (AHTR-MI)*, in International Congress on Advances in Nuclear Power Plants, Reno, June 4-8 2006

[9] C. Forsberg, *Alternative Passive Decay Heat Systems for the Advanced High Temperature Reactor*, in International Congress on Advances in Nuclear Power Plants, Reno, 4-8 Jun 2006

[10] D.F Williams et al., *Assessment of Candidate Molten Salt Coolants for the Advanced High-Temperature Reactor (AHTR)*, Oak Ridge National Laboratory (2006), ORNL/TM-2006/12.

[11] Franz Paul Hauk, *Design and set-up of a high temperature flow loop for the investigation of heat transfer and pressure loss in a mixed convection regime flow of higher Prandtl number molten salt simulants*, Diplomarbeit, UC Berkeley & Technische Universität München (2006)

[12] D.F Williams, *Assessment of Candidate Molten Salt Coolants for the NGNP/NHI Heat-Transfer Loop*, Oak Ridge National Laboratory (2006), ORNL/TM-2006/69.

[13] D. T. Ingersoll, et al., *Status of Physics and Safety Analyses for the Liquid-Salt-Cooled Very High-Temperature Reactor (LS-VHTR)*, Oak Ridge National Laboratory (2005), ORNL/TM-2005/218.

[14] William Casino, *Investigation of an Alternative Fuel Form for the Liquid Salt Cooled Very High Temperature Reactor (LS-VHTR)*, in International Congress on Advances in Nuclear Power Plants, Reno, 4-8 Jun 2006

[15] Pebble Bed Modular Reactor Ltd., *http://www.pbmr.com/index.asp?Content=103&MState=DT&Cat=-1&Image=16*.

[16] Salomon Levy, *Two phase flow in complex systems*, Wiley-IEEE (1999)

[17] R.B. Vilim et al, *Initial VHTR Accident Scenario Classification: Models and Data*, Argonne National Laboratory (2004)

[18] US Nuclear Regulatory Commission, 2004, SECY-04-0001.

[19] H. Nabielek, W. Schenk, W. Heit, A. W. Mehner, and D. T. Goodin, *The Performance of High-Temperature Reactor Fuel Particles at Extreme Temperatures*, Nuclear technology **84**, 62-81 (1989).

[20] M. Fratoni, E. Greenspan and P.F. Peterson, *Neutronic and Depletion Analysis of the PB-AHTR,* in Global '07, Advanced Nuclear Fuel Cycles and Systems, Boise, Idaho (2007).

2. Thermal Hydraulics Correlations for the PB-AHTR

During LOFC and ATWS transients, a variety of heat transfer and fluid mechanics phenomena occur in the PB-AHTR that are important to the transient response and determine the peak core outlet temperature. This chapter reviews several of the heat transfer and pressure loss correlations required to model the PB-AHTR transient response.

A. Laminar mixed convection in vertical channels

Assessing the flow conditions of the primary salt in the PHX modules is important to determine the correct heat removal rate from the primary coolant during loss of forced cooling transients. Given mass flows of around 100 kg/s on the primary side, the typical Re expected in the PHX pipes is Re_d = 230. This normally corresponds to laminar flow, where the uniform heat flux Nusselt number is given by:

$$Nu = 4.364$$

However, we can also estimate the Grashof number based on the tube diameter d:

$$Gr_d = \frac{\beta g \Delta T d^3}{\nu^2} \tag{2.1}$$

where ΔT is a typical temperature difference (for instance $T_{out} - T_{in}$). Evaluating this parameter in the PHX system yields the fairly large value Gr_d = 410,000.
Another interesting Grashof number is given by the tube diameter and the axial temperature gradient in the tube:

$$Gr_{dL} = \frac{\beta g (\Delta T / L) d^4}{\nu^2} = Gr_d \frac{d}{L} \tag{2.2}$$

Figures 2-1 and 2-2 give an overview of the change in flow and temperature distributions with changing temperature difference for a downward flowing cooled flow, which corresponds to the situation in the PHX. These figures are based on an analytical solution derived by Hallman [14].

At high Gr_{dL} value, colder conditions and stronger gravity forces will tend to accelerate the fluid near the wall: because of conservation of mass, fluid in the center of the tube will in turn tend to decelerate. At a very high value of $Ra_{dL} = Gr_{dL}Pr$, the flow will actually reverse near the centerline.

We see that higher Ra_{dL} will flatten the temperature distribution at the center of the tube, and sharpen the temperature gradients near the wall. The Nusselt number $Nu = d / \delta_{th}$ will then tend to increase. This means that laminar mixed convection heat transfer in these conditions ("aiding buoyancy") should be enhanced compared to simple convection. The same conclusion holds for the symmetric conditions (upward flowing

heated flow). On the other hand, upward cooled or downward heated flows ("opposing buoyancy") should have decreased heat transfer.

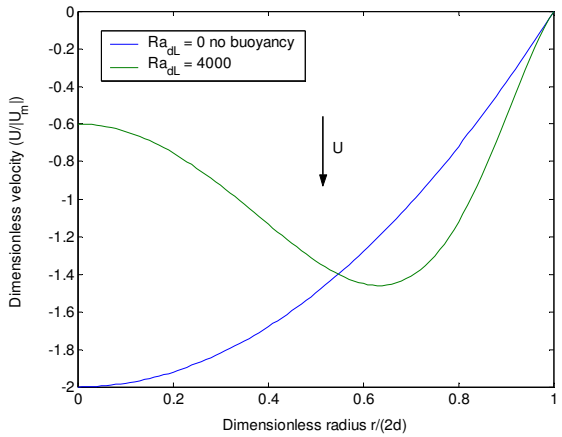

Figure 2-1: Flow distribution for a downward flowing cooled fluid (adapted from Hallman [14]). In the baseline design, we have $Ra_{dL} = PrGr_{dL} = 38{,}000$

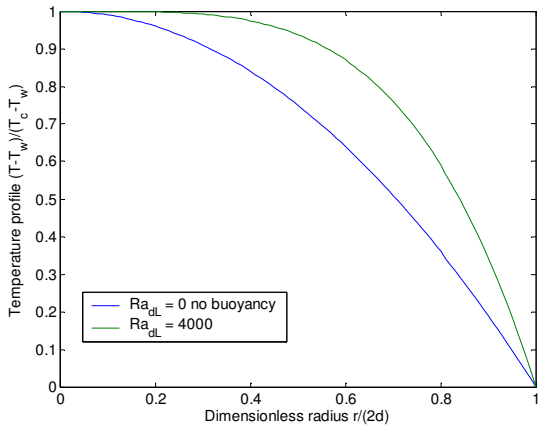

Figure 2-2: Temperature distribution for a downward flowing cooled fluid (adapted from Hallman [14]).

This section will describe the possible criteria to assess the influence of buoyancy effects in forced convection, give available heat transfer correlation for laminar mixed convection and discuss the applicability of RELAP5-3D code in these conditions.

1) Criteria to assess importance of mixed convection

A simple criterion can be based on the idea that the ratio between buoyancy and inertial forces can quantify the influence of buoyancy in convective heat transfer. According to Holman heat transfer handbook [15]:

$$\frac{F_{buo}}{F_{ine}} = \frac{Gr_d}{\mathrm{Re}^2} \tag{2.3}$$

The buoyancy effects begin to dominate if $Gr_d/Re^2 > 10$. For the PHX, we have $Gr_d/Re^2 \sim 8$. This means buoyancy should have a strong effect in these conditions.

Another graphical approach is given by Metais and Eckert [16] (Fig. 2-3).

The PHX module functions around $Ra_{dL} \sim 38{,}000$ and $Re \sim 230$. This means that the conditions are on the boundary between the mixed-laminar, the transition between laminar and turbulent flows and the laminar free convection flow regions. Hallman [17] observes such a transition between mixed laminar and unsteady flow with the following boundary between the two regimes:

$$\text{Laminar regime when } Gr_d \,\mathrm{Pr} < 9470\left(\frac{\mathrm{Re}\,\mathrm{Pr}}{2x/d}\right)^{1.83}$$

where x is the axial position into the tube. For the PHX system, $Gr_dPr = 5\times10^6$, and $9470\left(\frac{\mathrm{Re\,Pr}}{2L/d}\right)^{1.83} = 1\times10^6$, which means that the transition to turbulence occurs at an intermediate location along the PHX length.

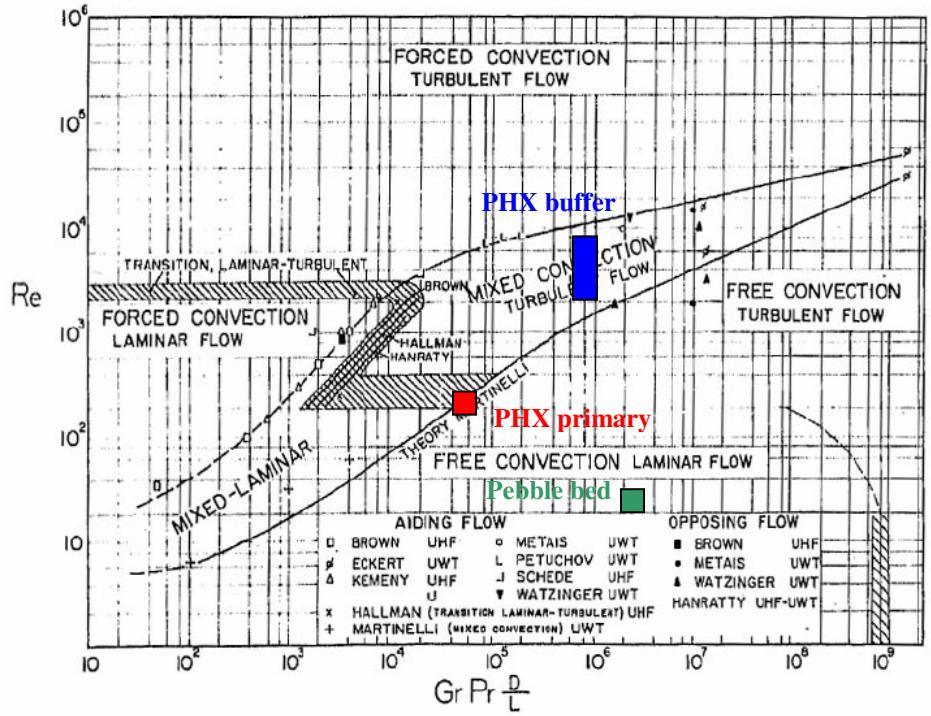

Figure 2-3: Regimes of forced, mixed and free convection in vertical tube. Note that the grouping GrPrD/L in the figure is equivalent to $Ra_{dL} = Gr_{dL}Pr$ used in this report. The red square represents the conditions in the primary side of the PHX (Re~230, Ra_{dL}~38,000), the blue rectangle in the buffer salt side (Re~2600-7000, $Ra_{dL}=1.4\times10^6$), and the green square shows the condition existing in the pebble bed (Re~30, $Ra_{dL}=2.5\times10^6$)

However, according to a latter stability study by Scheele and Hanratty [18], the onset of this unsteady flow does not change the Nusselt number significantly, as predicted by laminar mixed forced convection correlations. For conservatism, this analysis uses the laminar correlations in the rest of this study, even though actual heat transfer coefficients are likely to be higher.

Further investigation needs to be done to assess a more precise the heat transfer correlation on the primary side of the PHX: this recommendation is reinforced by the fact that no data is presented for high Pr fluid such as flibe at ~700ºC. These experiments will be performed in the future using the simulant oil heat transfer loop set up in the UCBNE Thermal Hydraulics Laboratory.

2) Laminar mixed correlations

There have been extensive numerical and experimental studies of laminar mixed convection for buoyancy aided laminar flow in circular tubes during the 50's and the 60's. Reviews on these are available in two heat transfer handbooks [19,20]. Interestingly enough, much of the work on laminar mixed convection in vertical channels was done for the design of a liquid metal fuel reactor (LMFR), where this type of flow regime can appear in the core channel during LOFC [14].

A recommended correlation for uniform wall temperature and developing flow is given by Jackson et al. in [27]:

$$Nu_{Jack} = 1.128\left\{Gz(x) + \left[3.02\left(Ra_{dL}\,\mathrm{Pr}\right)\right]^{0.4}\right\}^{1/2}$$
$$\text{with}\quad Gz(x) = \frac{\mathrm{Re}_d\,\mathrm{Pr}\,d}{x} \tag{2.4}$$

Hallman [14], Morton [21] and Tao [22] gives an analytical solution for the uniform heat flux problem, with a fully developed flow profile, in terms of functions of the Ra_{dL} number only. This complicated correlation involves modified Bessel functions, but has the following limits:

$$\begin{aligned} Ra &\to 0 \quad Nu_{Hall} = 4.36 \\ Ra &\to \infty \quad Nu_{Hall} = 0.644 Ra_{dL}^{0.28} \end{aligned} \tag{2.5}$$

This last correlation is supported by data provided by Hallman [17] and plotted in Fig. 2-4. It includes the point Ra_{dL}=38,000 corresponding to the conditions prevalent in the baseline PHX modules. However, the data does not provide the precise Re corresponding to each data point, which means that transition to turbulence may appear in the primary side of the PHX module, as pointed out in the last paragraph. Incidentally, this correlation follows a power law of around ¼, which is the same as laminar natural convection on a vertical plate.

Correlations for uniform heat flux should be applied to the downward cooled flow that occurs in the PHX modules, as these heat exchangers have a counter-flow design which maintains a fairly constant temperature difference between the primary and the buffer salt. Nonetheless, the uniform wall temperature correlations, Eq. (2.4), actually give similar results, given that the entry effects are negligible (because $Gz(L) << 1$);

$$Nu_{Jack} = 1.41\,\mathrm{Pr}^{0.2}\,Ra_{dL}^{0.2}$$

Evaluating the Nusselt for uniformly heated flow using Eq.(2.5) for high Rayleigh, we obtain Nu_{Hall} = 13. This number is 3 times higher than the Nusselt for pure laminar convection.

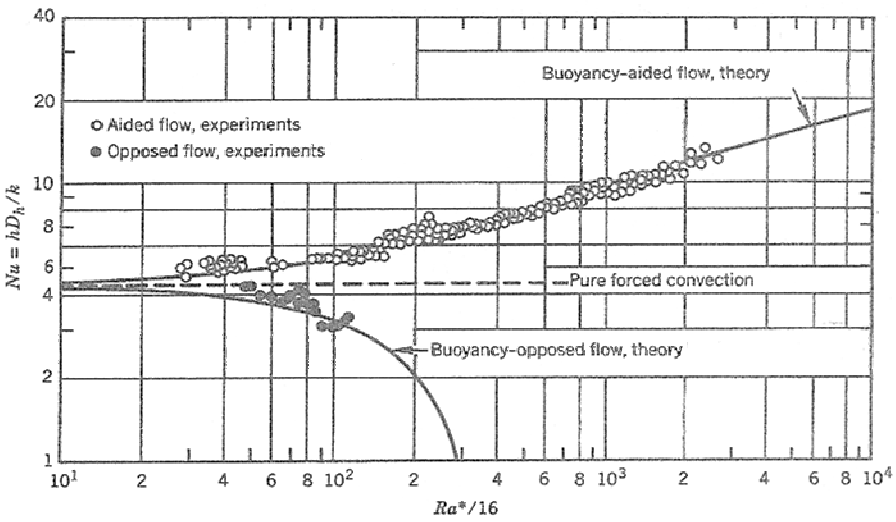

Figure 2-4: Comparison between theory and experiments for laminar mixed convection in vertical tubes. Ra^* corresponds to Ra_{dL}. For the primary side of the PHX, $Ra^*/16 = 2400$. The experimental points are from [17]**, the correlation from** [14]. **The limits for low/high Ra if given by Eq.(2.5)**

3) RELAP5-3D implementation

According to Volume IV of the RELAP5-3D manual [23], RELAP5-3D calculates the Nusselt number for heat transfer in vertical tubes using the equation:

$$Nu = \max(Nu_{f-lam}, Nu_{f-turb}, Nu_{free}) \tag{2.6}$$

– Laminar forced convection

$$Nu_{f-lam} = 4.36$$

– Dittus-Boelter correlation for turbulent forced convection

$$Nu_{f-turb} = 0.023\,\mathrm{Re}^{0.8}\,\mathrm{Pr}^{0.3}$$

For the PHX LOFC transient, $Nu_{f\text{-}turb} = 3.7$

– Churchill-Chu correlation for free convection on a vertical plate

$$Nu_{free} = \left(0.825 + 0.387(Gr_d\,\mathrm{Pr})^{1/6} \left(1 + \left(\frac{0.492}{\mathrm{Pr}} \right)^{9/16} \right)^{-8/27} \right)^2$$

taking the Gr number based on the tube diameter: this correlation is valid for the full laminar and turbulent Rayleigh number range. This yields $Nu_{free} = 31$

The manual gives several caveats concerning this correlation: more correlations need to be added for different channel geometries and mixed convection effects are still not implemented in the code.

In these conditions, there should be laminar mixed convection inside the PHX tubes according to the previous analysis. The RELAP5-3D correlation (2.6) actually reproduces this behavior by using the Churchill-Chu natural convection correlation for this boundary condition, but the RELAP5-3D Nusselt number ends up being two times higher than the one predicted the laminar mixed convection correlations (2.5) (Nu = 31 instead of 13).

In the RELAP5-3D simulations, parametric studies changing the PHX design will provide an assessment of the consequences of such a bias in the calculation of the PHX heat transfer coefficient.

B. Turbulent mixed convection in vertical channels

The buffer salt side of the PHX has significantly different flow conditions compared to the primary side: the mass flow varies typically between 300 and 800 kg/s during LOFC and ATWS transients, and the viscosity of the NaF-$NaBF_4$ sodium fluoroborate salt is significantly lower than for flibe (by a factor 5). This means the Re number will be a much higher on this side, a typical range being Re = 2600 to 7000.

Adopting similar notation than in the previous section (Eqs.(2.1) and (2.2)), we can calculate typical values of the Grashof and Rayleigh numbers:

$$Gr_d = 2.7\times10^7$$
$$Gr_{dL} = 3.2\times10^5$$
$$Ra_{dL} = 1.4\times10^6$$

where d = 3.74 cm is the wetted diameter of the 2.5 cm tubes which have a square array with a pitch of 3.5 cm.

This section concentrates on providing the most accurate description of the heat transfer in this turbulent mixed convection regime on the buffer salt side of the PHX. It is mostly based on a previous review of this subject by Hauk [24].

For upward heated flow (i.e. aiding gravity), the effect of buoyancy can reduce the overall heat transfer coefficient. Hotter fluid near the wall will be accelerated, whereas fluid near the centerline will decelerate: this will decrease the difference between the velocity of surface of the boundary layer and the average velocity and decrease the shear stress between the perimeter and the bulk of the flow (Fig. 2-5) Thus, the flow will be laminarized, which decreases the heat transfer coefficient.

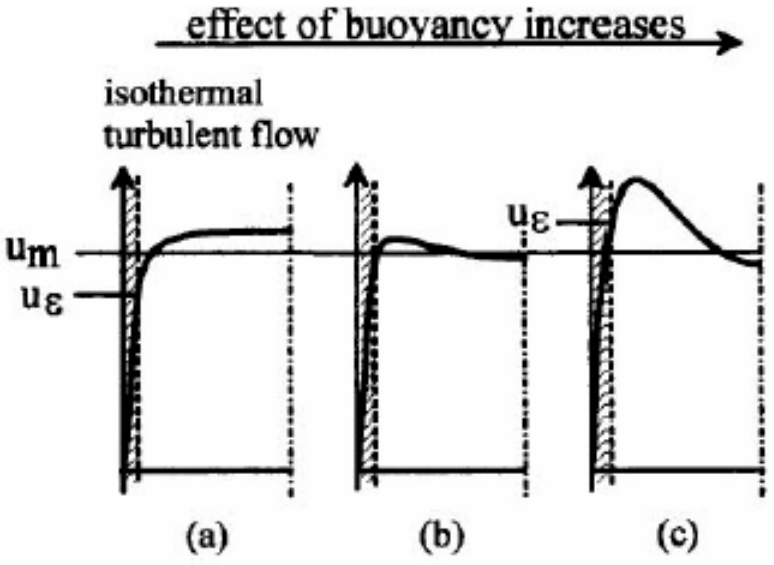

Figure 2-5: Effect of buoyancy forces on a turbulent velocity profile (a) No buoyency (b) Medium buoyancy: small shear stresses, laminarization of the flow (c) Strong buoyancy: turbulence reappears (from [25])

1) Criteria to assess the importance of mixed convection in turbulent flows

The previous criterion, Eq.(2.3), based on Gr_d/Re^2 = 3.9 to 0.55, shows that buoyancy effects should also be important in the buffer side of the PHX.

A better criterion adapted to turbulent flows in the PHX primary side can be derived by comparing the thickness of the boundary layer for free convection and turbulent forced convection, as proposed by Bejan [26]:

$$\delta_n \propto y Ra_d^{-1/5}$$
$$\delta_{fo} \propto y \,\mathrm{Re}_d^{-1/2}\,\mathrm{Pr}^{-1/3}$$

When this natural convection boundary layer estimate is thinner than the forced convection boundary layer, buoyancy outweighs inertia, and vice et versa. Forced convection dominates when:

$$\frac{Gr_d^{1/5}}{\mathrm{Re}_d^{1/2}\,\mathrm{Pr}^{2/15}} = \frac{Ra_d^{1/5}}{\mathrm{Re}_d^{1/2}\,\mathrm{Pr}^{1/3}} < 0.1$$

For the buffer salt side, the resulting range of values is $\frac{Gr_d^{1/5}}{\mathrm{Re}_d^{1/2}\,\mathrm{Pr}^{2/15}} = 0.5 \text{ to } 0.3$

Jackson et al. proposed a similar criterion, and tested it against a broad range of experimental conditions. According to [27], the buoyancy effects correspond to less than 5% of the forced convections values when:

$$\frac{Gr_d}{\mathrm{Re}_d^{2.7}\,\mathrm{Pr}^{0.5}} < 10^{-5}$$

On the buffer side of the PHX: $\frac{Gr_d}{\mathrm{Re}_d^{2.7}\,\mathrm{Pr}^{0.5}} = 8\times10^{-3} \text{ to } 5\times10^{-4}$

All these numerical criteria point to the importance of buoyancy effects in determining the correct flow conditions and heat transfer coefficients in the PHX. This is confirmed by the examination of Fig. 2-3, where the blue rectangle represents the zone accessible on the buffer salt side of the PHX during the LOFC / ATWS transients: this region is clearly in the middle of the mixed convection / turbulent flow regime.

2) Available correlations for turbulent mixed convection

According to Hauk [24], the most recent and precise heat transfer correlation for this flow regime has been presented by Celata et al. [28]. It uses the following non dimensional parameter *Bo* to assess the strength of buoyancy due to heat input from the wall (not to be confused with the Bond number):

$$Bo = 8\times10^4 \frac{Gr_h}{\mathrm{Re}_d^{3.425}\,\mathrm{Pr}^{0.8}} \qquad (2.7)$$

where

$$Gr_h = \frac{\beta g d^4 q''}{k\nu^2}$$

is a modified Grashof number based on the wall heat flux. For the purpose of estimating the buoyancy parameter *Bo*, we can estimate the difference between the bulk and the wall temperature as being approximately half of the total temperature difference between the primary and the buffer (i.e. 100/2 = 50ºC). With the estimated Nu ~ 30, this gives q'' ~ 20,000 W/m^2 . With these assumptions, the buoyancy parameter should vary in the interval:

$$Bo = 19.2 \text{ to } 0.67 \quad \text{(low - high Reynolds)}$$

The correlation can be best understood using Fig. 2-6. For low Bo, forced convection dominates. For upward flow in a heated channel, the greatest reduction in heat transfer occurs at Bo of order unity. At larger Bo, the buoyancy forces begin to dominate and at sufficiently high Bo the Nusselt number can become greater than for forced convection. For opposing flows (down flow in a heated channel), the Nusselt number in mixed convection increases monotonically with Bo.

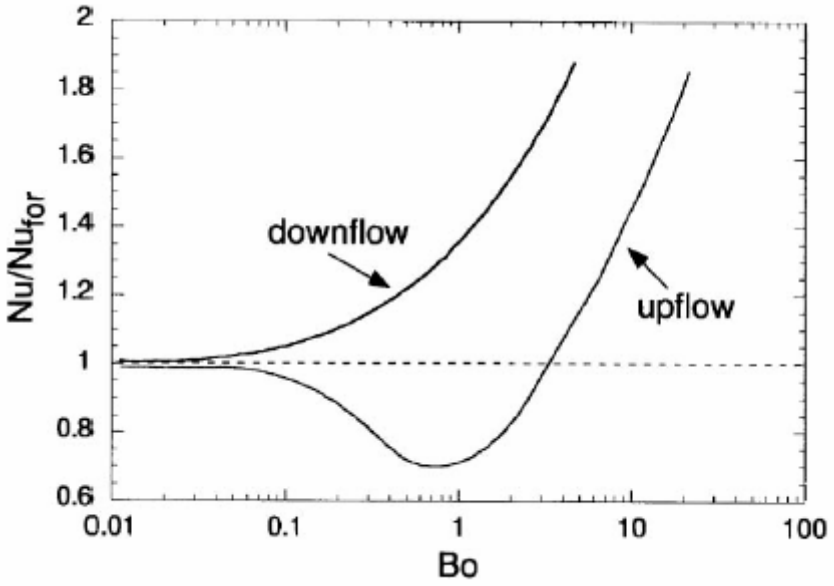

Figure 2-6: Scheme representing of the ratio of mixed convection Nusselt / pure forced convection Nusselt versus buoyancy *Bo*, for up/down turbulent flow in a heated channel. (from [27])

Celata gives the following correlation for opposing buoyancy flow:

$$Nu_{opp} = \left(Nu_{for}^3 + Nu_{nat}^3 \right)^{1/3}$$
$$Nu_{for} = 0.023 \,\mathrm{Re}_d^{0.8} \,\mathrm{Pr}^{0.4} \left(\frac{\mu_{bulk}}{\mu_{wall}} \right)^{0.11} \qquad (2.8)$$

$$Nu_{nat} = 0.15\left(Gr_d \,\mathrm{Pr}\right)^{1/3}\left(1+\left(0.487/\mathrm{Pr}\right)^{9/16}\right)^{-16/27}$$

which is a combination of the Dittus-Boelter forced convection equation and an adaptation of the free convection Churchill-Chu correlation in the case of heat transfer in tubes (see Eq.(2.6) for the RELAP5-3D implementation for vertical flat plates).

An impediment factor is then calculated versus the buoyancy parameter Bo:

$$\psi = 1 - a\exp\left\{-0.8\left(\log\left(\frac{Bo}{b}\right)\right)^2\right\} \qquad a = 0.36 + 0.0065\frac{L}{d} \quad b = 869\left(\frac{L}{d}\right)^{-2.16} \tag{2.9}$$

and the assisting buoyancy flow correlation is $Nu_{as} = \psi Nu_{opp}$. Figure 2-7 gives the shape of the function $\psi(Bo)$ for the geometry of the PHX (L/d = 128).

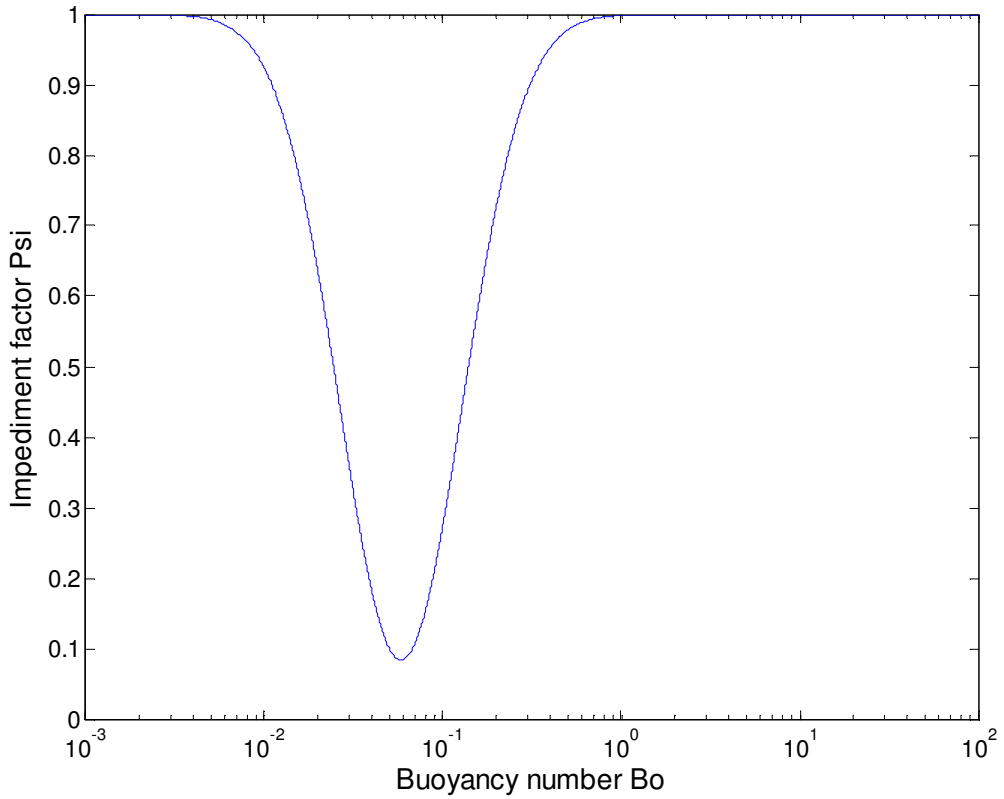

Figure 2-7: Celata et al. $\psi(Bo)$ factor versus buoyancy (L/d = 128)

Figure 2-8 presents a comparison of the Celata correlation versus experimental data. The range of L/d studied is 10-40, while for the PHX L/d is 128. Most of the data lie within 20% of the proposed correlation. Hence, this relatively low precision shows the need for data in the Prandtl range of interest for liquid salts, and for vertical tubes with higher aspect ratio, either to validate this correlation or establish a new correlation.

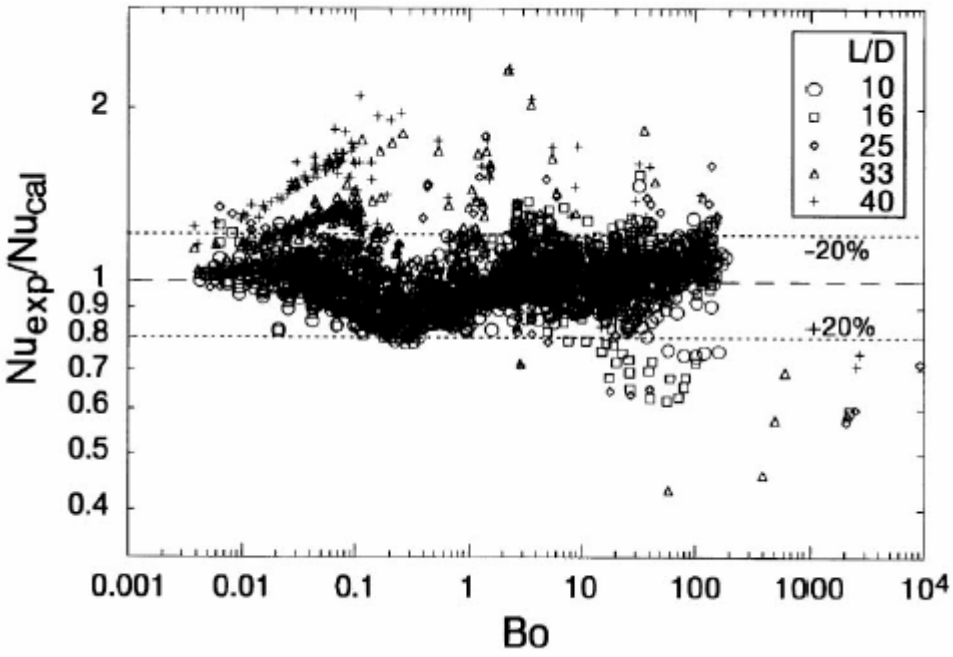

Figure 2-8: Comparison of experimental data and Celata correlation, at various L/d ratios

With the flow conditions in the PHX, we obtain the following impediment factors:

$$\psi = 1 \text{ to } 0.99 \quad \text{(low - high Reynolds)}$$

This means that according to the correlations, Eqs. (2.8)-(2.9), the PHX buffer flow is hardly impeded compared to the opposing buoyancy flow situation. This yields estimates of the Nusselt number:

$$Nu_{as} = Nu_{opp} = \left((23 \text{ to } 50)^3 + 51^3\right)^{1/3} = 53 \text{ to } 63 \qquad \text{(low Re - high Re)}$$

Because the buoyancy effects are strong in the PHX, the final Nu estimates are not so much different from the Nu value estimated assuming only natural convection.

RELAP5-3D evaluates the maximum of the forced convection Nusselt number (using the Boelter correlation as does Celata's correlation) and the free convection Nusselt (using a very similar version of Churchill-Chu correlation). In this condition, the difference between RELAP5-3D method, Eq.(2.6) and Celata's equations (2.8)-(2.9) is not very large, as natural convection tends to dominate here (Nu_{as} = 53 to 63 for Celata, Nu_{nat} = 51 for RELAP5-3D).

C. Pebble bed pressure loss and heat transfer correlations

Thermal hydraulics correlations for a randomly packed pebble bed are obtained by considering the bed as a porous media with a given porosity ε. The usually recommended average value for gas-cooled reactors has been measured by experiments done with randomly packed static beds in air [1]:

$$\varepsilon = 0.35 - 0.43$$

Pebble landing dynamics onto the pebble bed may be different in the liquid-salt cooled PB-AHTR, resulting in somewhat different packing density. Experiments in the PREX facility, described in the next chapter, will measure this packing density, but for analysis purposes here, this report uses the value $\varepsilon = 0.4$.

Significant variations of this porosity occurs a few pebbles away from the wall containing the bed, and correlated structures can occur as far as 6.5 pebbles away from the wall [2]. A homogeneous porosity model is accurate as long as the dimensions of the bed are significantly larger than the diameter of the pebble. A criterion for this is then:

$$\frac{D}{d_p} > 13$$

where D is the diameter if the bed, and d_p the diameter of a single pebble. The value of this ratio is 112 for the current PB-AHTR, which confirms the uniform porosity porous media approach. The PREX facility has $D/d_p = 16$.

1) Pressure losses: the Ergun equation

Most of pressure loss correlations for porous media are extensions from Darcy's law, for which pressure gradients Δp are directly proportional to the fluid velocity v, and thus the friction factor $f = \frac{\Delta p\, d_p}{\rho v^2 L}$ varies as $\frac{1}{\mathrm{Re}_d}$, where d_p is the pebbles diameter and L the total length of the bed.

This correlation is only valid for laminar flow at very low Reynolds. Empirical extensions of Darcy's law were first proposed by Ergun [3]. According to Ergun's law, the friction factor is given by:

$$f = \frac{1-\varepsilon}{\varepsilon^3}\left(a\frac{1-\varepsilon}{\mathrm{Re}_d} + b \right) \quad \text{with} \quad \mathrm{Re}_d = \frac{\dot{m} d_p}{\mu A_c} \tag{2.10}$$

where Re_d is the Reynolds number based on the pebble diameter, the total area A_c of the core, the fluid dynamic viscosity μ and the mass flow $\dot{m}$. The term proportional to Re^{-1} corresponds to laminar losses, whereas the constant term is associated to turbulent/form losses.

A broad number of references give possible values for the two parameters a and b, depending on the precise geometry of the porous media and the roughness of the solid/liquid boundary. According to a major review ([4], 1979), the recommended values for a smooth particles bed are $a = 180, b = 1.8$; whereas a more recent reference ([5], 1996) used by the previous PB-AHTR transient study [6] uses the somewhat lower values $a = 170, b = 1.75$.

Another possible correlation is given by Kugeler and Schulten [7] and is recommended by the German nuclear regulatory commission for studies on gas cooled pebble bed reactors (KTA correlation [8]):

$$f = \frac{1-\varepsilon}{\varepsilon^3}\left(\frac{160}{\mathrm{Re}_d/(1-\varepsilon)} + \frac{3}{\left(\mathrm{Re}_d/(1-\varepsilon)\right)^{0.1}}\right) \tag{2.11}$$

A typical values of the Reynolds number for steady state forced circulation operation in the PB-AHTR is $\mathrm{Re_d} = 2700$ ($\dot{m} \sim 10{,}000$ kg/s), and it drops to around $\mathrm{Re_d} = 30$ under loss of forced cooling transients ($\dot{m} \sim 100$ kg/s). This corresponds to the f values for the PB-AHTR core presented Table 2-1.

Correlations	Ergun (a = 180, b = 1.8)	Ergun (a = 170, b = 1.75)	KTA
f at $\mathrm{Re_d} = 2700$	17.3	16.8	12.5
f at $\mathrm{Re_d} = 30$	50.6	48.3	49.0

Table 2-1: Comparison of various pebble bed pressure losses correlations

This previous table shows that the two first correlations based on Eq. (2.10) provide similar results, whereas the correlation, Eq. (2.11), exhibits significant differences at forced circulation flow rates. However, as pointed out by [4], there may be up to 15% discrepancies between these correlations and experimental data for spherical pebbles.

This report will use the Ergun correlation, Eq. (2.10), with a = 180 and b = 1.8, which would overestimate force circulation pressure losses. Under forced circulation, pressure losses occur dominantly in the intermediate heat exchangers in any case.

2) Available heat transfer correlations

A simple heat transfer correlation for forced convection through pebble beds was proposed by Wakao and described by Kaviany's heat transfer handbook [9]

$$Nu_{wak} = \frac{h\,d}{k} = 2 + 1.1\mathrm{Re}_d^{0.6}\,\mathrm{Pr}^{1/3} \tag{2.12}$$

The constant 2 corresponds to the heat transfer coefficient found when solving the heat transfer equations for a single pebble immersed in a stagnant liquid with a uniform

temperature far from the pebble. The other term is very similar to the Dittus-Boelter equation for smooth tubes, except for the 0.6 exponent on Re_d, instead of 0.8.

According to the review paper by Alazmi published in 2000 [10], this correlation is applicable for 10 < Re < 10,000 and for a very narrow range of Pr, as experiments to validate the correlation have only been carried on with air, H_2, CO_2 gas and liquid water.

A slightly different approach can be found in papers by Gnielinski [11], who gives the following equation:

$$\begin{aligned} Nu_{gn} &= \left(1+1.5(1-\varepsilon)\right)\left[2+\sqrt{Nu_{lam}^2+Nu_{turb}^2}\right] \\ Nu_{lam} &= 0.664\,\mathrm{Re}_d^{1/2}\,\mathrm{Pr}^{1/3} \\ Nu_{turb} &= \frac{0.037\,\mathrm{Re}_d^{0.8}\,\mathrm{Pr}}{1+2.443\,\mathrm{Re}_d^{-0.1}(\mathrm{Pr}^{2/3}-1)} \end{aligned} \qquad (2.13)$$

If we neglect the term Nu_{turb} the following dependency is found, which looks quite similar to Nu_{kav}:

$$Nu_{gn} = 3.8 + 1.5\,\mathrm{Re}_d^{1/2}\,\mathrm{Pr}^{1/3}$$

Gnielinski provides supporting data for his correlations from various experiments with various gases or air (i.e. with Pr = 0.7-0.8). Furthermore, a fit of experimental data for mass transfer in packed sphere bed was considered using the equivalency between Nusselt and Sherwood numbers, and between Prandtl and Schmidt number:

$$Nu = \frac{h\,d}{k} \quad Sh = \frac{K\,d}{D}$$

$$Pr = \frac{c_p \mu}{k} \quad Sc = \frac{\frac{1}{\rho}\mu}{D}$$

where h (in W/m^2K) and K (in $ms^{-1}=kgs^{-1}/(m^2kg/m^3)$) are the thermal/mass transfer coefficients, k (in W/mK) is the thermal conductivity and D (in $m^2s^{-1} = kgs^{-1}/(mkg/m^3)$) the mass diffusivity. Figure 2-9 gives an overview of the comparison between the Gnielinski data and correlation.

The lines fit the data at various Pr/Sc within a relative difference smaller than 50%. There is a broad range of data points for small Pr/Sc = 2-3 (Pr = 0.7 experiments are not shown here) with Re between 30 and 10000. There are also a lot of points for very high Pr/Sc (800-10000) with Re between 1 and 10000. However, the data for intermediate range Pr/Sc is only represented by Pr = 7, with Re ranging from 300 to 3000. No data point is shown for the region Pr ~ 15 / Re ~ 30, which the typical operating conditions of the AHTR bed during LOFC and ATWS transients.

Finally, there is also a correlation recommended by the German regulatory commission, for gas cooled reactor (Pr = 0.7), with Re ranging from 100 to 10^5 [12]:

$$Nu_{KTA} = 1.27 \frac{\mathrm{Pr}^{1/3}}{\varepsilon^{1.18}} \mathrm{Re}^{0.36} + 0.033 \frac{\mathrm{Pr}^{1/2}}{\varepsilon^{1.07}} \mathrm{Re}^{0.86} \qquad (2.14)$$

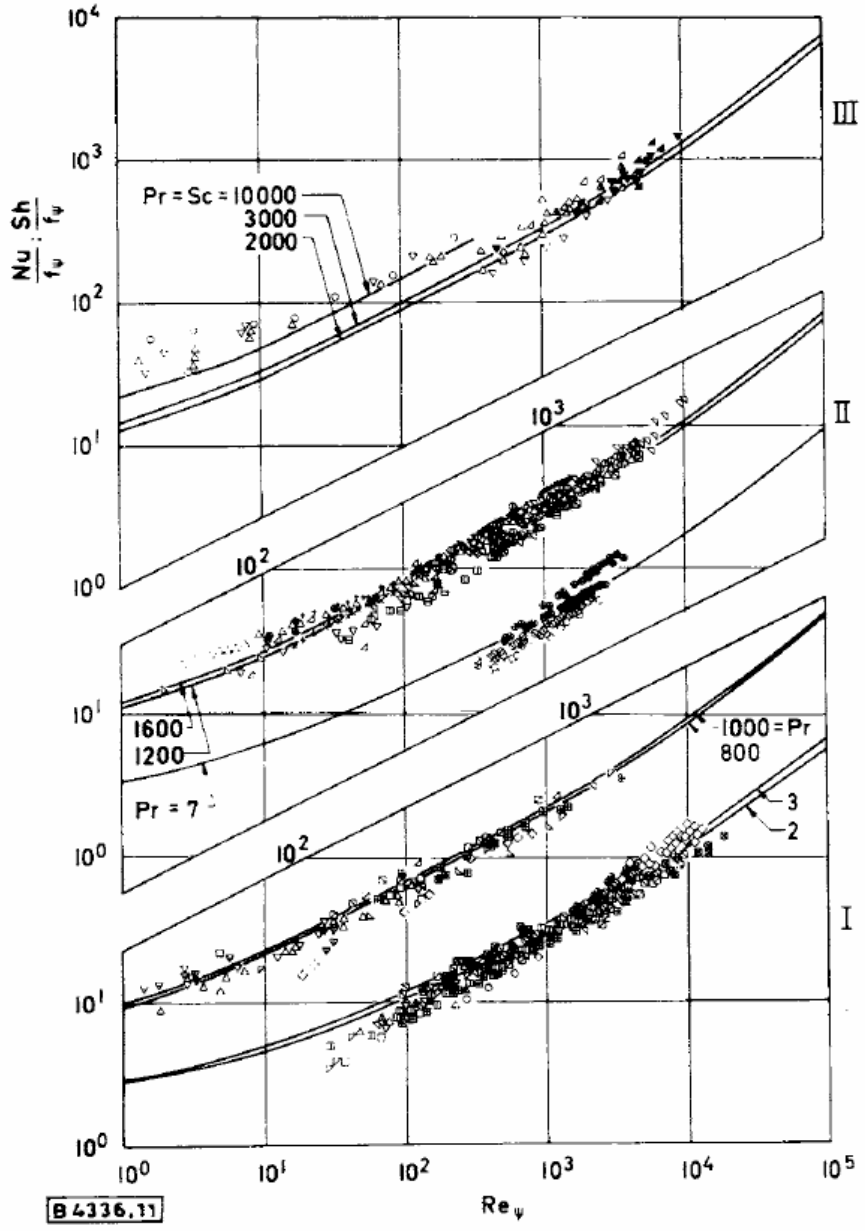

Figure 2-9: Comparison between various heat/mass transfer experiments, and Nu_{gn} correlation Eq.(2.13) **(from [11])**

A graphical comparison of the three correlations (2.12), (2.13) and (2.14) is proposed in Fig. 2-10, for the primary coolant at 655ºC (Pr = 14.3) and 30 < Re < 3000, corresponding to typical values attained during a LOFC transient. We see that there is a considerable scatter between the Gnielinski correlations and KTA equation, up to a factor

of 2. The Wakao and Gnielinski correlations agree better, with relative difference below the scatter of experimental points presented Fig. 2-9 and minimum for small Re.

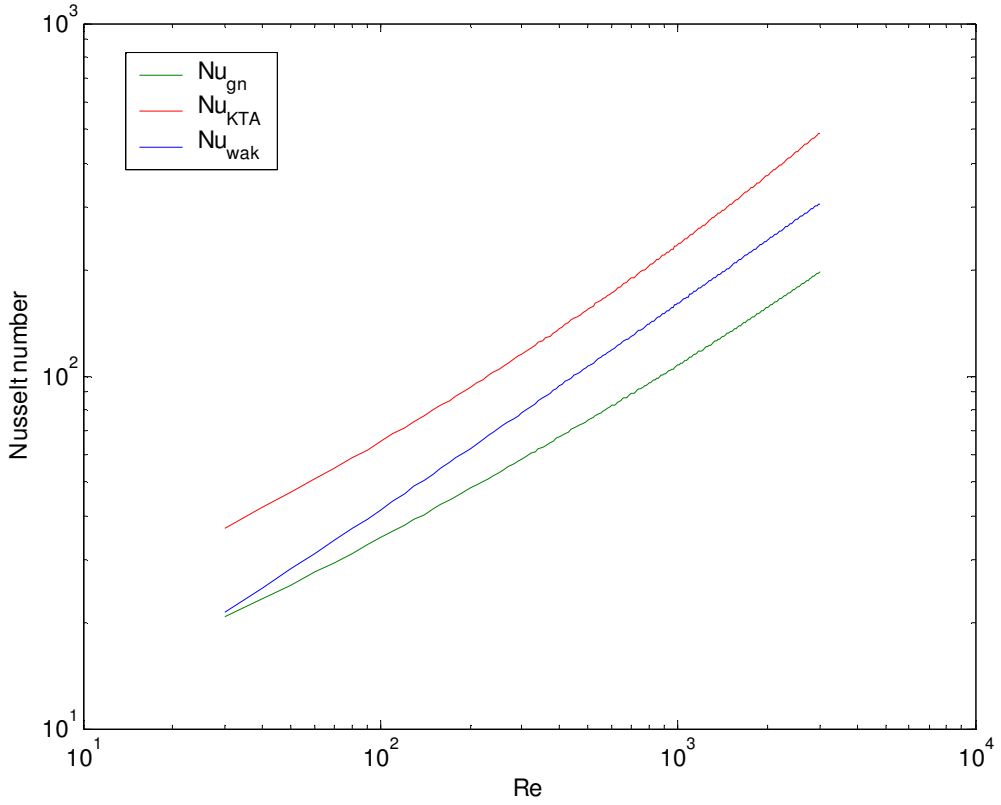

Figure 2-10: Comparison between Nu_{wak}, Nu_{gn}, Nu_{KTA} for Pr = 14.3

As an additional factor, under LOFC and ATWS conditions buoyancy forces are likely to be significant, and mixed convection may augment the heat transfer above the predictions from these correlations. Using the notations adopted in the mixed convection sections, the following Grashof and Rayleigh number can be calculated (Eqs.(2.1)-(2.2)):

$$Gr_d = 1.3\times10^7$$
$$Gr_{dL} = 1.8\times10^5$$
$$Ra_{dL} = 2.5\times10^6$$

where $d = 1.5\times d_p$ is the hydraulic diameter in the bed. These values have been plotted in the flow map Fig. 2-3. Even if this map is only adapted for flows in ducts, this first approach shows that mixed convection effect is likely to be important in the PB-AHTR pebble bed. No studies of mixed convection in internally heated packed sphere beds are available as yet.

This brief literature review suggests that the careful study of heat transfer for pebble beds with conditions similar to those of the PB-AHTR (Pr = 10-20 like flibe, and 30 < Re < 3000 region), and with mixed convection effects, which could be studied using

a reduced size pebble bed and stimulant oils at much lower temperature (see for instance [13]), could be warranted.

This report will use the Kaviany correlation, as it is easier to perform scaling analysis thanks to its less complicated functional form.

3) RELAP5-3D implementation

According to the RELAP5-3D manual, appendix A, it is possible to input pressure losses coefficients in a given junction between two volumes as a known function of $Re_{d,}$ where d is the hydraulic diameter of the junction. The possible functional expression is:

$$K(\mathrm{Re}) = b + a\,\mathrm{Re}^{-c}$$

It is therefore possible to model correctly a whole pebble bed by dividing it into elementary volumes, calculating equivalent K values based on the geometry of the junction between these volumes (using Ergun equation (2.10) which has a compatible expression) and of course deactivating the standard pressure loss correlations for pipes.

It is however not possible to input any special heat transfer correlations, different from standard geometries such as plates or tubes: it is only possible to input a history of heat transfer coefficients h(t). However, using Wakao-Kaviany correlation Eq.(2.12), we see that the possible time dependency of Nu is as follows:

$$Nu \sim 1.1\mathrm{Re}^{0.55}\,\mathrm{Pr}^{1/3} = 1.1\left(\frac{\dot{m}(t)d}{\mu(T(t))A}\right)^{0.6}\left(\frac{\mu(T(t))c_p}{k}\right)^{0.33} = A\dot{m}(t)^{0.6}\mu(T(t))^{-0.22}$$

where A is approximately independent of time.

During the ATWS/LOFC transients, flibe viscosity ranges from $8\text{x}10^{-5}$ Pa sec to $3\text{x}10^{-5}$ Pa sec (corresponding to temperatures ranging from 600 to 900ºC), which means a typical variation of Nu due to viscosity changes of 25%. As for mass flow rates, the simulations show relatively constant flow rates in the natural circulation loop, with typical values of 100 kg/s for the LOFC and 150 kg/s for the ATWS (see the final chapter for mass flow graphs). Moreover, as both viscosities and flow rates tend to decrease over time as the system cools down, their effects on Nu compensate each other as seen above.

This means it is possible to input an approximately correct history of heat transfer coefficients according to Wakao relation. Using an average value for the dynamic viscosity of $5.5\ \text{x}10^{-5}$ Pa sec, the heat transfer coefficients can be input depending on the flow conditions, as shown in Table 2-2. Again, it should be emphasized that these correlations neglect mixed convection effects, and thus likely underestimate the actual pebble heat transfer coefficients (particularly for LOFC and ATWS conditions).

	Flow rate (kg/s)	Nu	h (W/m^2K)
Steady State	9200	293	5365
LOFC	100	21	390
ATWS	150	27	490

Table 2-2: Comparison of heat transfer coeffficients in the pebble bed during various flow conditions

For the LOFC transient for instance, the following h(t) was given as input to RELAP5-3D to compute the heat transfer on the pebble surface:

- $t < 500$ s, steady state, $h = 5365$ W/m^2s
- $t > 500$ s, pump trip and natural circulation, $h = 390$ W/m^2s

D. Conclusions

This chapter finds that for the conditions expected for LOFC and ATWS transients in the PB-AHTR, available correlations for heat transfer in the PHX modules and the pebble bed may have significant uncertainty. At the current stage of conceptual design, this does not create major issues in evaluating the response of the PB-AHTR to LOFC and ATWS transients, because the PHX heat transfer area can be adjusted easily during detailed design to account for changes in the heat transfer coefficients, and the thermal response of the pebble bed is not highly sensitive to the convective heat transfer coefficient.

Laminar mixed convection occurs inside the PHX tubes and experimental data are available to support some correlations for heat transfer. But a possible transition to turbulence at a low Reynolds number warrants some additional investigation in the same Pr, Re and Gr region.

The flow on the buffer side of the PHX is turbulent mixed convection, with buoyancy dominating the overall heat transfer. Correlations are available, but no data has been presented to validate these correlations for high Pr, and for large tube aspect ratios ($L/d > 100$).

Pebble bed pressure loss correlations are very well documented, and show a rather good agreement with experimental data (within 15%). On the other hand, Nusselt number correlations for pebble-bed heat transfer show a considerable scatter, are not well documented for intermediate range Pr = 5-20, and do not consider mixed convection effects that may be important in increasing the pebble heat transfer coefficients in the PB-AHTR.

The standard RELAP5-3D heat transfer package has been used to model heat transfer in the PHX: compared to the mixed convection correlations, this overestimates the heat transfer coefficient on the primary side of the PHX tubes by around a factor of 2, while it predicts an approximately correct value for the Nusselt of the external flow of buffer salt.

For the pebble bed heat transfer, the expected slow variation of mass flow in the primary loop during transients allows the heat transfer coefficient in the bed to be input as a step function of time.

The Ergun equation for pressure losses inside the pebble bed has been implemented exactly into the PB-AHTR core RELAP model. The Ergun equation for pebble bed pressure losses is clearly sufficient, because losses in the fluid diode and form losses in locations with area changes dominate the total pressure drop under LOFC and ATWS conditions.

Bibliography

[1] J. S. Goodling, R. I. Vachon, W. S. Stelpflug, and S. J. Ying, *Radial porosity distribution in cylindrical beds packed with spheres*, Powder Technology **35**, 23 (1983).

[2] A. J. Sederman, P. Alexander and L. F. Gladden, *Structure of packed beds probed by Magnetic Resonance Imaging*, Powder Technology **117**, 255 (2000).

[3] Ergun S., *Fluid Flow Through Packed Columns*, Chem. Eng. Prog. **48**, 89 (1952).

[4] Macdonald I. et al., *Flow through Porous Media-the Ergun Equation Revisited*, Industrial engineering chemistry fundamentals **18**, 199 (1979)

[5] Van den Akker H.E.A. and Mudde, R.F., *Fysische Transport verschijnselen I*, Delft University Press (1996)

[6] S.J. de Zwaan, *The Liquid Salt Pebble Bed Reactor, A new high-temperature nuclear reactor*, Delft University of Technology (2006), PNR-131-2005-008.

[7] K. Kugeler and R. Schulten, *Hochtemperaturreaktortechnik*, edited by Springer-Verlag (1989)

[8] German Nuclear Safety Standards Commission, *Reactor Core Design of High-Temperature Gas-Cooled Reactors. Part 3: Loss of Pressure through Friction in Pebble Bed Cores*, KTA 3102.3 (1981)

[9] Kaviany M., *Principles of Heat Transfer in Porous Media*, edited by Springer-Verlag (1995)

[10] Alazmi, *Analysis of Variants Within the Porous Media Transport Models*, Journal of heat transfer **122**, 303 (2000)

[11] Gnielinski V., *Warme- und Stoff ubertragung in Festbetten*, Chem. -Ing. -Tech **52**, 228-236 (1980).

[12] German Nuclear Safety Standards Commission, *Reactor Core Design of High-Temperature Gas-Cooled Reactors. Part 2: Heat Transfer in Spherical Fuel Elements*, KTA 3102.2 (1983)

[13] P. Bardet and P.F. Peterson, *Design of Scaled Integral Experiments for High Temperature Liquid Salt and Helium Fluid Mechanics and Heat Transfer*, in Eleventh International Topical Meeting on Nuclear Reactor Thermal Hydraulics, Avignon, France, October 2-6 2005

[14] Hallman T.M., Trans. *Combined forced and free laminar transfer in vertical tubes with uniform internal heat generation*, Trans. ASME **77**, 1831 (1956).

[15] Holman J.P., *Heat transfer*, Mc Graw Hill (2002).

[16] Metais B., Eckert E.R.G., *Forced, mixed and free convection regimes*, Journal of heat transfer (1964).

[17] Hallman T.M., *Experimental study of combined forced and free laminar convection in a vertical tube*, National Aeronautics and Space Administration (1961), NASA TN-D-1104.

[18] Scheele G.F. et al., *Effect of natural convection instabilities on rates of heat transfer at low reynolds numbers*, AIChE journal **9**, 183 (1963).

[19] Sadık Kakaç, Yaman Yener, *Convective Heat Transfer*, CRC Press (1995).

[20] S Kakaç, RK Shah, W Aung, *Handbook of single-phase convective heat transfer*, Wiley (1987).

[21] Morton, *Laminar convection in uniformly heated vertical pipes*, Journal of fluid mechanics **8**, 2, 227 (1960)

[22] L. Tao*, Heat transfer of combined free and forced convection in circular and sector tubes*, Appl. Sci. Res. **9A**, 357-368 (1960).

[23] *RELAP5-3D© Code Manual Volume IV: Models and Correlations*, INEEL-EXT-98-00834 (2005)

[24] Franz Paul Hauk, *Design and set-up of a high temperature flow loop for the investigation of heat transfer and pressure loss in a mixed convection regime flow of higher Prandtl number molten salt simulants*, Diplomarbeit, UC Berkeley & Technische Universität München (2006)

[25] Aicher T. and Martin H., *New correlations for mixed turbulent natural and forced convection heat transfer in vertical tubes*, Int. J. Heat Mass Transfer **40**, 3617-3626 (1997).

[26] A. Bejan, *Convection Heat Transfer.* (John Wiley & Sons, 1984).

[27] Jackson J. D., Cotton M. A. and Axcell B. P., *Studies of mixed convection in vertical tube*, Int. J. Heat and Fluid Flow **10**, 2-15 (1989).

[28] Celata G. P., D'Annibale F., Chiaradia A. and Cumo, *Upflow turbulent mixed convection heat transfer in vertical pipes*, M., Int. J. Heat Mass Transfer **41**, 4037-4054 (1998).

3. Assessment of scaled experiments for the PB-AHTR

This chapter focuses on the design of scaled experiments to reproduce important phenomena that are central in understanding more precisely the thermal hydraulics of the PB-AHTR system under various operational or accidental conditions. The design of the AHTR system incorporates features that minimize the distortion of key phenomena as the reactor is scaled upward in power. These features include modularity for its decay heat removal system and the use of Froude number scaling for component heights to preserve buoyancy effects with changing power output.

One experiment design presented here is an integral effects test (IET) called the Pebble Recirculation Experiment (PREX), a "bench-top" scale experiment using a simulant fluid (water) that has been constructed in the UCBNE Thermal Hydraulics Laboratory to reproduce the integrated fluid and pebble bed dynamics of pebble recirculation in the PB-AHTR.

The second part of this chapter is centered on the analysis of important phenomena during Loss of Forced Cooling transients, where natural circulation in the primary loop provides cooling of the residual core power. Based on this analysis, the design of a reduced-scale AHTR Pilot Plant (APP) reactor is presented. The APP is a small reactor that reproduces natural circulation behavior of the prototypical scale PB-AHTR reactor.

A. Scaling for the Pebble Recirculation Experiment (PREX)

The PB-AHTR is a novel concept because it uses a coolant (flibe) and fuel (pebbles) that have been studied and applied individually in actual nuclear systems, but have not been combined together. This provides a major advantage, because well understood and qualified fuel (pebble TRISO fuel), as well as high temperature materials (Alloy 800H clad with Hastelloy N), can be used, avoiding the need for a long-term fuel and materials development programs. However, while pebble recirculation is well understood and demonstrated for gas-cooled pebble bed reactors, pebbles recirculation has not been studied for liquid-salt cooled pebble bed reactors. But a number of important similarities exist with the dynamics of a granular pebble bed with a helium coolant, and an extensive literature is available that tackle these issues [1].

No previous studies have been made for pebble beds operating under the conditions of the PB-AHTR. In contrast to the gas-cooled designs, pebbles float in the liquid-salt coolant at the temperatures associated with normal operation and transients. This means that assessment of the feasibility of the refueling/defueling processes is needed, as well as a study of the phenomena that affect behavior of the pebbles in the bed and in the recirculation system.

This section focuses on the design of the Pebble Recirculation Experiment (PREX), a relatively simple, scaled experiment to reproduce the dominant phenomena that occur a pebble bed at a reduced scale, shown schematically in Fig. 3-1. Because it is difficult to assess or reproduce the friction forces between pebbles in liquid salts, only the

interaction between the fluid and the pebbles are being considered: this means this study is fully adequate to investigate the physics of pebbles during refueling/defueling, but lacks some elements to understand fully the dynamics of the pebble bed motion.

1) Scaling of hydrodynamic phenomena in the bed

To scale an experiment to reproduce pebble/coolant interactions, there are two forces to consider:

- Drag forces between the pebble and the liquid. They depend on the non dimensional drag coefficient C_D, which is a function of the Reynolds number $\mathrm{Re} = \frac{\rho_f V_p d_p}{\mu}$, where ρ_f is the density of the flibe coolant, μ its viscosity and V_p the relative velocity of the pebble and the coolant.
- Buoyancy forces on pebbles

The terminal velocity of the pebble in the flow is given by setting the buoyancy and drag two forces equal:

$$\frac{\pi}{6} d_p{}^3 \left(\rho_f - \rho_p\right) g = C_D \frac{\pi}{8} \rho_f d_p{}^2 V_p^{\infty 2}$$

Here d_p is the pebble diameter and ρ_p the density of the pebble. We can express the terminal velocity of the pebble V_p^{∞} as a factor of the fluid flow velocity U and in term of a Froude number relative to D:

$$V_p^{\infty 2} = \frac{4}{3}(1-\frac{\rho_p}{\rho_f})\frac{1}{C_D}\frac{g d_p}{U^2}U^2 = \left(\frac{4}{3}(1-\frac{\rho_p}{\rho_f})\frac{1}{C_D}Fr^{-2}\right)U^2$$

The velocities ratio V_p^{∞}/U can be reproduced in the PREX experiment if:

- Fr is conserved,
- Re is conserved in all the parts of the experiment (same C_D)
- the ratio of coolant/pebble densities is conserved

These requirements correspond to the generally accepted scaling criteria to reproduce correctly hydrodynamic behavior for the motion of solid particles in fluids.

Let X_R be the scaling ratio between the scaled and the full-scale, prototypical systems (i.e. $X_R = X_{exp}/X_{fs}$). The choice of the simulant coolant (water in this case) and temperature fixes these ratios for all thermophysical properties. The length scale l_R and the mass flux scale q_R are the only variables that still need to be determined. Scaling to preserve the Reynolds and Froude numbers yields the following requirements for the length and mass flux scales:

$$1 = q_R l_R \frac{1}{\mu_R} \qquad 1 = \frac{q_R}{\sqrt{l_R}}\frac{1}{\rho_R}$$

With the viscosities and densities of flibe at 700ºC and of water at 25ºC, we obtain:

$$l_R = 0.4628 \qquad q_R = 0.3496 \tag{3.1}$$

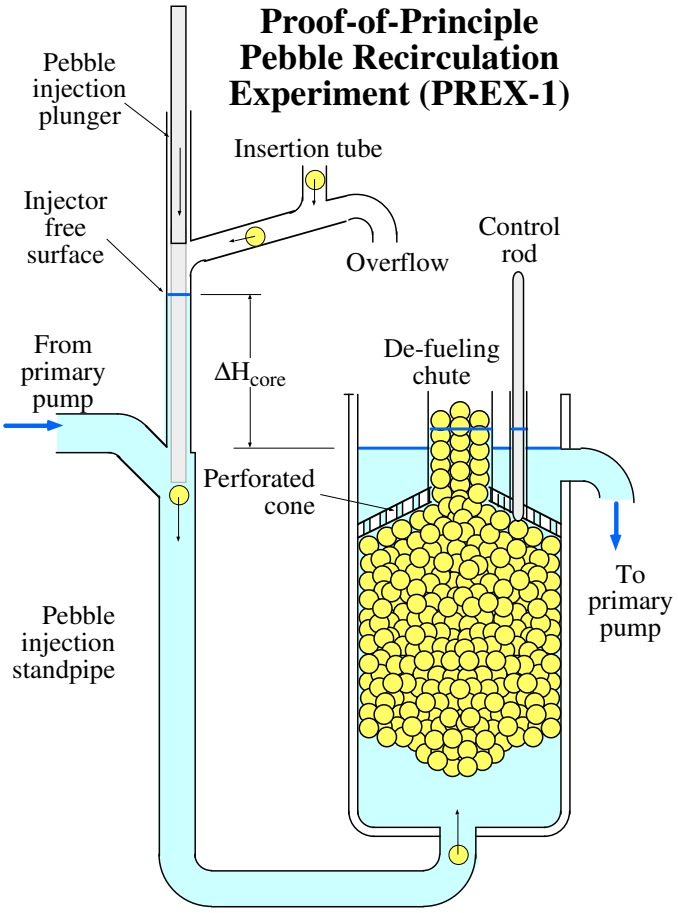

Figure 3-1: Schematic diagram showing the PREX experiment layout. The design flow rates reproduce Re and Fr in locations where there are pebbles, i.e. in the injection standpipes and the "core"

In the APP the ratio of the pebble density to the flibe coolant density in the APP depends upon the manufacturing of the pebble, which can produce pebbles with densities ranging from 1680 to 1940 kg/m^3, and on the temperature of the flibe coolant.

For salt temperatures ranging from 600°C to 850°C the ratio of pebble to salt density ranges from 0.846 to 0.901 for the lowest pebble density, to 0.911 to 0.971 for the highest pebble density. The polypropylene spheres used in PREX have a density of 843 kg/m^3, so the ratio of the pebble density to the water density in PREX is 0.844. Thus the density ratio in PREX more closely matches that for the low pebble density for APP, and for higher pebble densities (and higher flibe temperatures) the actual terminal rise velocity of the APP pebbles will be lower than the scaled rise velocity for PREX.

2) Sizing of the PREX system

As the scaling parameters derived are still very large (0.46 for the length ratio, from Eq. (3.1)), it is not practical for an initial demonstration experiment like PREX to try to reproduce the full-scale AHTR core, which has 1.2 million pebbles and is 6.4m high. It was decided to reproduce the core of a small scale test and research reactor, the AHTR Pilot Plant (APP), using a scaled pebble bed experiment. The APP is an 86 MWth pebble bed AHTR design, intended to be used as a demonstration and test reactor for initial development of the PB-AHTR. It is discussed in greater detail in the next section of this chapter.

PREX uses reduced area scaling, so that it reproduces coolant flow velocities for a fraction of the total APP coolant flow area and bed area. Because the APP has four cold legs and injection standpipes, it is a natural choice for PREX to simulate only one injection standpipe of the APP and one-quarter of the core flow area, i.e. adopting the area scaling $l^2/4$. The reduced area scaling for the reactor pebble core results in some distortion of the pebble bed dynamics due to the difference in the shape of the core, however these were considered to be acceptable given that PREX is a proof-of-principal experiment for pebble recirculation. Applying such scaling to the APP system yields to the following set of design parameters:

	APP	PREX
Total height	2.13 m	0.99 m
Flow area	2.29 m^2	0.12 m^2
Pebble d_p	6 cm	2.54 cm
Pebble density	1680 - 1810 kg/m^3	843 kg/m^3
Coolant density	1987 - 1865 kg/m^3	999 kg/m^3
Number of pebbles	26,000	8,300
Inlet temperature	600°C	~20°C
Outlet temperature	704°C	~20°C
Re	905	842
Head loss	11.9 cm	5.5 cm

Table 3-1: Comparison of baseline core design parameter for the APP and the PREX. The pebble density can be controlled in the manufacturing process. The flibe coolant density is for the range from 600°C to 900°C.

	APP	PREX
Total height	3 m	1.38 m
Flow area	0.126 m^2	0.0068 m^2
Diameter	20 cm	9.3 cm
Re	54800	54800
Head loss	15.7 cm	7.3 cm

Table 3-2: Comparison of baseline cold leg and pebble injection standpipe designs for the APP and PREX

The choice of commercially available 1-inch (2.54-cm) polypropylene balls introduces a small distortion in the scaled pebble diameter, which implies a small change in the pebble Reynolds number (<10%). The pebble Froude number is also slightly affected and is underestimated by approximately 5 %.

The flow rate of fluid in the APP is 3.6 kg/s (compared to 190 kg/s in the APP), or 3.6 liter/sec (98 liter/sec in the APP). These are reasonable design parameters, and thus the PREX experiment was constructed in a relatively short amount of time during the '06 fall semester in the UCBNE Thermal Hydraulics Laboratory.

3) Results of the recirculation experiment

PREX provided a successful demonstration of the recirculation of pebbles in a liquid-salt cooled pebble bed reactor (see Figs. 3-2 and 3-3). One interesting issue is the relative unpredictability of the trajectory of the pebbles injected into the lower inlet plenum, as the injected coolant flow establishes large-scale recirculation patterns, which carry pebbles toward the periphery of the bed as they bounce against the bottom of the bed.

Further studies will include the design of a diffuser to break up the large-scale recirculation flows in the inlet plenum area and improve the injection of pebble at the bottom of the bed. Also of interest is the test of insertion of insertion forces for a control rod into the pebble bed, which can be studied in the PREX experiment. PREX will also be used to measure pressure losses and benchmark the pebble-bed pressure loss correlations used in simulations.

Figure 3-2: View of PREX, fully loaded with pebbles.

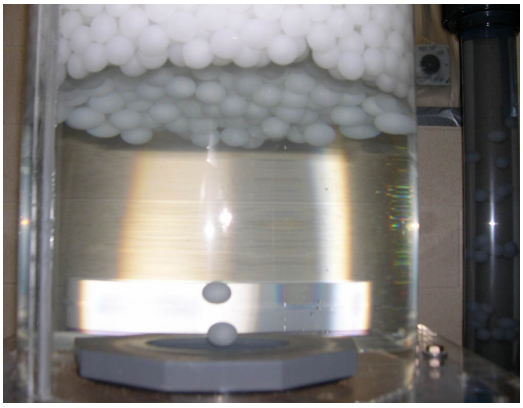

Figure 3-3: Successful injection of pebbles at the bottom of the bed; note the concave shape of the bottom of the pebble bed generated by the pebble landing pattern.

B. Scaling for the AHTR Pilot Plant (APP)

This section presents scaling analysis and design for the PB-AHTR Pilot Plant (APP), a reduced-scale test reactor designed to replicate important phenomena that would occur in the prototypical scale 2400-MW_t PB-AHTR. The APP is a key element of the AHTR development program: the 86-MW_t APP is a reduced height, reduced area, reduced power, and accelerated time IET for the nuclear performance of the PB-AHTR. The most important role for the APP is to study key reliability related phenomena (such as salt chemistry control) and key operations and maintenance activities (such as pebble recirculation and sorting). However, it is also desired that the APP be capable of replicating key operational transients expected for the full-scale PB-AHTR.

The scope of this preliminary APP design work is to investigate the proper scaling of the APP facility to reproduce the behavior of the prototypical PB-AHTR during a loss of forced cooling (LOFC) transient. This scaling is optimized so that the APP can replicate the most important safety related parameters in the transient, and in particular, so that the normal and peak metal temperatures experienced by key components (primary pumps, PRACS heat exchangers, etc.) are reproduced during the LOFC transient. The scaling presented here provides preliminary design parameters for the APP height, area, power and time scaling.

To achieve accelerated time scaling for the LOFC transient, it is anticipated that LOFC tests in the APP will be initiated following a programmed ramping of the reactor power, designed to reduce the inventory of longer-lived fission products so that the subsequent drop in decay heat generation occurs over the correct accelerated time frame.

While for most components the length, area, and thickness can be scaled to better preserve the transient phenomena experienced by the prototypical PB-AHTR, the pebble diameter used in the APP is set to be identical to the prototypical plant (e.g., 6-cm diameter). This allows APP to be used to study fuel fabrication, burn up and performance. The resulting distortion of the LOFC transient phenomena from the pebbles diameter scaling is discussed in the following subsections.

Following a top-down approach, the PB-AHTR reactor system was divided into several subsystems and components. Starting for first principle balance equations of the LOFC transient and scaling analysis already made in the literature, pertinent non-dimensional groupings were derived. They were used to properly scale the APP experimental reactor.

1) Physical description of the prototypical and scaled systems

The PB-AHTR system was hierarchically divided in an approach similar to the one of Zuber [2]. However, because the whole system is very complicated, this analysis was limited to a rather high level.

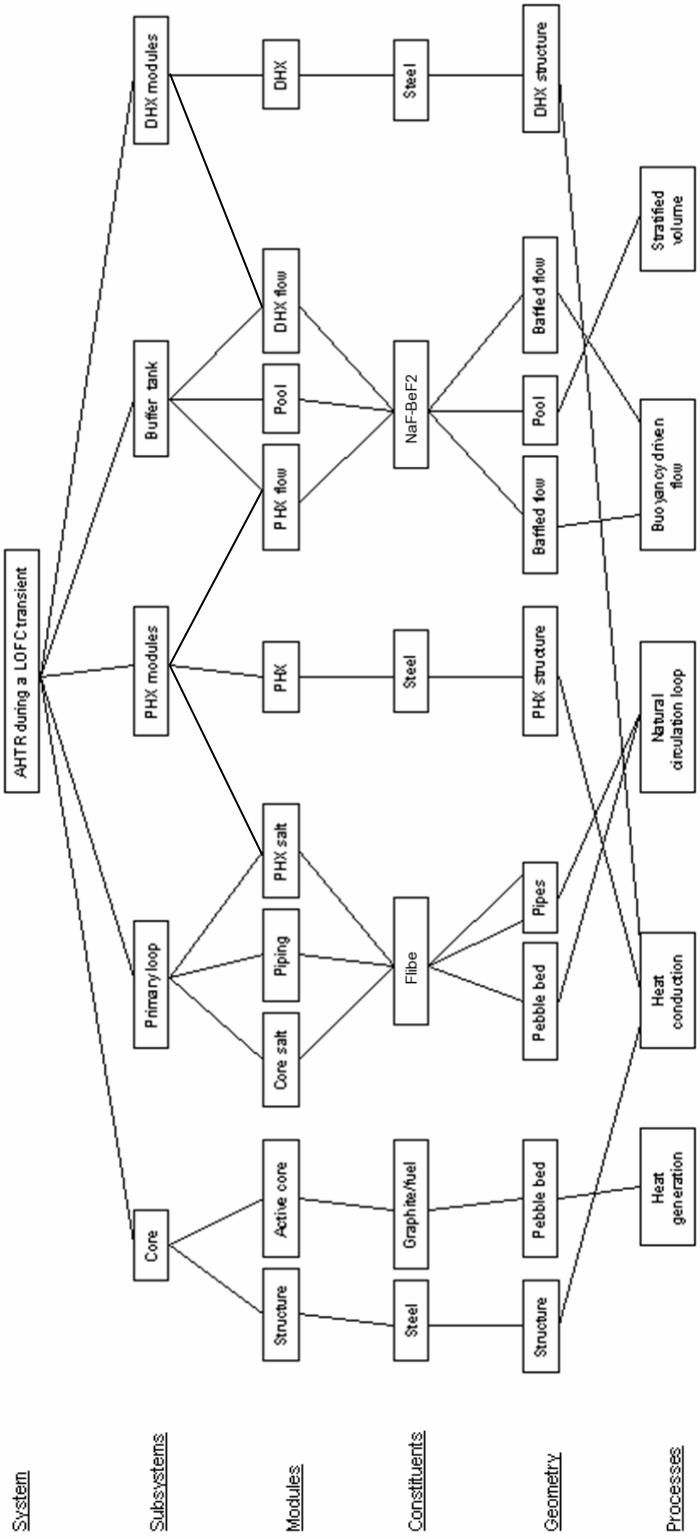

Figure 3-4: Hierarchical subdivision of the PB-AHTR reactor under a LOFC transient

For instance, one can make Zuber's two-tiered scaling analysis for lower level phenomena (for instance, stratified volumes - see Peterson et al. [3]). In this work, we applied this type of analysis and introduced the pertinent non-dimensional groupings as characteristic parameters for rather broad physical processes. Figure 3-4 describes the categorization of subsystems and modules that was used in this study. For more precision on details of the design, please refer to the tables Annex A.

Based on Fig. 3-4, for the LOFC transient where the primary loops (primary pumps and IHX's) do not participate, the AHTR system can be divided into two main sets of subsystems:

- A natural circulation loop for primary coolant that includes the core and the primary coolant inside the PHX modules.
- The buffer salt tank, including the buffer salt inside the baffled region of the PHX and DHX

Heat can be transferred between the reactor core and the buffer salt by two means:

- Forced convection driven by natural circulation flow in the primary side of the PHX, conduction through the PHX tubes and forced convection driven by natural circulation of buffer salt in the baffled region of the PHX. The PHX surface area has been designed to remove slightly less than 1% of the full power (around 20 MW) for a typical temperature drop between the inlet and outlet of the PHX modules of 100ºC, and a primary salt flow rate of around 100 kg/s.
- Conduction though the outer reflectors and the reactor vessel, and natural convection from the reactor vessel to the buffer salt. Assuming a 0.9 m thick graphite outer reflector, 5 cm thick steel reactor vessel wall, the primary thermal resistance is that of the graphite reflector, with h ~ 45 W/(m^2K). With a heat transfer surface of around 160 m^2 and a ΔT of around 200K, then the maximum heat transfer by this mean is found to be 1.4 MW, well below the heat removal capacity of the PHX natural circulation loop. If some bypass flow of primary salt occurs between the reactor vessel and reflector, this heat loss rate through the reactor vessel could increase, however this can be compensated for by reducing the size of the PHX.

In the models developed here, only the heat transfer by the PHX modules is considered, and heat losses through the reactor vessel wall to the buffer salt are neglected.

2) Relevant time scales

To have a correct idea of magnitude of the inertia terms in the differential equations describing the system, relevant time scales should be considered. Several characteristic times can be defined for the LOFC / ATWS transient:

- Core transient heat generation time constant. Previous calculations for the prismatic NGNP core [4] showed that the decay heat decreases from 7% just after scram to 3.5% after around t_{decay} ~ 100 s. Under ATWS conditions, the reduction of core power

output will occur over larger time scales due to the slower shutdown of the fission process.

– Pebble thermal response time constant. This characteristic time heat transfer through the pebble by thermal diffusion is derived from the pebble Fourier number: $t_p = d_p^2 / \alpha_p \sim 200\,\mathrm{s}$.

– Core primary salt residence time. This time is $t_{core} = \rho_f \varepsilon A_c L_c / \dot{m}_f$. Under natural circulation, a flow rate of 100 kg/s is expected and corresponds to the cooling power necessary to remove around 1% of the full power, with a temperature variation of 100ºC from the inlet to the outlet of the core. This flow rate gives $t_{core} \sim 2000$ s, much longer than the core transient heat generation and pebble thermal equilibration time constants.

– PHX manifold pipes primary salt residence time. The residence time of the primary salt in the manifold pipes connecting the core and the PHX. $t_{pipes} \sim 10\,\mathrm{s}$

– PHX modules primary salt residence time. The residence time of the primary salt in the PHX system is $t_{phx} = \rho_f A_{f,phx} L_{phx} / \dot{m}_f$, which gives $t_{phx} \sim 200\,s$. Due to the similar physical properties of the buffer and primary salts, the time of residency of the buffer salt in the PHX is expected to be also approximately 200 s.

– PHX modules buffer salt residence time. With a mass flow of 100 kg/s, the residence time of the buffer salt in the buffer tank is 20,000 s.

This analysis shows that the evolution of the system depends on phenomena with very different time scales (from 10 sec to 20,000 sec). As we are primarily interested in the average core outlet temperature and the peak fuel temperature, two time periods can be distinguished in the study of the LOFC cooling transients:

1) $0 < t < 2000\,s$. The core primary salt that was present at the beginning of the transient has not been fully discharged yet. Thus the PHX operation has not yet influenced the average core outlet temperature. This phase is characterized by lower mass flow and lower heat generation (compared to steady state operations) that tend to diminish the temperature differences between the pebbles and the flibe. Thus, this phase will be called the fuel thermal equilibration phase. A reasonable characteristic time to use for this phase is the pebble thermal response time, $t_p = 200$ s.

2) $t > 2000\,s$. The primary salt can circulate multiple times in the natural circulation loop formed by the core and the PHX. Because the residence time for the primary salt in the PHX is very short compared to in the residence time the reactor core, the PHX can be modeled using the assumption of quasi-steady-state behavior. This phase will be called the long-term heat removal phase. A reasonable characteristic time scale to use for this phase is the residence time of primary salt in the core $t_0 = 2000$ s.

In the following studies, the time scale t_0 will be changed depending on the phases considered during the transient. This is to assure that the inertia terms of the form $\partial X^* / \partial t^*$ will be approximately 1, with $\Delta T_0 =$ 100ºC and t_0 as temperature and time scales. These estimates of the inertia terms can be confirmed by observing the temperature evolutions given by RELAP5-3D simulations in chapter 5, which clearly

show an initial phase of rapid rise of temperature (the fuel equilibration phase), followed by a slower rise up to the maximum temperature experienced in the transients (the long-term heat removal phase).

This approach will give two estimates of the loop non-dimensional parameters. This will help identifying the relevant phenomena during these two important time phases.

3) Governing equation and non dimensional parameters

a) Natural circulation in the primary loop

Definition of parameters

From Levy's book [5] and Ishii's papers [6] and [7], we have the following momentum equation in the natural circulation loop formed by the core and the PHX:

$$\rho \sum_i L_i \frac{dU_i}{dt} = -\int \rho g \, dz - \sum_i \left(\frac{f_i L_i}{d_i} \frac{\rho U_i^2}{2} + K_i \frac{\rho U_i^2}{2} \right)$$

U_i represent the velocities in each of the components of the loop, L_i and d_i their lengths and diameters. The volumic forces integral is over the different elevations of the natural circulation loop. f_i are the friction factors in each sections amd K_i are the corresponding form losses.

According to Levy, this approach has already been used to estimate the global momentum balance in a specific complex system, the Simplified Boiling Water Reactor (SBWR).

During a LOFC transient, the loop is expected to have a typical mass flow rate of 100 kg/s. We can then assess the flow regime in each of the system components, assuming coolant properties at 700ºC, and using the reactor design parameters presented Annex A.

- Core pressure losses

The Darcy friction coefficient in the core is assumed to follow the Ergun correlation already described in Eq. (2.10) (the factor 1/2 is here to reconciliate the correlation with the Darcy definition of the friction factor used here):

$$\frac{f_c}{2} = \frac{1-\varepsilon}{\varepsilon^3}\left(180\frac{1-\varepsilon}{\mathrm{Re}_c} + 1.8\right) \quad with \quad \mathrm{Re}_c = \frac{\dot{m} d_p}{\mu A_c}$$

where the Reynolds number is based on the pebble diameter. A typical value under LOFC conditions is $\mathrm{Re}_c = 30$

– PHX pressure losses

During the LOFC transient we have $Re_{phx} = 230$, corresponding to laminar flow (although buoyancy forces may result in turbulent mixed convection). Assuming laminar flow,

$$f_{phx} = \frac{64}{\mathrm{Re}_{phx}}$$

– PHX inlet and outlet manifold pipes pressure losses

Here $Re_{pipe} = 14000$ and the Blasius correlation can be used:

$$f_p = \frac{0.316}{\mathrm{Re}_{pipe}^{1/4}}$$

For scaling purposes we can separate the laminar pressure losses (proportional to $\dot{m}$) and the other losses:

$$\left(\sum_t \frac{L_i}{A_i}\right)\frac{d\,\dot{m}}{dt} = g\rho\beta\int_0^{Lc}(T_h - T_c)\,dz - \left(\frac{64\mu L_{phx}}{2d_{phx}^2\rho A_{phx}} + 180\frac{(1-\varepsilon)^2}{\varepsilon^3}\frac{\mu L_c}{d_p^2\rho A_c}\right)\dot{m}$$
$$-\left(\sum_i \frac{K_i}{2\rho A_i^2} + 1.8\frac{1-\varepsilon}{\varepsilon^3}\frac{L_c}{d_p\rho A_c^2} + f_p\frac{L_{pipe}}{2d_{pipe}\rho A_{pipe}^2}\right)\dot{m}^2$$

Following Levy we introduce a characteristic mass flow rate $\dot{m}_0 = 100\,kg/s$, a characteristic temperature difference $\Delta T_0 = 100^\circ K$ and a characteristic inertia time t_0 that will depending on the transient phase.

Defining a non-dimensional mass flow $\dot{m}^* = \dot{m}/\dot{m}_0$, average temperature difference in the loop $\overline{\Delta T}^* = \int_0^{L_c}(T_h - T_c)\,dz / L_c\Delta T_0$, and time $t^* = t/t_0$, we obtain the following dimensionless equation:

$$\frac{d\dot{m}^*}{dt^*} = Ri_1\overline{\Delta T}^* - F_2\dot{m}^* - F_3\dot{m}^{*2} \qquad (3.2)$$

with a modified Richardson number:

$$Ri_1 = t_0\frac{g\rho\beta L_c\Delta T_0}{\dot{m}_0\sum_i \frac{L_i}{A_i}}$$

a laminar loss term, proportional to $\dot{m}$:

$$F_2 = t_0 \frac{1}{\rho \sum_i \frac{L_i}{A_i}} \left(\frac{64 \mu L_{phx}}{2 d_{phx}^2 A_{phx}} + 180 \frac{(1-\varepsilon)^2}{\varepsilon^3} \frac{\mu L_c}{d_p^2 A_c} \right)$$

and a turbulent losses term roughly proportional to $\dot{m}^2$:

$$F_3 = t_0 \frac{\dot{m}_0}{\rho \sum_i \frac{L_i}{A_i}} \left(\sum_i \frac{K_i}{2 A_i^2} + 1.8 \frac{1-\varepsilon}{\varepsilon^3} \frac{L_c}{d_p A_c^2} + f_p \frac{L_{pipe}}{2 d_{pipe} A_{pipe}^2} \right)$$

Evaluation of parameters

Calculating these parameters for the PB-AHTR design, with parameters presented in Annex A, gives the results during the two main transient phases shown Table 3-3.

	Ri_1 (buoyancy)	F_2 (laminar loss)	F_3 (turbulent loss)
Phase 1	150	2.2	49
Phase 2	1500	22	490

Table 3-3: Characteristic non dimensional parameters of the natural circulation loop

The pressure losses due to the fluidic diode and to area changes account for approximately 80% of the total turbulent losses. Solving the momentum equation:

$$\dot{m}^* = \frac{1}{2} \left[\sqrt{\left(\frac{F_2}{F_3} \right)^2 + 4 \left(\frac{Ri_1}{F_3} \overline{\Delta T}^* - \frac{1}{F_3} \frac{dm^*}{dt^*} \right)} - \frac{F_2}{F_3} \right]$$

Considering the value of the non dimensional groupings F_2, F_3 and Ri_1, the laminar losses can be neglected, allowing the following simplification:

$$\dot{m}^* = \sqrt{\frac{Ri_1}{F_3} \overline{\Delta T}^*}$$

where F_3 depends on area changes and the fluidic diode characteristics, and not on the actual configuration of the loop.

b) Energy conservation in the core

Neglecting multi-dimensional flow in the core, two energy conservation equations can be written for the pebble bed and the primary salt:

– For one representative pebble at a given elevation in the bed, assuming the heat losses to the flibe are uniformly distributed on the surface and considering q'''_{ave} the

volumic heat generation in the total core volume, the temperature distribution in the pebble T_p follows :

$$\rho_p c_p \frac{\partial T_p}{\partial t}(r,t) = k_p \nabla^2 T_p(r,t) + \frac{q'''_{ave}}{1-\varepsilon} f(\frac{r}{r_c})$$

$$-k_p \nabla T_p(r=r_c) = \frac{Nu_p k_f}{d_p}(T_p(r=r_c) - T_f)$$

where $\rho_p c_p$ is the volumetric heat capacity of the pebbles, and $h_c = Nu_c k_f / d_p$ is the average surface heat transfer coefficient between the pebble bed and the liquid salt coolant. The function $f(r/r_c) = (1-\varepsilon) q'''(r) / q'''_{ave}$ provides the power distribution inside the pebble, depending on the type of pebble used in the reactor (homogeneous or annular design).

Using the non-dimensional time $t^* = t/t_0$, temperature $T^* = T/\Delta T_0$ and position $r^* = r/d_p$ the dimensionless version of this heat conduction/convection problem is:

$$\begin{aligned} \frac{\partial T_p^*}{\partial t^*} &= Fo_4 \nabla^{*2} T_p^* + Hg_5 f\left(r^*\right) \\ -\nabla^* T_p^*(r^*=1) &= Bi_6 (T_p^*(r^*=1) - T_f^*) \end{aligned} \tag{3.3}$$

with the following significant groupings:

- Fourier number, an estimate of the influence of heat conduction inside one pebble after a characteristic time t_0:

$$Fo_4 = t_0 \frac{k_p}{\rho_p c_p d_p^2}$$

- Heat generation number, ratio of the total power generated in the core, and the cooling capability of the flibe flow:

$$Hg_5 = t_0 \frac{q'''}{(1-\varepsilon)\rho_p c_p \Delta T_0}$$

- Biot number, ratio of the thermal resistance of the liquid-salt boundary layer around the pebble and the thermal resistance of conduction in the pebble itself:

$$Bi_6 = \frac{Nu_p k_f}{k_p}$$

For the salt, writing a simple one dimensional advective balance equation for the temperature of the flibe T_f at a given elevation x of the core yields:

$$A_c \varepsilon \rho_f c_f \left(\frac{\partial T_f}{\partial t} + U_c \frac{\partial T_f}{\partial x} \right) = \frac{Nu_p k_f}{d_p} L_c^w (T_p(x, r_c) - T_f(x))$$

where $L_c^w = 6(1-\varepsilon)A_c / d_p$ is the wetted perimeter of the pebble bed. Making this equation non-dimensional yields:

$$A_7 \frac{\partial T_f^*}{\partial t^*} + \dot{m}^* \frac{\partial T_f^*}{\partial x^*} = St_8 (T_p^*(x, r_c) - T_f^*(x)) \tag{3.4}$$

where the non dimensional time $t^* = t / t_0$, position $x^* = x / L_c$, temperatures $T^* = T / \Delta T_0$ and mass flow $\dot{m}^* = \dot{m} / \dot{m}_0$ are used. This equation involves the Stanton number, which represents the ratio of the convective heat transfer rate between the core and the primary and the cooling capacity of the salt by advection:

$$St_8 = \frac{Nu_p k_f L_c^w L_c}{d_p} \frac{1}{\dot{m}_0 c_f}$$

A_7 is represents the inertia of the flibe in the core:

$$A_7 = \frac{\varepsilon A_c L_c \rho_f}{\dot{m}_o} \frac{1}{t_0}$$

Evaluating these different non dimensional groupings gives (considering the LOFC decay heat generation, and taking the volumic heating rate at 5% of full power during the first phase, 1% during the second phase), as shown in Table 3-4.

	Fo_4 (pebble conduction)	Hg_5 (heat generation)	Bi_6 (convection / conduction)	A_7	St_8 (convection / advection)
Phase 1	0.87	0.67	0.68	9.0	27
Phase 2	8.7	1.3	0.68	0.90	27

Table 3-4: Characteristic non-dimensional parameters for the heat transfer inside the core

During the equilibration phase, the Fourier, heat generation and inertia terms are generally of the same order of magnitude (around 1), so that the interaction of conduction and thermal inertia cannot be neglected in the pebble transient heat balance. During the later stage of the transient, the heat generation number and the inertia terms become small compared to Fo_4: the pebble temperature distribution should then quickly be flattened out by heat conduction. The Biot number is always of order unity, which means that the same temperature differences in the pebble and in the thermal boundary layer around it can be expected.

During the fuel thermal equilibration phase of the transient, the Stanton number St_8 and inertia term A_7 are comparable and dominate the advective term, whereas in the subsequent long term heat removal phase the Stanton number is the dominant grouping. This means it is expected that the pebble/coolant temperature difference will equilibrate and become significantly smaller than the earlier $\Delta T_0 = 100$ K during the initial phase. This assumption has been confirmed by RELAP5-3D simulations discussed in chapter 5.

c) Energy conservation in the PHX

First, the thermal conductance between the primary coolant and the buffer salt in the PHX can be evaluated for typical conditions under LOFC:

$$\frac{Nu_{f,phx}k_f}{d_{f,phx}} = 570 \text{ W/m}^2\text{K}$$

$$\frac{k_{steel}}{e_{phx}} = 10,000 \text{ W/m}^2\text{K}$$

$$\frac{Nu_{buf,phx}k_{buf}}{d_{buf,phx}} = 740 \text{ W/m}^2\text{K}$$

This means the heat conduction through the PHX module structure can be neglected, and the heat transfer from the primary to the buffer can be described in term of the following advection equations:

– In the primary salt:

$$A_{f,phx}\rho_f c_f \left(\frac{\partial T_f}{\partial t} + U_{f,phx} \frac{\partial T_f}{\partial x} \right) = -\left(\left(\frac{Nu_{f,phx}k_f L^w_{f,phx}}{d_{f.phx}} \right)^{-1} + \left(\frac{Nu_{buf,phx}k_{buf} L^w_{buf,phx}}{d_{buf.phx}} \right)^{-1} \right)^{-1} (T_f(x) - T_{buf}(x))$$

where $L^w_{f,phx}$ is the wetted perimeter inside the PHX tubes, and $L^w_{buf,phx}$ the wetted perimeter outside the PHX tubes.

– In the buffer salt:

$$A_{buf,phx}\rho_{buf} c_{buf} \left(\frac{\partial T_{buf}}{\partial t} + U_{buf,phx} \frac{\partial T_{buf}}{\partial x} \right) = \left(\left(\frac{Nu_{f,phx}k_f L^w_{f,phx}}{d_{f.phx}} \right)^{-1} + \left(\frac{Nu_{buf,phx}k_{buf} L^w_{buf,phx}}{d_{buf.phx}} \right)^{-1} \right)^{-1} (T_f(x) - T_{buf}(x))$$

These two equations can be made non-dimensional:

$$\begin{aligned} A_{11} \frac{\partial T^*_f}{\partial t^*} + m^*_f \frac{\partial T^*_f}{\partial x^*} &= \frac{1}{1/St_9 + 1/St_{10}} (T^*_f - T^*_{buf}) \\ Ti_{13} \left(A_{12} \frac{\partial T^*_{buf}}{\partial t^*} + m^*_{buf} \frac{\partial T^*_{buf}}{\partial x^*} \right) &= -\frac{1}{1/St_9 + 1/St_{10}} (T^*_f - T^*_{buf}) \end{aligned} \qquad (3.5)$$

with the same non dimensional parameters than introduced above. The following dimensionless groupings are used:

– Stanton number in the PHX tubes primary coolant:

$$St_9 = \frac{Nu_{f,phx}k_f L^w_{f.phx} L_c}{d_{f,phx}} \frac{1}{\dot{m}_0 c_f}$$

- Stanton number in the buffer salt flowing around the PHX tubes:

$$St_{10} = \frac{Nu_{buf,phx} k_{buf} L^{w}_{buf.phx} L_c}{d_{buf,phx}} \frac{1}{\dot{m}_0 c_f}$$

- Inertia ratios for the PHX primary side and buffer sides:

$$A_{11} = \frac{A_{f,phx} L_c \rho_f}{\dot{m}_0} \frac{1}{t_0} \quad A_{12} = \frac{A_{buf,phx} L_c \rho_{buf}}{\dot{m}_0} \frac{1}{t_0}$$

- Specific thermal inertia ratio between the primary coolant and the buffer salt:

$$Ti_{13} = \frac{c_{buf}}{c_f}$$

Values for these characteristic groupings are shown in Table 3-5.

	St_9 (Primary convection / advection)	St_{10} (Buffer convection / advection)	A_{11}	A_{12}	Ti_{13}
Phase 1	4.8	6.2	1.2	1.7	0.63
Phase 2	4.8	6.2	0.12	0.17	0.63

Table 3-5: Characteristic grouping for the heat transfer in the PHX modules

The grouping $Ti_{13} \times A_{12}/A_{11} = 0.9$ has a value very close to 1, which means that the thermal inertia of the primary salt in the PHX and of the buffer salt in the PHX have similar magnitude.

The relatively similar values of St_9 and St_{10} show that convection in both the primary and in the buffer is important phenomena in the heat transfer through the PHX modules.

During the long term heat removal phase, the small values of the PHX inertia terms confirm that the PHX modules should behave as a quasi steady state heat sink.

4) Scaling of the primary loop: proposal for an APP design

The AHTR Pilot Plant (APP) is a reduced-size, reduced power version of the PB-AHTR. The APP uses the same coolant and fuel and is scaled to have the same core inlet and outlet temperatures. This means all the important physical properties used in the previous analysis remain the same, and that the APP materials are subjected to prototypical conditions.

The goal is to find a APP design for which the eleven dimensionless groupings presented above (all except the laminar friction losses) will remain very close to the values in PB-AHTR. For that, there are several non-dimensional design parameters to adjust (following Ishii's scaling guidelines):

l_R = vert. length ratio m_R = mass flow rate ratio d_{pR} = pebble dia. ratio
a_R = flow area ratio q_R = power density ratio d_{phxR} =PHX tubes dia. ratio

We assume that the factors l_R and a_R are applied uniformly in the APP core, which means that inertia ratios A_7, A_{11} and A_{12} in the heat equations (3.4) and (3.5) are conserved. For the same reasons, the turbulent losses can also be replicated faithfully assuming also that a correctly scaled fluidic diode is possible.

Scaling the other groupings yields the following equations given in Table 3-6. For the heat transfer in the core and the PHX, the following correlations were used:

- In the core, the Wakao correlation (2.12), for which $Nu_p \propto \mathrm{Re}_c^{0.6}$
- In the PHX primary salt, laminar forced convection following $Nu_{f,phx} \propto \mathrm{R}\, a_{d_f^{phx} L}^{0.25}$, where d_f^{phx} is the PHX tube diameter and the Rayleigh number is based on the diameter and the axial temperature gradient, according to (2.5)
- In the PHX buffer salt, turbulent free convection following the Churchill-Chu correlation for which $Nu_{buf,phx} \propto \mathrm{R}\, a_{d_{buf}^{phx}}^{0.33}$, where d_{buf}^{phx} is the hydraulic diameter, according to (2.8)

In the PHX, the scaling ratios for the hydraulic diameter and the pitch should be $d_{phx,R}$, as the relative surface of the primary and the buffer salt heat exchanger areas must be conserved.

Numbers	Ri_1	F_3	Fo_4	Hg_5	Bi_6	A_7
1 =	$\frac{l_R a_R^2}{m_R^2}$	1	$\frac{l_R a_R}{m_R d_{pR}^2}$	$\frac{q_R l_R a_R}{m_R}$	$\mathrm{Re}_c^{0.6} = \left(\frac{m_R d_{pR}}{a_R}\right)^{0.6}$	1

Numbers	St_8	St_9	St_{10}	A_{11}	A_{12}	Ti_{13}
1 =	$\left(\frac{m_R d_{pR}}{a_R}\right)^{0.6} \frac{l_R a_R}{m_R d_{pR}^2}$	$\left(\frac{d_{phxR}^4}{l}\right)^{0.25} \frac{a_R l_R}{m_R d_{phxR}^2}$	$\left(d_{phxR}^3\right)^{0.33} \frac{a_R l_R}{m_R d_{phxR}^2}$	1	1	1

Table 3-6: Scaling equations and the corresponding conserved groupings

Scaling the Richardson number Ri_1 and heat generation Hg_5 yields:

$$\frac{m_R}{a_R} = l_R^{1/2} \quad q_R = l_R^{-1/2} \tag{3.6}$$

Characteristic circulation time is of the form $\rho_f A_c L_c / \dot{m}_f$, which means that the time scaling ratio is:

$$t_R = l_R^{-1/2} \tag{3.7}$$

Using the same fuel in the APP than in the full scale reactor imposes $d_{pR} = 1$, and this gives the following distorted ratios on the heat transfer inside the pebble:

$$Fo_{4R} = l_R^{1/2} \quad Bi_{6R} = l_R^{0.3} \quad St_{8R} = l_R^{0.8}$$

The expressions of St_9 and St_{10} show that it not possible to find the correct d_{phxR} that conserves both St_9 and St_{10}. However, the choice $d_{phx,R} = l_R^{0.375}$ introduces only small distortion on the non dimensional parameters ratios:

$$St_{9R} = l_R^{-0.125} \quad St_{10R} = l_R^{+0.125}$$

Choosing l_R = 1/3 and a_R = 1/16 yields the design parameters for the PHX modules and the reactor core shown in Table 3-7.

	APP	**Full scale**
Top elevation of the active region	0 m	0 m
Active height	2.13 m	6.4 m
Inlet plenum height	0.67 m	2 m
Outlet plenum height	0.83 m	2.5 m
Total diameter	1.7 m	6.8 m
Horizontal area	2.27 m^2	36.3 m^2
Total number of pebbles	26,000	1.2 million
Bed packing fraction	60%	60%
Pebble diameter	6 cm	6 cm

PHX modules	**APP**	**Full scale**
Top elevation of heat transfer region	-0.17 m	-0.53 m
Active height	1.07 m	3.2 m
Number of modules	1	8

Baffled diameter	63 cm	88 cm
Primary salt flow area	0.123 m^2	1.96 m^2
Number of tubes	421	4000
Tube diameter	1.93 cm	2.5 m
Buffer salt flow area	0.184 m^2	2.94 m^2
Pitch between tubes	2.7 cm	3.5 cm
Buffer flow hydraulic diameter	2.88 cm	3.74 cm

PHX inlet/ outlet manifolds	**APP**	**Full scale**
Combined length	1.4 m	4.2 m
Flow area	0.0079 m^2	0.126 m^2
Number of pipes	1	16
Pipe diameter	10 cm	10 cm

Table 3-7: Design parameters for the APP compared to the prototypical PB-AHTR

The APP will function at a reduced maximum power of 86 MW_t, and with a mass flow rate of 3.6% of the full power design, when solving Eq.(3.6) for m_R and q_R. The characteristic time of evolution of any transient would be multiplied by a factor $(1/3)^{1/2}$ = 0.58, from Eq.(3.7). This means the transient will be nearly twice as fast.

Table 3-8 gives an overview of the flow conditions in the APP reactor during a LOFC transient, while Table 3-9 summarizes the distortions compared to the full scale version.

Component	Core	PHX manifold	PHX tubes	PHX buffer flow
APP Reynolds	17	8,300	100	3000
Full scale Reynolds	30	14,000	230	6500

Table 3-8: Typical values of Re during LOFC transients in the APP

Numbers	Ri_1	F_3	Fo_4	Hg_5	Bi_6	St_7
N_{APP}/N_{FS}	1	1	0.58	1	0.72	0.42

Numbers	A_8	St_9	St_{10}	A_{11}	A_{12}
N_{APP}/N_{FS}	1	1.15	0.87	1	1

Table 3-9: Value of the ratios of non dimensional groupings for the APP and the full scale PB-AHTR

In summary, all the relevant groupings are reproduced relatively closely except the numbers related to the heat transfer in the pebble. Using the prototypical pebble diameter in the APP results in lower convection characteristic numbers (Stanton and Biot groupings), and a smaller Fourier conduction parameter.

Bibliography

[1] Chris H. Rycroft, Gary S. Grest, James W. Landry, and Martin Z. Bazant, *Analysis of Granular Flow in a Pebble-Bed Nuclear Reactor*, Cond. Mat. (2006).

[2] Zuber N., *A Hierarchical, Two-Tiered Scaling Analysis*, 1991), Appendix D, NUREG/CR-5809, EGG-2659.

[3] Peterson P.F., *Scaling for integral simulation of mixing in large, stratified volumes*, Nuclear engineering and design **186**, 213 (1998).

[4] P.E. MacDonald et al., *NGNP Preliminary Point Design - Results of the Initial Neutronics and Thermal-Hydraulic Assessments*, Idaho National Engineering and Environmental Laboratory (September 2003), INEEL/EXT-03-00870 Rev. 1.

[5] Salomon Levy, *Two phase flow in complex systems* (Wiley-IEEE, 1999), p. 448.

[6] Ishii M., Kataoka I., *Similarity Analysis and Scaling Criteria for LWR's Under Single-phase and Two-phase Natural Circulation*, NUREG/CR-3267 (ANL-83-32) (1983)

[7] Kocamustafaogullari G., Ishii M., *Scaling criteria for two-phase flow loops and their application to conceptual 2× 4 simulation loop design*, Nuclear technology **65**, 146 (1984).

4. Neutronics study – Reactivity feedback calculations

This chapter describes the reactivity feedback calculations used in the transient modeling of the PB-AHTR with RELAP5-3D. The MCNP model used to calculate the reactivity feedback coefficients relies on more extensive work by Max Fratoni on the PB-AHTR core neutronics design (see reference [1]), and was first created for a NE-255 project with two other students, Steve Mullet and Jeff Seifried.

The reactivity model presented here considers only the reactivity feedback created by temperature variations of the fuel and the flibe coolant, for two variations of the pebble design. It does not include more detailed analysis on fuel burn up effects or optimization of the fuel performance. The reactivity calculations are for fresh fuel, i.e. pebbles that have just been loaded inside the core containing no fissions products or transuranics: hence, the feedback coefficients based on this model apply to a PB-AHTR at startup conditions, and approximately for a PB-AHTR with an equilibrium core.

A. Pebble fuel characteristics and the MCNP model

1) Description of the pebbles

The design parameters used for the TRISO particles can be found in chapter one. Every particle contains a pure uranium dioxide fuel kernel at an enrichment of 10%, with a density of 10.5 g/cm^3 and the other material layers have already described in chapter one, Table 1-6.

The standard, homogeneous pebble is described in Table 4-1 and Fig. 4-1. An annular variation of the pebble has also been introduced in the study of PB-AHTR fuel. For the annular pebble, the homogeneous central fuel zone is replaced by a central graphite sphere, surrounded by an annular fuel zone and a 0.5-cm thick protective graphite coating: in both cases, the fuel zone is a 1.6 g/cm^3 graphite matrix containing similar TRISO particles. By making the packing density of TRISO particle in the fuel zone higher, the annular pebble can contain the same mass of heavy metal as a homogeneous pebble, but with a smaller fuel zone.

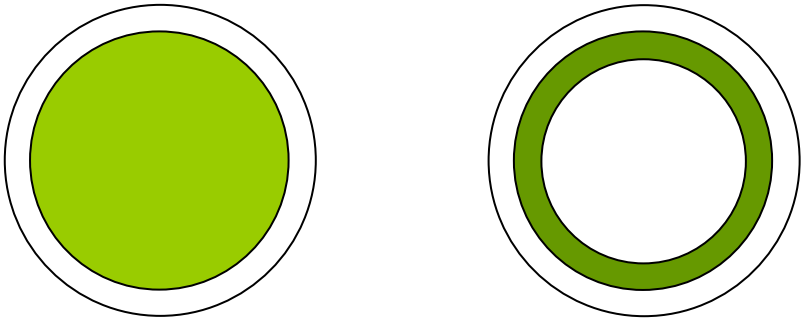

Figure 4-1: Left, homogeneous pebble with a 10% TRISO packing fraction fuel zone (light green). Right, annular pebble with a 20% TRISO packing fraction fuel zone (darker green)

The purpose of this annular geometry is to lower the peak temperature inside the pebble and the stored energy in the fuel. This reduces the rise in the coolant temperature that occurs during the fuel equilibration phase following the initiation of a LOFC or ATWS transient. In steady state, the central graphite zone will have a nearly flat temperature distribution. It is necessary, however, to investigate the differences in neutronics of the homogeneous and annular pebble designs.

	Graphite kernel radius	Fuel zone outer radius	TRISO packing fraction	Coating thickness	Total number of TRISO	Total mass of heavy metal U	U to C molar ratio
Standard pebble	N/A	2.5 cm	10 %	0.5 cm	17150	10.4 g	14
Annular pebble	1.984 cm	2.5 cm	20 %	0.5 cm	17150	10.4 g	14

Table 4-1: Numerical characteristics of the two pebble designs

As shown Table 4-1, the two pebble designs contain exactly the same quantity of heavy metal, carbon and silicon, as the pebble size and the total number of TRISO particles do not vary. This means that the difference in neutronics behavior only depends on the geometrical disposition of the fuel, and on the actual temperature distribution. In the annular design, the TRISO fuel is more concentrated and is bordered by a rather large graphite kernel that acts as a moderator: this should decrease parasitic capture in the fuel and favor moderation, which will increase the k_{inf}. With similar flibe flow rate and steady state heat removal, the fuel operates at at a lower temperature. Due to the negative fuel Doppler feedback we expect, this should increase k_{inf}. On the other hand, the fuel is now closer to the flibe coolant, where ^{6}Li has a large capture cross section, which could decrease k_{inf}.

2) MCNP5 modeling approach

We used MCNP5 to implement a model of the flibe cooled AHTR pebble bed and calculate the variation of reactivity due to temperature changes. Two temperature zones were considered in this analysis: the pebble zone and the coolant zone. In each zone, a uniform temperature distribution was assumed. The fuel and coolant temperature were changed, and k_{inf} variations were observed.

Both Doppler broadening of resonances and temperature-induced density changes of materials affect criticality, and were studied here. This required the use of different cross-section libraries for each temperature (except for ^{19}F, which cross-sections were only available at room temperature) and different total densities of the coolant at each temperature.

Due to a limited neutronics cross-section library, a uniform sampling of the temperature ranges could not be performed. It was decided to perform runs at fuel and coolant temperature intervals of 100°C, where possible. The graphite scattering kernel,

for example, was only available at 200°C increments in these temperature regions. When this happened, it was decided to simply use the closest cross-section available.

The actual range of fuel and coolant temperatures was determined by heat transfer considerations. The coolant temperature was assumed to vary between 600ºC and 900ºC, and analysis of the heat transfer coefficient on the surface shows a maximum reasonable temperature difference between the coolant and fuel being 200ºC. In view of the availability of MCNP5 libraries at these temperatures on the UCB DECF grid where the calculations were performed, it was decided to perform the following calculations:

	T_{fuel} = 900K	T_{fuel} = 1000K	T_{fuel} = 1100K	T_{fuel} = 1200K	T_{fuel} = 1300K
T_{flibe} = 900 K	X	X	X		
T_{flibe} = 1000 K		X	X	X	
T_{flibe} = 1100 K			X	X	X

Table 4-2: Selection of flibe/fuel temperatures for the MCNP5 calculations

The pebble bed structure contains two levels of heterogeneity that make it more challenging to model using Monte Carlo methods:

- there is around 17,000 TRISO particles (~1 mm) in one pebble (~6 cm)
- there is around 1.2 million pebbles (~6 cm) in the AHTR core (~6 m)

To have a MCNP model that can be run quickly, only the TRISO/pebble heterogeneity level was reproduced in the calculation: this analysis calculates k_{inf} for an infinite array of fuel pebbles inside the flibe coolant. Arguing that neutron leakage does not depend much on temperature variations, the variation of k_{inf} should reproduce accurately the reactivity variations of the whole core. This approach is however not adapted for calculations on a pebble bed that has already been in use for some time, as in this case the burnup level is not homogeneous in the core, and instead it increases with increasing elevation in the core.

This heterogeneity level, with 17,000 TRISO particles, implies that at least the same number of neutron histories should be simulated before iterating the fission source distribution: 25,000 was the number chosen in this calculation.

3) TRISO particle model

One TRISO particle is described in the MCNP deck according to the parameters of the Table 1-6 of chapter 1. It is placed at the center of a graphite matrix cubic cell (density 1.6 g/cm^3), which main dimension *a* corresponds to a given packing fraction:

- 10% packing fraction: a = 1.56 mm
- 20% packing fraction: a = 1.24 mm

This cubic structure is then reproduced along its three principal directions to give a cubic lattice of parameter *a*. The parameter *a* is greater than the diameter of one TRISO particle (0.9 mm in this model). Using a cubic lattice permits packing fractions up to $\pi/6 = 0.524$, well above the value needed for study of PB-AHTR pebbles (see Fig. 4-2)

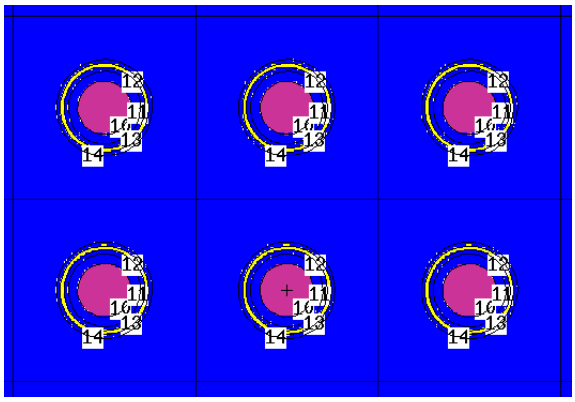

Figure 4-2: Cross section of the TRISO cubic lattice, for 10% packing fraction. The material layers in the TRISO particles are distributed according to Table 1-6 from chapter 1

4) Single pebble model

The cubic TRISO lattice is then restricted to the fuel zone, which is placed in a single pebble which possible geometries are described in Tab. 4-1 (homogeneous pebble represented in Fig. 4-4). The flibe coolant and the pebble bed structure still need to be reproduced. For simplicity, it was decided to use an infinite crystal lattice with matching porosity ε to simulate the pebble bed.

The appropriate lattices should have a minimum porosity below ε_{bed} = 40%, which leaves the following options:

- fcc or hcp lattices, $\varepsilon_{min} = 0.259$
- bcc lattice, $\varepsilon_{min} = 0.320$
- center of an hexagonal cell, as illustrated Fig. 4-3, $\varepsilon_{min} = 0.395$

The two first options are theoretically better, as they allow an isotropic representation of the bed. On the other hand, the third option shows anisotropy between the directions inside the hexagonal plane, and the direction orthogonal to it. It is however easier to model using only one pebble and reflective boundary conditions on the hedges of the hexagonal polyhedron, and thus this option was used in the analysis.

Adopting the notations of Fig. 4-3, the incidence of this anisotropy can be decreased by choosing equal vertical and horizontal pitches, so that one given pebble is at equal distances from neighboring pebbles in the vertical direction and in the horizontal plane. After some algebra, the correct pitch can be derived:

$$p = d_p \frac{1}{\sqrt{3}} \sqrt[3]{\frac{\pi}{1-\varepsilon}} \tag{4.1}$$

For ε_{bed} = 40%, this gives p/d_p = 1.0025: the closed pack dimensions are expanded by only 2.5%.

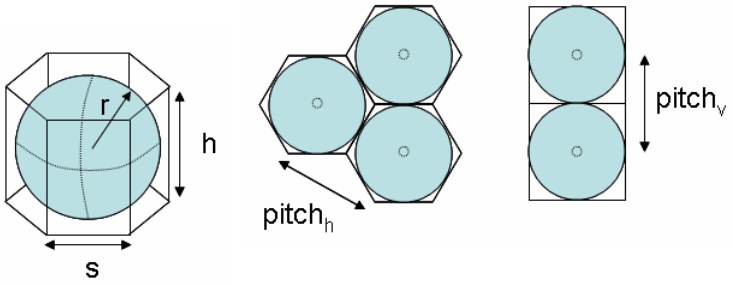

Figure 4-3: Different views of the pebble hexagonal cell

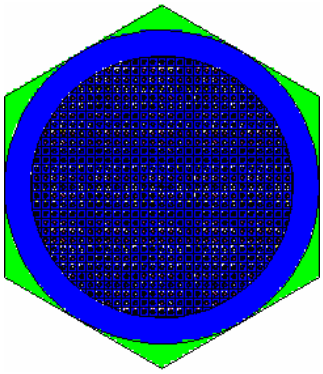

Figure 4-4: A homogeneous pebble is filled with the TRISO lattice, surrounded by flibe and put in a hexagonal cell

B. Coolant and fuel temperature reactivity feedback

1) Raw results

Figures 4-5 and 4-6 give k_{inf} variations relative to the coolant and the fuel temperatures. The standard deviation estimates for each k_{inf} calculation are typically around $\sigma = 0.0003 = 30$ pcm. The error bars on the graphs represent the 95% confidence interval for each estimate of k_{inf} ($\pm 1.96\sigma$).

The colored lines represent a linear fit of k_{inf} variations relative to the coolant T at constant fuel T (left graphs), or vice-versa (right graphs). All of these fits approximate the k_{inf} values within the statistical error bars.

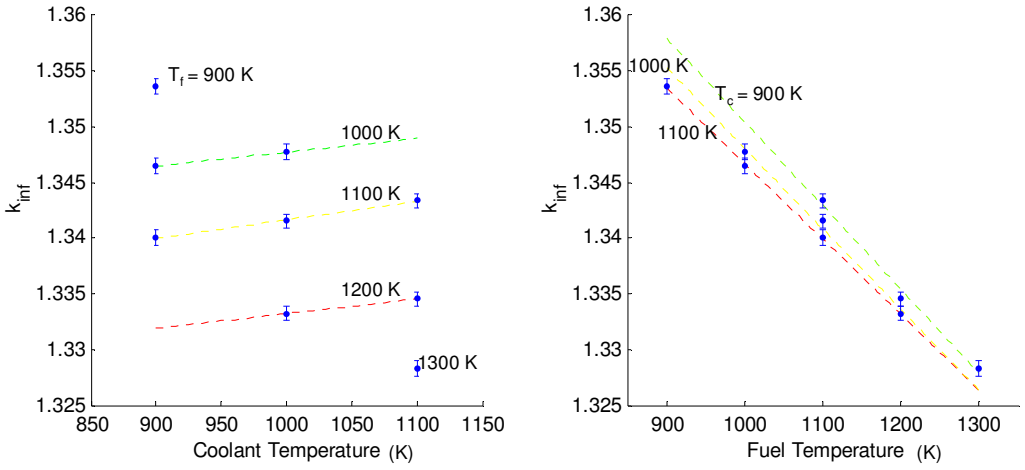

Figure 4-5: k_{inf} variations for the homogeneous pebbles

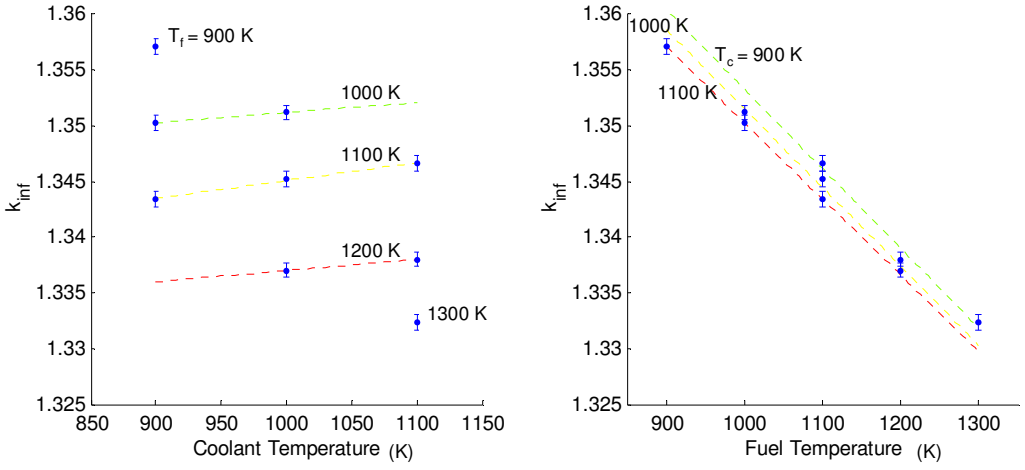

Figure 4-6: k_{inf} variations for the annular pebbles

We see that at given fuel and coolant temperatures, k_{inf} for the annular pebbles is around 0.005 = 500 pcm above the k_{inf} for the homogeneous pebbles. For this fuel design, both fuels present slightly positive coolant temperature feedback, which is compensated by a much larger negative fuel temperature feedback. Furthermore, the amplitudes of variation on the curves look pretty similar for the two fuels. More recent work by M. Fratoni has shown that negative coolant temperature feedback can be achieved by using pebbles with higher heavy metal loading. This higher heavy metal loading would also be expected to increase the Doppler resonance absorption, and make the fuel temperature coefficient yet more negative as well.

2) Fit of the reactivity map

Homogeneous pebbles

T_f (K)	α_c (pcm/K)
1000	+0.91
1100	+1.23
1200	+0.99

T_c (K)	α_f (pcm/K)
900	-5.02
1000	-5.38
1100	-5.62

Annular pebbles

T_f (K)	α_c (pcm/K)
1000	+0.68
1100	+1.18
1200	+0.75

T_c (K)	α_f (pcm/K)
900	-5.05
1000	-5.25
1100	-5.32

Table 4-3: Reactivity feedback at different fuel and coolant temperatures, for the homogeneous and the annular pebbles

If we consider that most of the temperature induced reactivity variations in the pebble bed are due to variations of k_{inf} rather than effects of neutron leakage, then good estimates of the core temperature reactivity feedback coefficients are:

$$\alpha_c = \frac{1}{k_{\inf}} \frac{\partial k_{\inf}}{\partial T_c} \qquad \alpha_f = \frac{1}{k_{\inf}} \frac{\partial k_{\inf}}{\partial T_f} \tag{4.2}$$

Table 4-3 provides numerical values for the α's calculated here.

We see that reasonable values for the reactivity temperature coefficients in the range $900\text{K} < T_c < 1100\text{K}$ and $1000\text{K} < T_f < 1200\text{K}$ are:

$$\begin{aligned} \alpha_c &= +1 \text{ pcm/K} \\ \alpha_f &= -5 \text{ pcm/K} \end{aligned} \tag{4.3}$$

The relatively small positive coolant feedback is balanced by a much larger negative fuel feedback. At higher heavy metal loading, the coolant feedback coefficient can be made negative as well. The most recent calculations of Max Fratoni have shown that $\alpha_c \sim -1$ pcm/K can be obtained, and potentially more negative fuel reactivity coefficient values as well. Furthermore, the burn up level of the fuel in the pebbles also influences these feedback coefficients: equilibrium pebbles apparently have a lower (more negative) coolant coefficient.

Because the actual temperature reactivity feedback will depend on the details of the fuel design, the coefficients were varied parametrically in the RELAP5-3D simulations to determine the sensitivity of the peak coolant outlet temperature to these values.

Bibliography

[1] M. Fratoni, E. Greenspan and P.F. Peterson, *Neutronic and Depletion Analysis of the PB-AHTR,* in Global '07, Advanced Nuclear Fuel Cycles and Systems, Boise, Idaho (2007).

5. RELAP simulations of the PB-AHTR

RELAP5-3D is the latest version of an Idaho National Laboratory system code that has been successfully used to model many light water reactor and modular helium reactor transients. Even though RELAP5-3D was initially designed specifically for water/steam two phase flow systems, it also supports single-phase flow problems. There has recently been an interest to extend the capacity of this code to handle different coolants for different reactor systems.

In 2005-2006, a new version of RELAP5-3D was developed by INL with specific libraries for the thermophysical properties of liquid salts such as flibe, flinak and $NaBF_4$-NaF. This relatively new version was used here for the transient analysis of Berkeley's PB-AHTR baseline design, a high-temperature variant of this baseline design, as well as possible power uprates. This study includes modeling of the steady state operating condition, the loss of forced cooling (LOFC) transient and the anticipated transient without scram (ATWS) coinciding with loss of forced cooling.

A. Nodalization of the system

Figure 5-1 provides an overview of the RELAP5-3D nodalization of the PB-AHTR. Following the RELAP nomenclature, the system is divided into three main functional categories:

- *Hydrodynamic system.* This includes fluid nodal volumes and junctions between them. In this model of the AHTR, there are two distinct hydrodynamic systems, because the primary coolant and the buffer salt are physically separate.
- *Heat structures.* These structures represent all the solid interfaces linked to the hydrodynamic components. They conduct and store heat and they can have heat generation.
- *Heat generation model.* This part can be very simple, with options for a steady state power source, a fixed decay heat curve, or more complex model using point kinetics reactivity feedback, for instance

This chapter focuses on the precise description of each of the components of the PB-AHTR for the baseline design described in Annex A. More specific information on the RELAP5-3D code structure can be found in several references ([1, 2] and particularly in [3]).

1) Hydraulic description

RELAP5-3D describes hydraulic components by dividing them into elementary control volumes, linked by junctions. Mass and energy are averaged on volumes, whereas momentum is averaged at the junctions. The conservation equations are then integrated

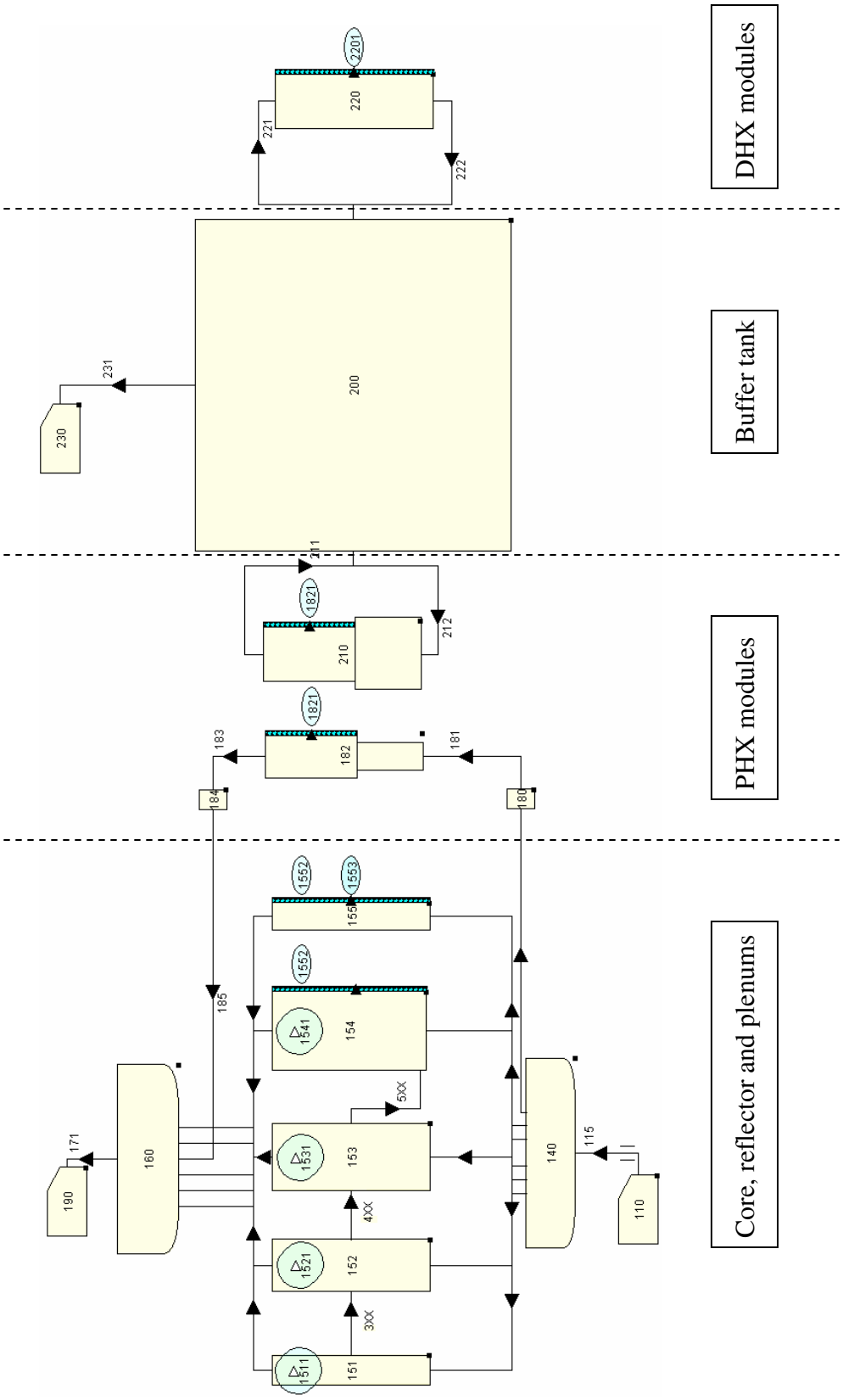

Figure 5-1: Overview of the RELAP5-3D model of the PB-AHTR. Hydrodynamic volumes are light orange, the heat structures blue green

on one elementary volume V between the junction j and j+1 with area $A_{j/j+1}$, yielding for example:

$$V\frac{\partial\overline{\rho X}_V}{\partial t}+\left(A\rho UX\right)_{j+1}-\left(A\rho UX\right)_j=V\overline{S}_v$$

where X any conserved field variable, and S is a source term.

The time derivative is then approximated using a given time step dt between times t_n and t_{n+1}. To obtain a closed set of equations for the discretized spatial mesh and time steps, the other terms, like the sources or the advective terms, can be evaluated at either time t_n (explicit evaluation), or t_{n+1} (implicit evaluation), or thorough a more complex combination (semi-implicit).

Explicit evaluation permits faster evaluation, but can induce instabilities in the numerical solutions, whereas implicit yields more complex linear systems to solve, but is more robust. RELAP5-3D gives the user several solver options to choose between more implicit or more explicit methods.

For this study a semi-implicit scheme was selected with an implicit coupling of the heat structures, where phenomena with shorter time steps are analyzed implicitly. According to the RELAP5-3D manual volume I, this is the most commonly recommended approach for any transient calculations.

The hydrodynamic components correspond either to the primary system (their numbers are generally in the form 1XX), or the buffer salt (their numbers are in the form 2XX).

a. Pebble bed core

In order to reproduce more accurately the non-uniform heat generation in the pebble bed core, and to take into account any possible three-dimensional flow, the core was divided into four concentric annular zones, with respective outer radii 0.85 m, 1.7 m, 2.55 m and 3.4 m. The corresponding RELAP components are 151, 152, 153 and 154. Each of these components is divided into 12 axial volumes of uniform height 0.533 m. This model can represent axisymmetric primary flow in the core.

RELAP would normally use standard pipe pressure loss correlations in these components. These settings are replaced by an implementation of the Ergun correlation discussed in Chapter 2. Between two volumes of the core, the friction pressure loss is computed using:

$$\Delta p_{fric}=K_e\frac{\rho v_{junc}^2}{2}$$

where v_{junc} is the junction flow velocity and K_e is given by Ergun correlation Eq. (2.10):

$$K_e=2\frac{L}{d_p}\left(\frac{1-\varepsilon}{\varepsilon^3}\left(180\frac{1-\varepsilon}{\mathrm{Re}_d}+1.8\right)\right)$$

In Fig. 5-1, the axial junctions in the core components 151-154 are not shown, while the radial cross flows are numbered 3XX, 4XX and 5XX with XX varying from 1 to 12.

The core model also includes a radial reflector represented by component 155. The reflector has a 0.106-m^2 flow area and 1-cm hydraulic diameter. This can either represent a 0.5-cm gap in the reflector where primary coolant can flow, or 1-cm vertical cooling channels. This component is also divided into 12 axial volumes.

The lower and upper plenums are modeled using two branch components. Each of them includes a single volume of primary coolant connected to the four parts of the core, the reflector, the PHX modules and the boundary components. They are labeled 140 and 160 respectively.

b. PHX modules

In the primary side, the PHX loop is composed of two parts: one corresponds to the 16 inlet and 16 outlet manifold pipes connecting the PHX inlet/outlet plenums and the PHX modules, and the PHX modules themselves which have a total of 4000 tubes.

The manifold pipes are represented by components 180, 184 and the lower half of 182 All these manifold pipe components have a 10-cm hydraulic diameter and a combined 0.126 m^2 total flow area. To accommodate the proper height and radial position of the connection to the bottom inlet plenum, the elementary volume size over one pipe total length is either 0.167 m or 0.533 m: the nodalization is the same for all pipes. The total length of a pair of inlet and outlet manifold pipes adds up to 4.2 m.

The 4000 tubes are represented by the upper half of component 182, which is characterized by a hydraulic diameter of 2.5 cm and a total flow area of 1.96 m^2. Its total length of 3.2 m is divided in 0.533 m nodalization volumes. In component 182, it is straightforward to modify the repartition between the connecting manifold pipes and the PHX tubes, so that parametric studies of the effect of the PHX tube length are simple to undertake.

The junction 181 between components 180 and 182 includes a fluidic diode model, which consists in a junction flow resistance of K = 1 downflow, K = 400 upflow. The corresponding area for this resistance is the total flow area of the manifold pipes (0.126 m^2).

The buffer side of the PHX is represented by component 210. The upper half represents the combined flow inside the tube bundles of the 8 PHX modules, and the lower half the baffle around each PHX module.

The external flow through the square-pitched array of tubes in the PHX modules is characterized by a hydraulic diameter of 3.74 cm, a combined flow area of 2.94 m^2 and a 3.2 m total length divided into 0.533 m elementary volumes.

The baffles have an 88-cm diameter, 4.9-m^2 flow area, a total length of 3.2 m, and 0.533-m long elementary volumes.

c. Buffer salt pool

The buffer salt pool is modeled by component 200, which has a uniform total area of 111.2 m^2 and a height of 12.8 m. It is uniformly divided into elementary volumes with a height of 1.067 m.

The DHX modules have almost exactly the same design as the PHX modules, except that the heat exchangers are 6.4 m tall, so there are no sections of the DHX baffles that do not have tubes inside.

d. Boundary conditions

As shown in Fig. 5-1, the primary system does not include the 4 primary loops with the primary pumps and intermediate heat exchangers (IHX). However, inlet and outlet flow boundary conditions are applied on the inlet and the outlet plenums and emulate the effects of this loop for steady state operations (where cool flibe is provided to the inlet plenum, and an equal flow rate of flibe removed from the outlet plenum) and loss of forced cooling transients (where the IHX primary loop flow is set to zero, reflecting the lack of buoyancy driven flow when no heat is removed from the IHX modules). This approach cannot treat transients where the primary pumps remain totally or partially operating, but is sufficient for the LOFC and ATWS transients studied here.

During steady state operation, components 110 and 115 inject a 9600 kg/s flow of flibe coolant at 600ºC in the lower plenum. Component 190 is an outflow component and plays the role of a constant pressure boundary condition at 1 bar on top of the upper plenum. This component discharges the heated 9600 kg/s flow that comes from the outlet plenum.

After a trip of all the primary pumps, two flow paths exist for the primary coolant: the natural circulation loop provided by the PHX system, and the loop created by the IHX modules. This LOFC transient can then be modeled by decreasing the flow rate injected by component 115 to 0 kg/s, thus neglecting any flow in the IHX system. A ten-second linear coast down from 9600 kg/s to 0 kg/s was chosen to model the primary pumps trip.

2) Heat structures description

RELAP5-3D heat structures can have rectangular, cylindrical or spherical geometry. In this 1D description, the heat structure is composed by several layers of material, to accurately resolve transient conduction into the structures. Two boundary conditions are available for connections between any hydrodynamic component and heat structure. One option is to use a standard embedded correlation in RELAP to calculate the heat transfer coefficient; or where a standard embedded correlation is not available, the heat transfer coefficient can be entered as a tabular function of time.

To solve the one-dimensional heat conduction equation, RELAP5-3D uses a Crank-Nicholson scheme, which does not impose any stability condition on the time step size and the heat structure mesh size, and gives a good level of truncation precision. The

heat transfer is advanced with the same time step as the hydraulic calculation using this approach.

The heat structures were numbered according to the hydraulic components they are attached to.

a. Pebble bed core

A single pebble is modeled as a spherical structure with the nodalization shown in Table 5-1, depending on its geometry.

Homogeneous pebble	Graphite kernel	Fuel zone	Coating
Thickness	0 cm	2.5 cm	0.5 cm
# intervals	0	8	4

Annular pebble	Graphite kernel	Fuel zone	Coating
Thickness	1.98 cm	0.52 cm	0.5 cm
# intervals	5	5	2

Table 5-1: Radial nodalization of the homogeneous and the annular pebbles

Each of the 4*12 = 48 hydraulic zones in the core is connected to the number of pebbles necessary to fill its volume to reach the desired porosity ε, which creates the heat structures 1151, 1152, 1153 and 1154. The surface area of a pebble is multiplied by the number of pebbles in the volume to give the appropriate heat transfer surface between the pebble bed and the given hydraulic volume.

As described in Table 2-2 of chapter 2, the heat transfer coefficient used for the boundary conditions between the fluid and the pebbles is given as a tabulated function of time according to the correlation, Eq. (2.12), with the value calculated based on the operation regime and flow rate in the reactor.

b. PHX modules

The metallic structure of the PHX modules is reproduced using a cylindrical pipe structure 1182 with a total thickness of 2.5 mm, divided into 3 radial intervals, connecting the primary hydraulic component 182 and the buffer hydraulic component 210.

On the both primary and buffer salt sides, the standard embedded RELAP5-3D pipe heat transfer correlations were used, with the limitations discussed in chapter 2, sections A.3 and B.2.

c. DHX modules

The DHX module structure uses the same discretization than the PHX discussed above, and is numbered 2201.

Because the design of the DHX has not been fully completed yet, it not possible to give a precise description of the boundary conditions in this structure. Because its design goal to remove 48 MW with a temperature difference of 100ºC, a uniform heat transfer coefficient was fixed on the buffer side, while the other side of the DHX was fixed at the constant sink temperature 500ºC. As the buffer salt temperature changes very slowly through the transients studied, this approximation was judged to predict the buffer salt temperature evolution with sufficient accuracy.

3) Heat source description

a. Heat source distribution

The heat source distribution was determined using radial and axial power peaking factors described in Annex A. The nominal thermal power of the reactor was fixed at 2400 MW_t, which represent an electrical power of 1100 MW_e with a power conversion efficiency of 46%.

This power map was integrated over each of the 48 elementary core elements to assign each the correct power level.

b. Decay heat curve

For simple LOFC transient, the transient decay power level was taken from previous calculations from studies on the NGNP prismatic core [4]. Annex A provides this decay heat curve.

For LOFC, the scram is initiated 3 seconds after the pump trip: during this short time, the core remains at full power. No reactivity feedback model has been implemented during this 3 sec. period.

c. Point kinetics model

For the RELAP modeling of ATWS transients, the feedback map presented in Table 4-3 of chapter 4 has been adopted as a baseline value. The reactivity feedback coefficients were also treated as an adjustable parameter, using a range of values that are consistent with those calculated in MCNP, and with the more negative coefficients that have been found with recent optimized core designs.

The reactivity changes due to temperature contribute in the variations of power through the classical point kinetics equations (PKE) [1]:

$$\frac{dn(t)}{dt} = \frac{\rho(T) - \beta}{\Lambda} n(t) + \sum_i \lambda_i C_i(t)$$

$$\frac{dC_i(t)}{dt} = \frac{\beta f_i}{\Lambda} n(t) - \lambda_i C_i(t)$$

where n(t) is the neutron density and $C_i(t)$ the delayed neutron precursors density. From n(t) the total fission power of the reactor can be determined. The decay heat is calculated

using the ANS79-1 standard, which uses ^{235}U as the only source of fission fragments. By default, RELAP5-3D considers equilibrium quantities of fission fragment obtained after an infinite reaction operation time. The RELAP5-3D decay heat curve is about 33% higher than the NGNP decay heat curve presented in Annex A, so the RELAP5-3D curve is used for conservatism here.

RELAP5-3D has two ways to represent the reactivity changes versus temperature

– A separable model, where the coolant and fuel temperatures feedbacks are independent:

$$\rho = \rho_0 + \alpha_{fuel}\overline{T_{fuel}} + \alpha_{cool}\overline{T_{cool}}$$

– A more general model, where the two temperatures feedbacks can have effects on each others:

$$\rho = F(\overline{T_{fuel}}, \overline{T_{cool}})$$

The reactivity is linearly interpolated between the different temperatures data points given in the input. Caution is required to assure that the feedback coefficients cover the full range of temperatures that the fuel and coolant reach.

The point kinetics differential equation (PKE) has typically a small characteristic time compared to the TH phenomena ($\Lambda/\beta = 5\times10^{-4}$ sec$/0.0065 = 0.08$ sec compared to a few seconds to many minutes). Thus, the advancement time step of the kinetics equation should be smaller than the advancement step for the TH calculations. RELAP5 uses a modified Runge-Kutta method to solve the system of linear ODE corresponding to the PKE's:

$$\frac{dX(t)}{dt} = AX(t) + B$$

where A and B are held constant over the TH advancement time step. The time step used to solve this equation is checked and if necessary refined by using tight convergence criteria on the power P(t).

This model does not take into account any three dimensional effects of the core temperature distribution into the neutronics calculation, as the temperatures used to compute the feedback are averaged over the whole core. Further studies may be necessary to assess the sensitivity of the ATWS response to this point kinetics assumption, for instance using a coupling of RELAP with a 3-D neutronics code such as PARCS. This would require more detailed calculations of effective macroscopic cross sections in function of temperature in the PB-AHTR core.

4) Time step control, precision studies

RELAP5-3D uses an adaptative time step strategy to strike a compromise between calculation speed which requires large time steps, and stability of the hydraulics semi-implicit scheme which requires small ones.

The assessment of stability uses the Courant limit time steps, calculated in every hydraulic volume:

$$\Delta t_i^c = \frac{\Delta x_i}{U_i}$$

The Courant-Friedrichs-Lewy stability condition for a purely explicit scheme for the advection equation imposes that the discretization time step satisfies the requirement that $\Delta t < \min_i(\Delta t_i^c)$. However, because RELAP5-3D uses a semi implicit scheme, it is possible to relax this condition and violate the Courant limit in some hydro volumes. More precisely, the code chooses the time step so that:

$\Delta t > \Delta t_i^c$ for 1/5 of the volumes with lower Courant limits

$\Delta t \leq \Delta t_i^c$ for 4/5 of the volumes with higher Courant limits

It is possible to manually impose a smaller step by inputting a maximum time step.

To verify the adequacy of the current nodalization, a model of the AHTR with a finer spatial mesh was built and run. All the elementary volumes of the system were divided in half, so that the spatial mesh sizes were divided by two. In the core, the four radial zones were conserved, and only the axial subdivisions were refined. The meshing for the heat structure was not modified.

An ATWS transient with the baseline design and reactivity coefficients (with annular pebbles) was run with the initial and the refined mesh. The differences between the two models were benchmarked by comparing the predicted core outlet temperature and the mass flow rate into the PHX (Figs. 5-2 and 5-3).

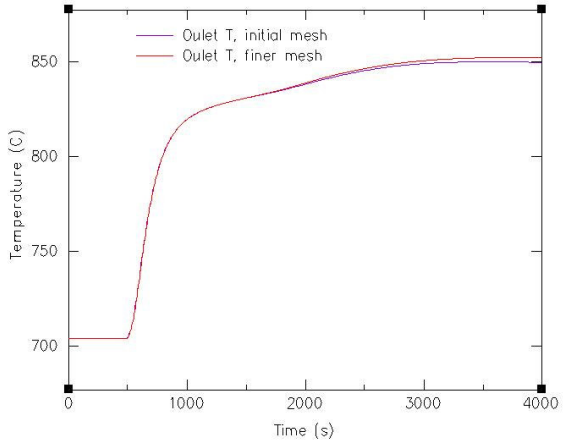

Figure 5-2: Outlet temperature for the initial and finer nodalization

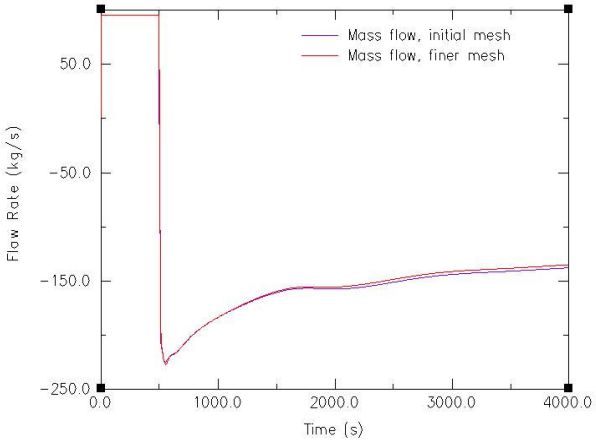

Figure 5-3: PHX mass flow for the initial and the finer nodalization

The graphs show only very small differences between the two models, with outlet T difference at a maximum of 2ºC (corresponding to ~1 % of the temperature increase in the transient), and mass flow difference at a maximum of 3 kg/s (around 2 % of the maximum flow rate) .

Given these small differences, the coarser nodalization was adopted and used for the analysis presented here, as it provides faster calculation. Indeed, a doubling of the mesh nodes causes the number of elementary calculation steps to increase by a factor of approximately four, because the time step also needs to be divided approximately in half to meet a matching set of Courant conditions. A 10,000 s (reactor time) simulation is done in around 5 minutes (CPU time) with the coarse mesh, whereas the finer mesh model took around 25 minutes, on an Intel Centrino Duo processor (2000 MHz CPU frequency)

B. Steady state operation

The baseline steady state solution was obtained by letting the system converge to a steady-state condition with a fixed core flow rate of 9600 kg/s, with homogeneous fuel pebbles. Given that the residency time of the fluid in the buffer tank is approximately 20,000 s, the simulation was run for around 40,000 seconds to achieve a converged solution.

The results of the following section were obtained for homogeneous pebbles.

1) Flow distribution

The following mass flow rate distribution has been obtained in the primary loop:

- Active core region 9197.7 kg/s
- Bypass in reflector 306.8 kg/s
- Bypass in PHX: 95.5 kg/s

The flow is quite uniform in all the four radial core zones, so that the horizontal cross flows are negligible compared to the vertical forced flow. This design with a high-performance PHX vortex diode gives a total bypass flow rate through the PHX heat exchanger of around 5%.

The pressure loss from the inlet to the outlet of the core is 0.63 bar under forced flow, which is comparable to the analytical value predicted using the Ergun relation with a uniform temperature of 655ºC and a flow rate of 9200 kg/s (0.61 bar by hand calculation).

2) Temperature distribution

Figure 5-4 shows the axial core temperature distribution in the centerline core zone. Because the power distribution is roughly cosine shaped in the axial direction, the coolant temperature shows a typical sine shape resulting from the integration of the linear power along the direction of flow. The pebble surface and center temperature are also skewed toward the top of the core, as the temperature differences remain symmetric along the vertical direction, but the coolant temperature rises with the elevation.

The maximum flibe temperature at the top of the active core (~755ºC) is higher than the outlet temperature, as the outlet mixes coolant coming from cooler regions of the core and bypass flow at 600ºC. This gives a steady state T_{out} = 704ºC corresponding to T_{in} = 600ºC. This points to the importance of designing the outlet plenum to provide good mixing of the outlet flow and confirming in the future that this mixing occurs using more detailed 3-D simulations and experiments, so that the hot legs and primary pumps to not experience fluctuating temperatures.

The maximum temperature in pebbles for this homogeneous pebbles core design is 1015ºC.

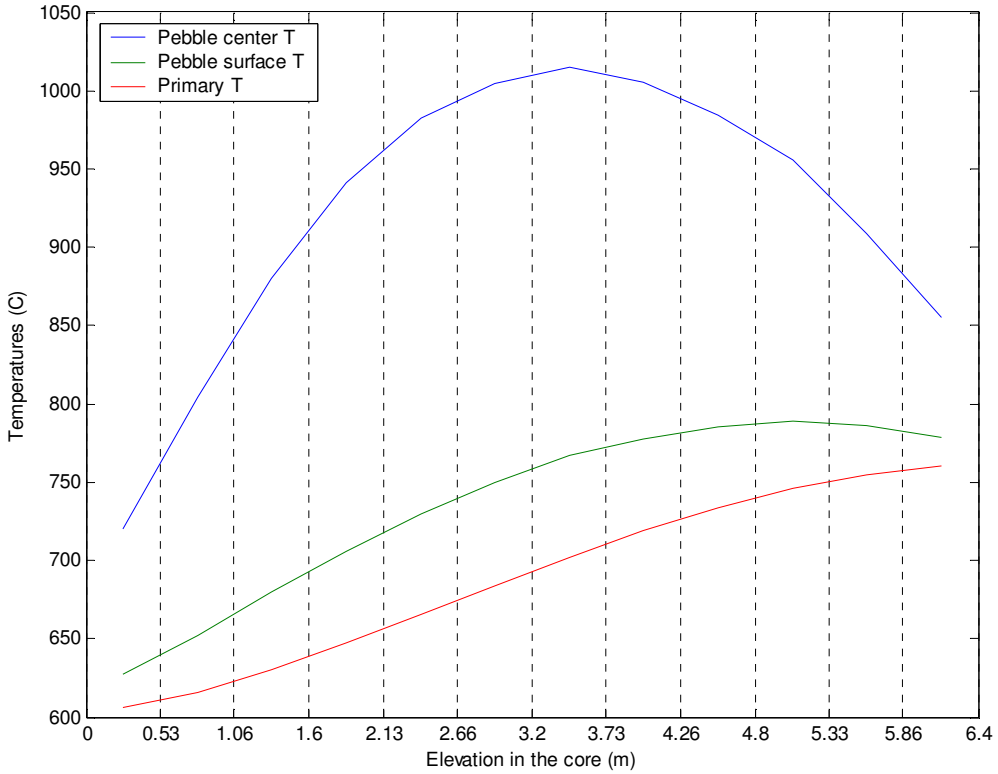

Figure 5-4: Axial core temperature distribution in the center core zone, for homogeneous pebbles. The plot shows the data for the 12 uniform axial cells limited by the dashed lines

These values can also be reproduced using a simple analytical model. The expected total flow in the core is around 9200 kg/s, corresponding to the following Reynolds number:

$$\mathrm{Re} = \frac{\dot{m} d}{\mu A} = 2300$$

taking the viscosity of flibe at 655ºC, for which $\mathrm{Pr} = 14.3$. According to the correlation, Eq. (2.12) adopted in chapter 2, we have the following Nusselt number for forced convection inside the bed:

$$\mathrm{Nu} = 2 + 1.1\ \mathrm{Pr}^{1/3}\ \mathrm{Re}^{0.6} = 280$$

The following heat balance between heat generated locally and heat transferred can be made at the surface of the pebble:

$$\Delta T_{surf}\ \frac{Nu\,k}{d}\frac{6}{d} = \frac{q'''_{loc}}{1-\varepsilon} \quad \text{and} \quad \Delta T_{surf} = \frac{q'''_{loc}}{6Nu\,k(1-\varepsilon)}d^2$$

where the heat source is per cubic meter of core volume.

Solving the spherically-symmetric heat diffusion equation yields the following temperature drop across the graphite pebble outer coating, and across the fuel zone:

$$\Delta T_{coat} = \frac{q'''_{loc}}{6k_g(1-\varepsilon)} d^3 \left[\frac{2}{d_{in}} - \frac{2}{d} \right]$$

$$\Delta T_{fuel} = \frac{q'''_{loc}}{6k_g(1-\varepsilon)} \left(\frac{d_{in}}{2} \right)^2$$

This yields the following values, for at hypothetical pebble bed with homogenous pebbles immersed in a Re = 9200 kg/s flow of 655ºC flibe, with a uniform heat generation rate of 10.3 MW_t/m^3 shown in Table 5-2.

ΔT_{surf}	ΔT_{coat}	ΔT_{fuel}
33.5 ºC	137.7 ºC	59.8 ºC

Table 5-2: Predicted temperature differences in the homogeneous pebble, according to a simple analytical model

Compared to this idealized model, the temperature and power density in the core are not uniform. In high power, high temperature regions, the coolant viscosity is lower, which increases Re and the heat transfer coefficient. This means that while the temperatures drop inside the pebbles increases in regions with higher q'''_{loc}, the temperature drop at the surface of the pebble may remain more stable, because Nu also increases.

The values found by this simple analytical model match the RELAP steady state simulations closely, and as predicted there is a larger temperature drop from the center to the surface of the pebble than the temperature drop from the surface to the coolant.

Because the coolant heat transfer coefficient is likely underestimated because mixed convection effects are neglected, the actual temperature drop from the surface of the pebble to the coolant is likely even smaller. This is fortuitous, because it suggests that the stored energy in the pebbles, which is important in affecting the rise in the core outlet temperature that occurs during the early fuel equilibration phase, depends primarily on conduction in the pebble and can be predicted accurately.

C. Loss of Forced Cooling (with scram)

1) Flow distribution

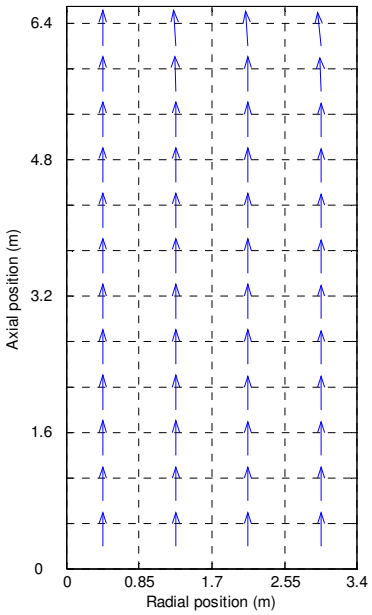

Fig. 5-5: Steady state velocity distribution (max velocity: 0.34 m/s)

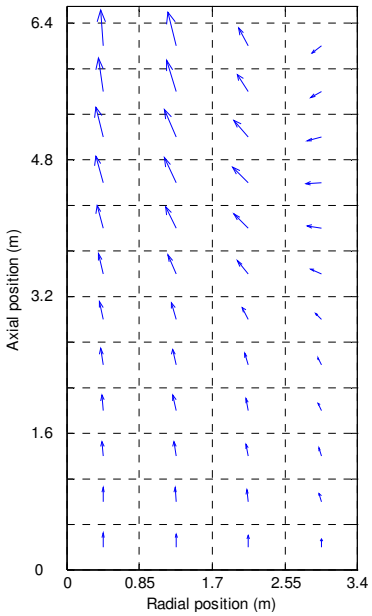

Fig. 5-6: Distribution 500s after trip (max velocity: 0.019 m/s)

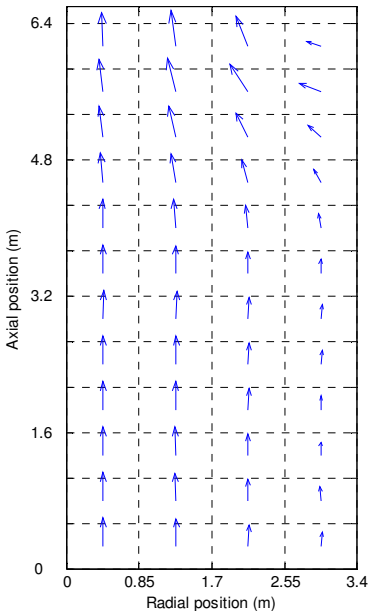

Fig. 5-7: Distribution 1500s after trip (max velocity: 0.009 m/s)

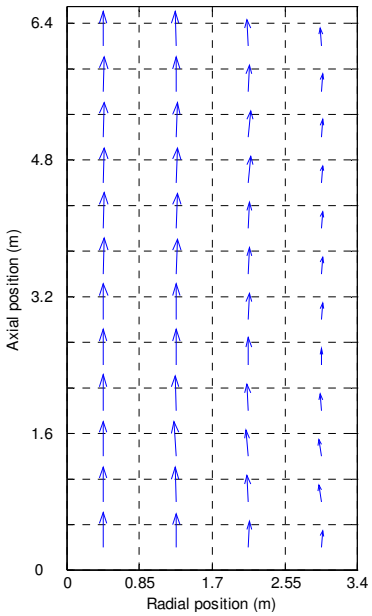

Fig. 5-8: Distribution 3500s after trip (max velocity: 0.006 m/s)

Figures 5-5, 5-6, 5-7 and 5-8 present the flow pattern into the pebble bed at several times during a LOFC transient for the baseline PHX design, with homogeneous pebbles. The cell liquid velocities have been normalized to the maximum velocity in the core at each specific times, so that the top left vector has the same length in all four figures.

At steady state (Fig. 5-5), the flow in the core flow is driven by the coolant injection at 9600 kg/s and is very uniform. On the other hand, during the LOFC transient, the flow is not uniformly distributed either in the radial or in the axial direction. It shows a recirculation pattern at the beginning of the transient (500 sec after pump trip, Fig. 5-6), where flow reversal can be observed in the top outer region of the core.

The pattern observed in the transient can be explained by the natural circulation effect inside the core, due to the radial temperature difference between the more heated inner regions and the less heated outer region of the core. Later during the transient, the decay heat generation decreases exponentially and convection transports heat radially outward, this temperature difference become smaller and this natural circulation pattern slowly disappears. However, the outer core is still colder than the center, which means that the mass flows driven by natural circulation with the PHX modules will be greater in the center part of the core. This explains the larger velocities near the center.

As for the rest of the primary system, the bypass flow in the reflector decreases to nearly zero, whereas the flow rate in the PHX evolves as shown Fig. 5-9. There is a flow reversal from positive values (upward bypass flow) to negative during the transient (downward flow). As expected, the PHX flow occurs as a consequence of the natural circulation loop created with the hotter core.

These transient flow patterns are not strongly affected by the type of pebbles (annular or homogeneous)

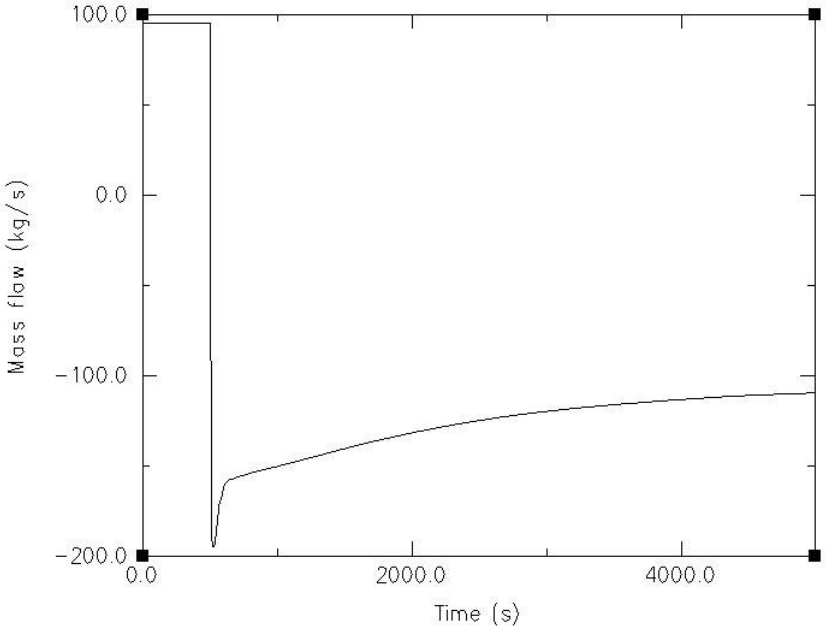

Figure 5-9: Mass flow in the PHX during an LOFC transient, for the homogeneous pebbles

2) Temperature variations

The inlet plenum temperature, outlet plenum temperature, average temperature of the flibe in the core and maximum fuel temperature have been plotted for the homogeneous and the annular pebbles in Figs. 5-10 and 5-11, respectively. The two phases of the LOFC transient can be seen, the early fuel equilibration phase and the subsequent long-term heat removal phase.

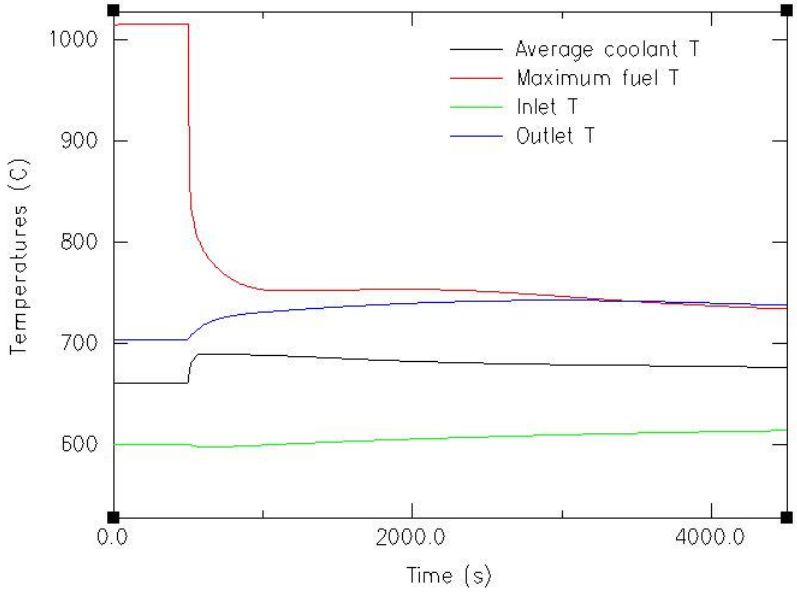

Figure 5-10: Temperatures variation during the LOFC transient, baseline PHX and homogeneous pebbles

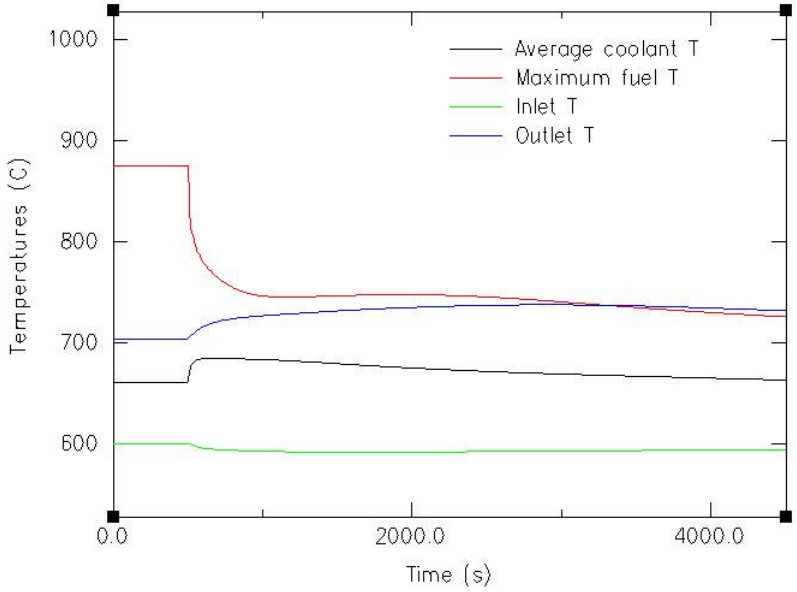

Figure 5-11: Temperatures variation during the LOFC transient, baseline PHX and annular pebbles

The initial thermal equilibration phase occurs over a few hundred seconds, as the fuel stored energy is transferred to the coolant. As the heat flux from the pebbles drops to decay heat level, a convergence of the maximum fuel temperature and the coolant outlet temperature occurs. This can be explained by the fact that at decay heat levels, only a small temperature difference between the coolant and the pebble center is required to remove heat from the pebble. Subsequently, during the long-term heat removal phase all temperatures evolve very slowly due to the large thermal inertia of the PB-AHTR core and coolant.

For both designs, the rise in the core outlet temperature is very modest (from the initial 704ºC to a maximum of 743ºC for the homogeneous pebbles, and to 738ºC for the annular pebbles). This slightly lower value for the annular pebbles can be explained by the lower stored energy inside the annular pebble, as the steady state maximum pebble temperature is decreased from 1015ºC to 875ºC; the initial increase of the coolant temperature just after the trip (t > 500 s) to transfer this excess heat is then larger for the homogeneous pebbles.

3) PHX design optimization study

The total heat transfer in the PHX can be expressed as a function of the average temperature difference between the primary salt and the buffer salt in the PHX modules:

$$Q_{phx} = \left(\frac{d_{f,phx}}{Nu_{f,phx} k_f L_{phx} L^w_{f,phx}} + \frac{d_{b,phx}}{Nu_{f,phx} k_f L_{phx} L^w_{b,phx}}\right)^{-1} \overline{\Delta T}$$

Using the RELAP5-3D equation for natural convection, Eq. (2.6) (for which $Nu \propto Ra_d^{1/3} \propto d$), on the primary and the buffer sides of the PHX, the total heat transfer in the PHX can be expected to vary as (only taking into account geometric parameters appearing explicitly in the expression, and assuming the pitch to diameter ratio in the PHX is kept constant):

$$Q_{phx} \propto \frac{Ra_{d_{phx}}^{1/3} N_p H d_{phx}}{d_{phx}} \propto \frac{N_t H}{d_{phx}}$$

where N_t is the total number of PHX tubes in the modules and H its total height.

This equation shows that transient PHX performance depends primarily on the two parameters N_tH and d_{phx}. Having very low d_{phx} is not desirable from the perspective of mechanical strength. For this reason a value of d_{phx} = 2.5 cm was selected as a reasonable choice. The baseline design has N_t = 4000 and N_tH = 12800 m .

Figure 5-12 shows the influence of the parameter N_tH on the maximum core outlet temperature, for annular pebbles. As N_tH increases, the core outlet temperature monotonically approaches a value in the range of 735°C.

This insensitivity of the peak core outlet temperature is explained by the ~ 2000 s residency time of the coolant in the core. Before this time, the PHX design does not influence the core outlet temperature, and the corresponding temperature rise is dominated instead by the fuel stored energy and the early, higher rate of decay heat

generation. Figures 5-10 and 5-11 show that the maximum outlet temperature for the baseline case is attained around 2500 s after pump trip, and that most of the outlet T rise occurs between 500 seconds (pump trip) and 2500 seconds. This means that the baseline design is nearly optimal to decrease T_{out}, which is confirmed by Fig. 5-12.

This broad range of nearly optimal N_tH also means that the peak core outlet temperature in the LOFC transient is quite insensitive to both N_tH and to uncertainties on the heat transfer coefficients on the primary or the buffer side of the PHX, as it is formally equivalent to decrease the heat transfer coefficient of the PHX and decrease the N_tH of the PHX modules. Another way to explain this is that the maximum outlet temperature does not depend on details of the PHX design, as long as the modules have roughly the proper size to prevent overheating of the outlet coolant for times greater than some 2000 s after pump trip.

As explained in chapter 2 on correlations, the heat transfer coefficient used by RELAP5-3D on the primary side likely overestimates the actual heat transfer coefficient by a factor of around 2, and reproduces more accurately the heat transfer on the buffer salt side. As the primary and the buffer salt sides have roughly the same heat transfer coefficients, this means the total heat transfer coefficient should be overestimated by a factor of (2/3)/(1/2) = 4/3 in this model. We can offset this bias by looking at the PHX design for which N_tH = 3/4*12800 = 9,600 m. There is around a 5ºC difference on the outlet temperature between N_tH = 9,600 and N_tH = 12,800, as shown in Fig. 5-12.

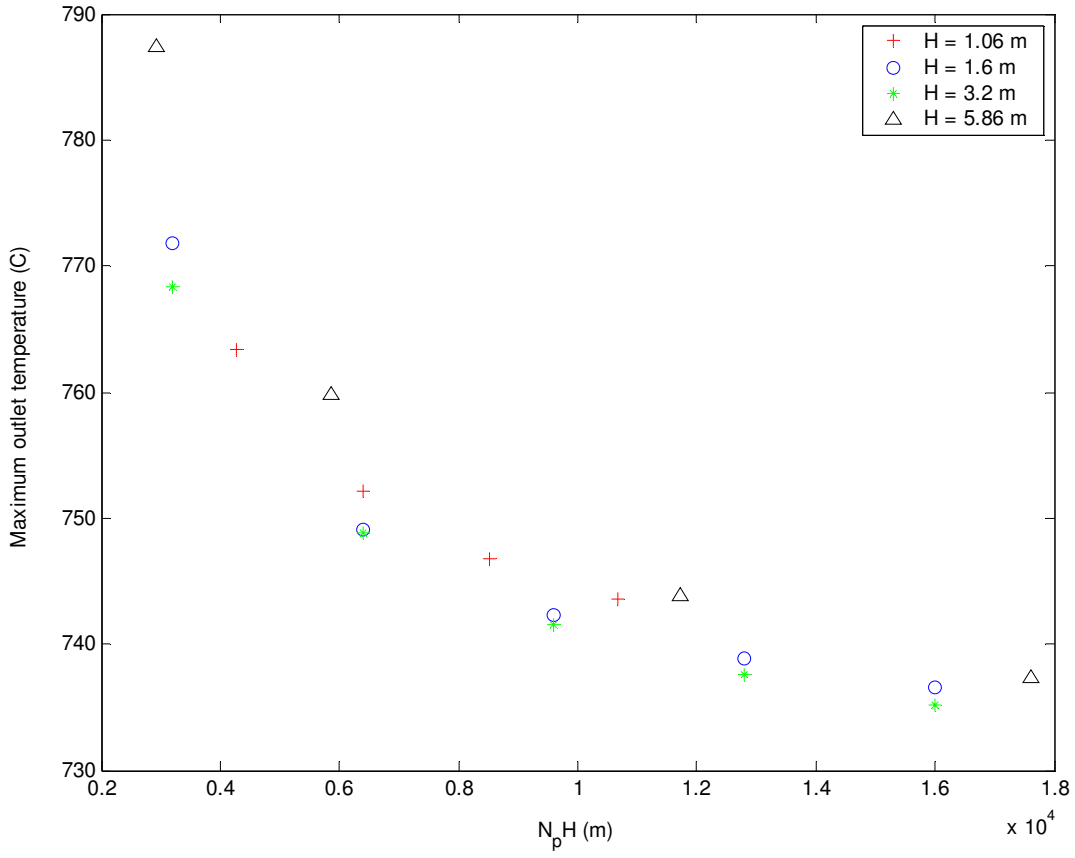

Figure 5-12: Maximum outlet temperature during LOFC for annular pebbles, as a function of N_pH,. The baseline PHX design has N_pH = 12,800 m and H = 3.2 m (green cross).

D. Anticipated Transient Without Scram (With LOFC)

1) Mass flow

In an anticipated transient without scram (ATWS) with LOFC, flow through the IHX's becomes very small due to their high flow resistance, and the primary salt flows in a natural circulation loop between the core and the PHX modules while the bypass flow in the reflector is negligible. Figure 5-13 shows the resulting PHX mass flow rates for the homogeneous and the annular pebble designs.

The PHX mass flow for the annular pebbles design is somewhat smaller in absolute value than the mass flow for the homogeneous pebbles. This is because the coolant temperatures are significantly smaller in the core for the annular pebbles, which decreases the coolant temperature difference between the core and the PHX that drives natural circulation.

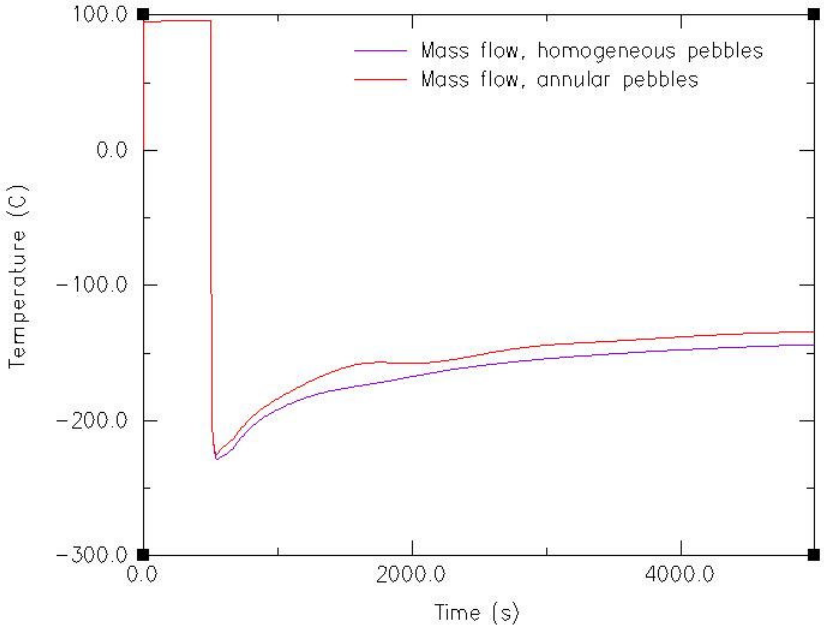

Figure 5-13: Mass flow in the PHX during an LOFC transient, baseline PHX design

2) Reactivity and power evolution

Figures 5-14 and 5-15 present the reactivity and power evolution, respectively, for the homogeneous and the annular pebble cores. Due to the temperature increase in the fuel, there is a reactivity insertion of up to -$0.28 for the homogeneous pebbles, and -$0.32 for annular pebbles approximately one hundred seconds after the trip. The difference in reactivities is explained by the lower average steady state temperature of the annular fuel (25ºC lower) which gives a potentially higher temperature difference between steady and transient temperature during the early fuel thermal equilibration phase of the ATWS.

During the first 1000 s of the transient, the annular pebble reactivities are always lower than for the homogeneous pebbles. Just after 1000 s of transient (t = 1500 s), for the annular design there is a significant positive reactivity insertion up to +$0.05: this corresponds to the period where the cooled flibe from the PHX fills the volume of the lower plenum and begins to fill the bottom of the core, thus driving the reactivity up.

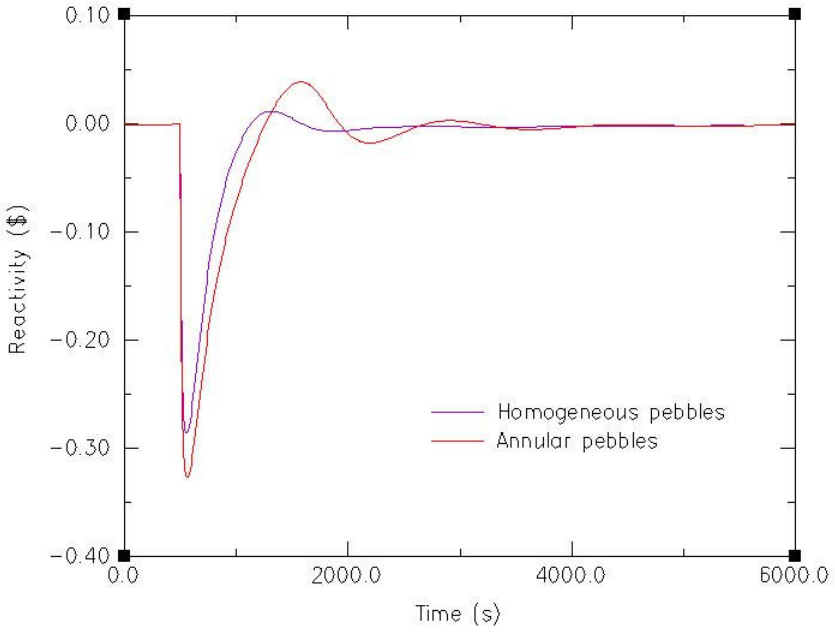

Figure 5-14: Reactivity insertion due to temperature variation in the core, baseline design

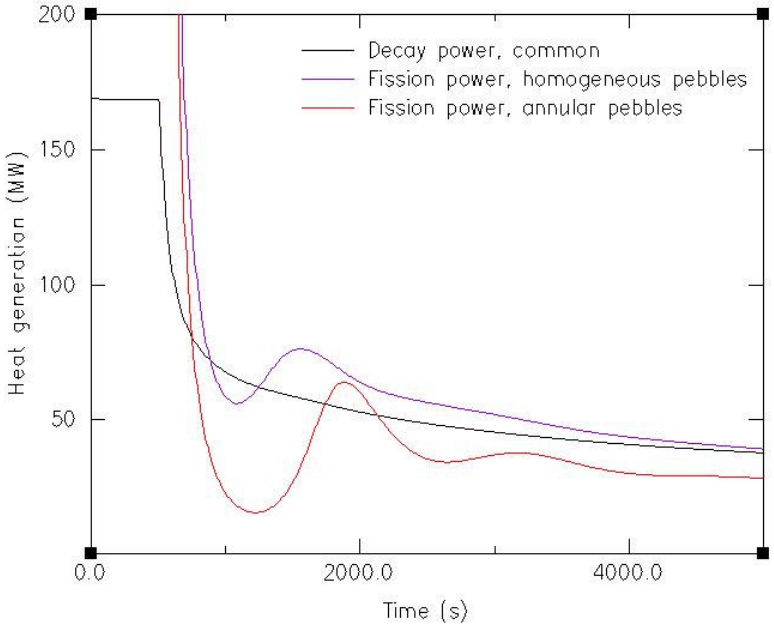

Figure 5-15: Decay and fission powers during ATWS, for the baseline design. The decay power does not differ significantly between the two pebble designs, therefore only one curve is shown

The fission power is obtained by integrating the point kinetics equations with this reactivity history. Because of consistently more negative reactivity (except during the

recriticality phase), the fission power during ATWS is always significantly lower for the annular pebble core than the homogeneous pebble core, by a margin of up to 40 MW. The homogeneous pebbles fission power is nearly always above the decay power in Fig. 5-15, whereas the annular pebbles fission power becomes smaller than decay heat after 300 s of transient, except during the short positive reactivity insertion.

3) Temperature evolution

As for the LOFC transient, various representative temperatures in the ATWS have been plotted Figs. 5-16 and 5-17 for the homogeneous and the annular pebble designs.

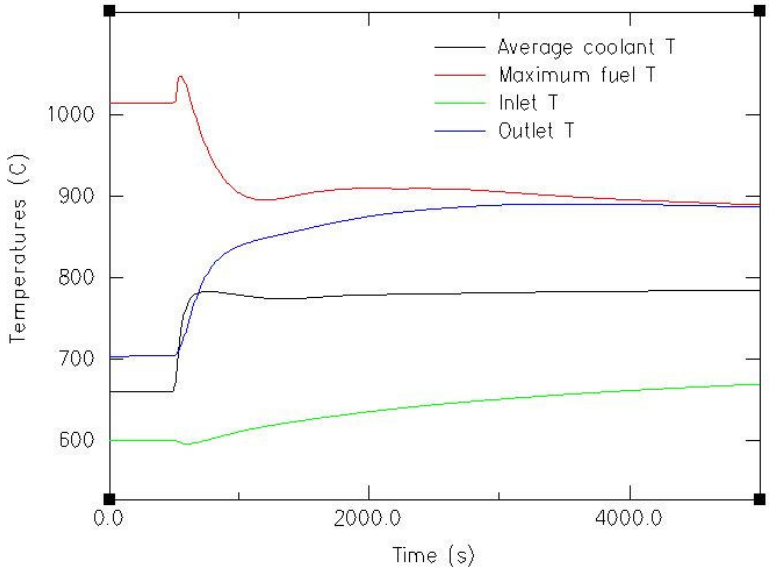

Figure 5-16: Temperatures variation during the ATWS transient, homogeneous pebbles

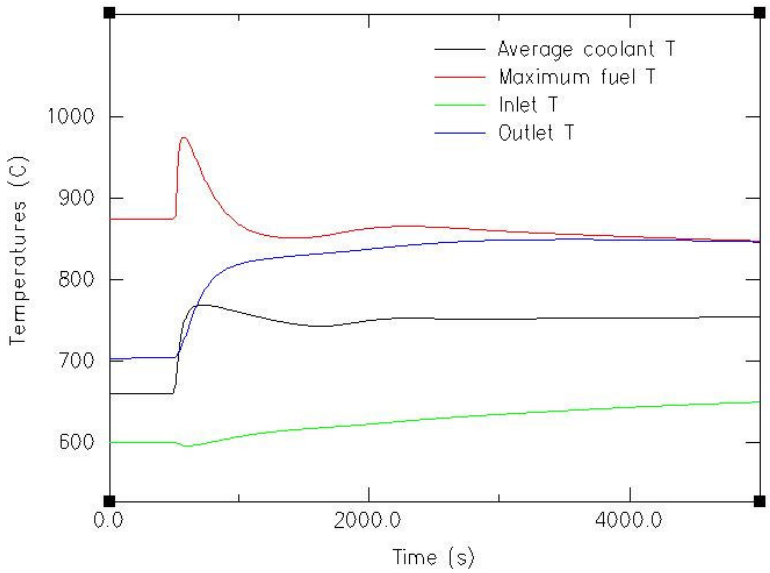

Figure 5-17: Temperatures variation during the ATWS transient, annular pebbles

The maximum fuel temperature in the pebble bed is 1050ºC for the homogeneous pebbles and 975ºC for the annular pebbles: this is far below the temperature ranges where TRISO fuel particles can fail (T > 1600ºC).

The outlet temperature rise is much more severe in the ATWS accident than in the LOFC transient: up to 895ºC for the homogeneous design and up to 850ºC for the annular design. The much higher rise for the homogeneous pebbles is a consequence of additional fission power, as presented Fig. 5-15.

4) PHX design optimization study

As for the LOFC transient, Fig. 5-18 presents a study of the ATWS core outlet temperature variations with the size of the PHX. As for the LOFC study, variations of *H* have been made with the upper end of the PHX modules at a constant elevation, so that smaller PHX have a higher average elevation and larger buoyancy driving forces.

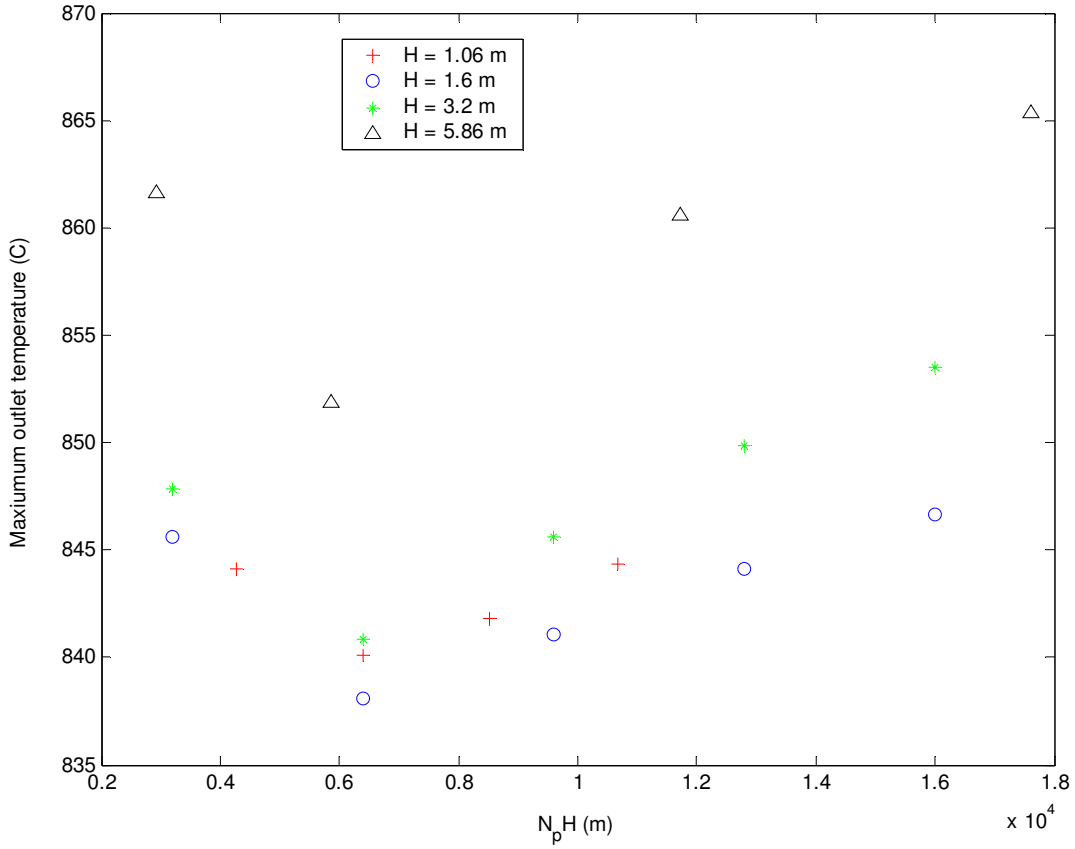

Figure 5-18: Maximum outlet temperature during ATWS, function of N_pH, for the annular pebbles. The baseline PHX design is represented by the green cross at N_pH = 12,800

For equal total PHX tube length, the shorter PHX with more tubes is more efficient than the taller PHX with fewer tubes. Figure 5-19 provides an explanation. The smaller PHX located at a higher average elevation provides a larger natural circulation flow, which explains the lower maximum outlet temperatures shown in Fig. 5-18. This

effect is particularly important when comparing the H = 5.86 m and the other design with H < 3.2 m: the difference of maximum outlet temperature is greater than 10ºC, whereas the designs with H < 3.2 m have values regrouped in a 5ºC interval.

At a given PHX height, there is an optimum value of the total PHX tube length (N_tH around 6000 m) to obtain the smallest maximum outlet temperature. This is because of the competition of two effects. Too small a PHX does not adequately remove the heat created during the ATWS transient. On the other hand, a bigger PHX cools down the flow in such a manner that the inlet temperature decreases significantly compared to smaller designs. The lower part of the core becomes filled with colder coolant supplied by the PHX after a time period comparable to the core residency time (~`2000 s). As the overall core temperature reactivity feedback is negative, the colder coolant drives up reactivity and recriticality is possible, as shown in Fig. 5-20.

These variations in the maximum outlet temperature are quite small, however, for a broad range of PHX sizes and heights. From Fig. 5-18, designs with H < 3.2 m and 4000 m < N_tH < 14,000 m have a maximum outlet temperature within a range of 10ºC. This means uncertainties on the PHX heat transfer correlations do not strongly impact this maximum temperature during the ATWS transient. For instance, the potential effect of uncertainty in the primary heat transfer coefficient can be emulated by comparing PHX designs with N_tH = 12,800 m (baseline) and N_tH = 9,600 m: the maximum is around 850ºC for the baseline parameters and around 845ºC for N_tH = 9,600 m.

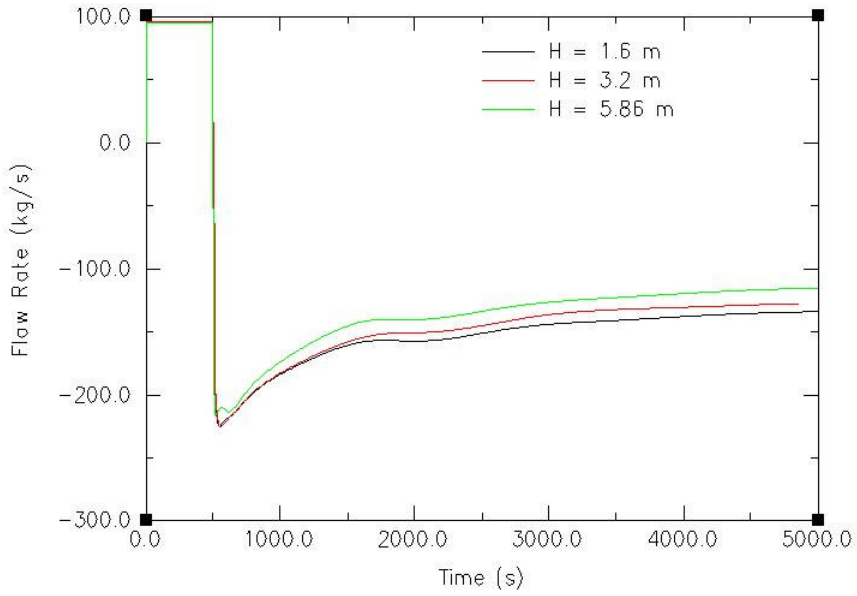

Figure 5-19: Natural circulation flow rate in the PHX during the ATWS transient, for various PHX height H. N_pH has been fixed to 12,800.

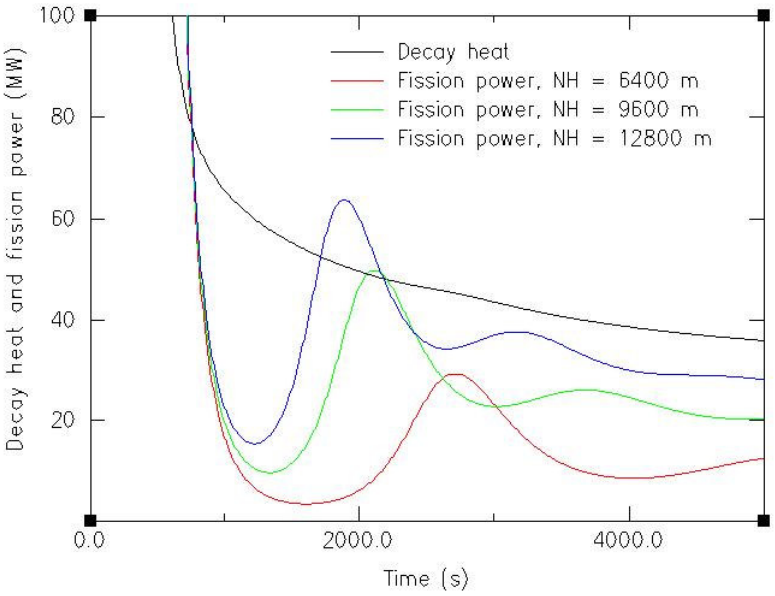

Figure 5-20: Decay heat and fission power levels during an ATWS transient, for various PHX sizes. H = 3.2 m is kept constant.

5) Feedback coefficient sensitivity analysis

In all these previous ATWS transient analysis, the feedback coefficients map provided in chapter 4, Table 4-3 were used. Over the relevant fuel and coolant temperature ranges, this baseline analysis resulted in the the following average values:

$$\alpha_c = +1 \text{ pcm/K}$$
$$\alpha_f = -5 \text{ pcm/K}$$

These reactivity coefficients are representative of a clean fuel at the beginning of life of the pebble, with a heavy metal loading of 10.3 g/pebble. Recent depletion analysis by Max Fratoni has shown that higher heavy metal loadings gives a negative coolant void coefficient, and results in higher discharge burnup, both of which are desirable properties.

As the precise fuel design is not yet completed and the fuel composition will change during operation, there are considerable uncertainties for these calculated coefficients. To investigate their impact on the peak core outlet temperatures reached in during an ATWS transient, a parametric study of the ATWS transient was undertaken, with the following range of values for the average feedback coefficient:

$$\alpha_c = -1, +0, +1 \text{ pcm/K}$$
$$\alpha_f = -10, -5, -3 \text{ pcm/K}$$

As a lower bound for the coolant feedback, $\alpha_c = +1$ pcm/K was chosen because results from Max Fratoni show that core designs with negative coolant void coefficients, which would give negative coolant temperature feedback, are feasible.

Tables 5-3 and 5-4 show the resulting variations of the peak outlet temperature and the maximum temperature in the pebbles attained during the ATWS transient. Peak outlet temperatures vary in the range 807ºC – 869ºC, and peak pebbles temperature in the range 920ºC – 1016ºC. Having more negative coolant and fuel coefficients generally result in lower peak temperatures. There are some slight differences with the previous baseline calculation, as the feedback coefficients map was replaced by average values: for instance, the maximum outlet decreases from 850ºC to 845ºC.

These maximum temperatures are more sensitive to variations of the coolant coefficients compared to the fuel coefficients: the 2 pcm/K difference in the coolant coefficient results in variation of the maximum outlet T up to 55ºC, whereas a 7 pcm/K variation in the fuel coefficient translates in a maximum outlet T variation of 39ºC. This behavior emphasizes the importance of obtaining a negative coolant feedback coefficient in minimizing the effects of ATWS transients, as it more effective to lower the outlet temperature than the negative fuel coefficient.

In one case, having a more negative fuel feedback does not result in a lower peak outlet temperature, when $\alpha_c = -1$ pcm/K and α_f varies from -5 pcm/K to -10 pcm/K. The explanation is provided by Fig. 5-21, which shows that the design with $\alpha_f = -10$ pcm/K undergoes a phase of recriticality earlier during the transient, due to the much more negative temperature feedback coefficients.

ºC	-1 pcm/K	0 pcm/K	**+1 pcm/K**
-3 pcm/K	816	831	869
-5 pcm/K	807	822	**845**
-10 pcm/K	811	820	830

Table 5-3: Maximum core coolant outlet temperature during the ATWS transient for various combinations of the coolant coefficient (columns) and fuel coefficient (rows). The baseline design value is shown in bold text.

ºC	-1 pcm/K	0 pcm/K	**+1 pcm/K**
-3 pcm/K	972	989	1016
-5 pcm/K	948	957	**970**
-10 pcm/K	920	924	929

Table 5-4: Maximum pebble temperature during the ATWS transient for various combinations of the coolant coefficient (columns) and fuel coefficient (rows). The baseline design value is shown in bold text.

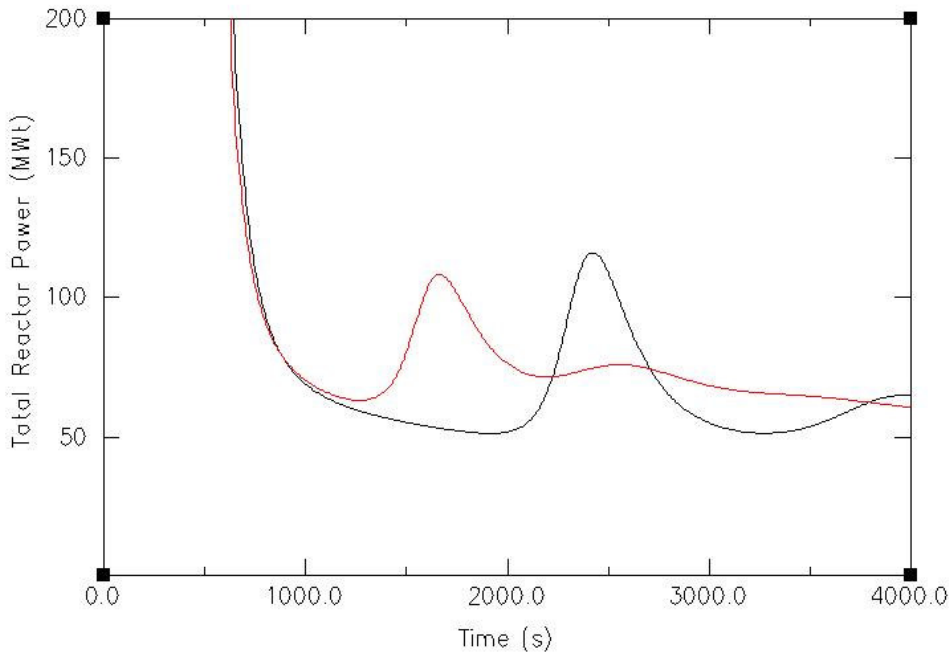

Figure 5-21: Total power during ATWS, for $\alpha_c = -1$ pcm/K , $\alpha_f = -5$ pcm/K (black curve) and $\alpha_c = -1$ pcm/K , $\alpha_f = -10$ pcm/K (red curve)

E. Study of a high outlet temperature variant of the PB-AHTR

The steady state and transient analysis of the baseline, low temperature PB-AHTR shows a modest rise of temperature for the LOFC transient and a larger but still reasonable rise during the ATWS, which preserves a significant safety margin. For the low-temperature PB-AHTR design, the potential exists to up rate the power of the reactor, or to increase the core outlet temperature.

Given this gentle behavior for the low-temperature design, it is interesting to first examine the potential for a higher temperature design, adapted to hydrogen production by thermo-chemical or high-temperature electrolysis processes. To increase the outlet temperature compared to the baseline design, the inlet temperature was set 50ºC higher (from 600ºC to 650ºC), and the steady state flow rate in the primary pump was halved (from 9600 kg/s to 4800 kg/s). The heat transfer coefficient in the pebble bed was decreased to reflect this lower mass flow rate (remembering that mixed convection effects likely result in a larger heat transfer coefficient). All the other parameters remain unchanged in the RELAP model: in particular, the annular pebbles design is adopted with the baseline temperature feedback, and the total steady state power is set at 2400 MW_t.

Neglecting the steady state bypass flows in the PHX and in the reflector, the core temperature rise is expected to approximately double to 200ºC during steady state operation: in fact, the calculated core outlet temperature is 859°C. This falls into the range of temperature that are compatible with hydrogen production by high temperature electrolysis or thermo-chemical processes.

1) Steady state operation

After running for 40,000 sec to approach steady state conditions, the following flow rates distribution was obtained:

- main flow through the active core 4592 kg/s
- bypass flow through the PHX 43 kg/s
- bypass flow through the reflector 165 kg/s

As for the low temperature design, the bypass flows only represents a negligible fraction of the flow through the active core.

With the changes from the baseline design, the outlet temperature increases to 859ºC, and corresponds to an outlet/inlet temperature rise of 209ºC. The peak fuel temperature rises to 1060ºC, which is well within the temperature limits of the TRISO fuel.

2) Loss of forced cooling with scram

Figure 5-22 shows the temperature histories during this transient, while Fig. 5-23 shows the natural circulation mass flow rate.

Compared to the low temperature design, the outlet temperature excursion during the LOFC transient is even smaller with a rise of 24ºC, to a peak value of 883ºC. Because of this small temperature rise, the natural circulation mass flow in the PHX is also somewhat smaller than in the standard low temperature design (flow rate at about 80 kg/s

instead of 100 kg/s previously). The reactor outlet temperature remains well within the ASME code temperature limit for Alloy 800H.

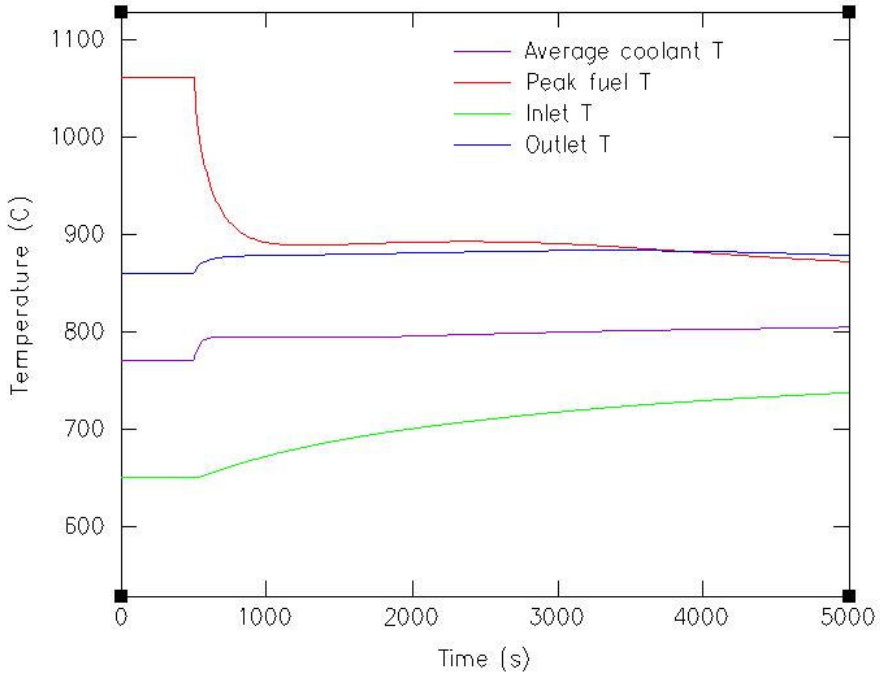

Figure 5-22: Temperatures during the LOFC transient, high T variant and annular pebbles

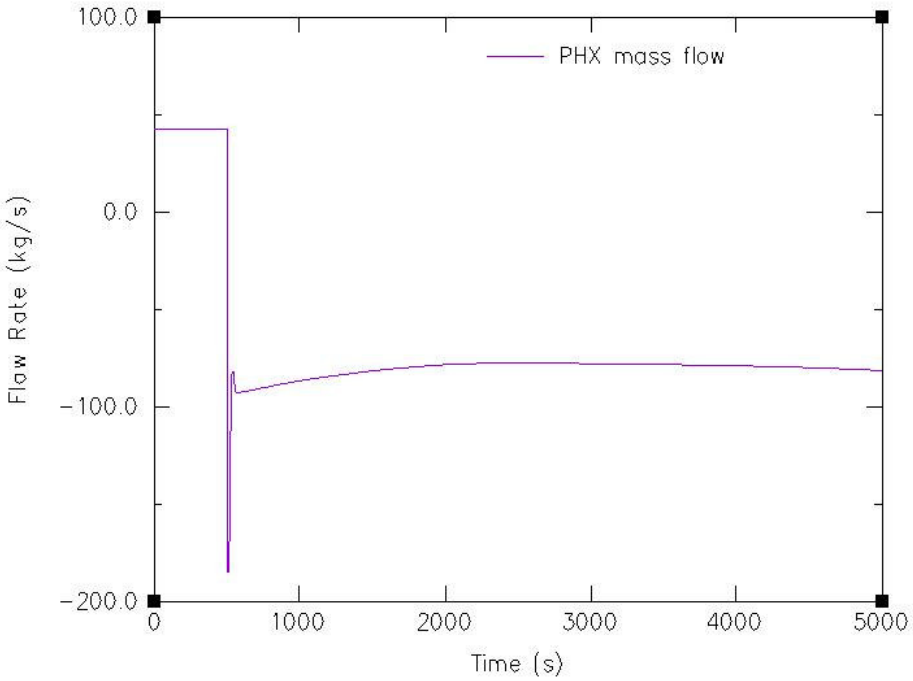

Figure 5-23: PHX mass flow during the LOFC transient, high T variant and annular pebbles

3) ATWS

The ATWS transient was also simulated for this high-temperature variant of the PB-AHTR design, and Fig. 5-24 shows the resulting temperatures histories. The RELAP5-3D simulation stopped at t = 2360 sec, due to a failure of the thermophysical library of the buffer salt, which has just reached a temperature of ~700ºC in one volume of the PHX buffer side. This failure is not due to any numerical artifact of the code: the temperature 700ºC corresponds to the physical limit of thermal dissociation temperature of sodium fluoroborate. This means that the selected buffer salt may not be adapted to this higher temperature design.

However, for the first 1500 s of the ATWS transient (t < 2000 s), the ATWS transient for this high T variant is milder than the equivalent transient for the standard low temperature design. During this 1500 sec period, the outlet temperature for the high temperature design rise is limited to 112ºC, compared to 134ºC for the low T design (the total rise during the transient being 145ºC). It is then possible to assume that the total temperature rise for the high temperature design is given (approximately) by:

$$T_{out}^{\max} = 112 + (145 - 134) = 123\ ^{\circ}\mathrm{C}$$

This translates into a peak outlet during the ATWS of around 982ºC for the high T design, which is just above the 980ºC ASME code specified limit for allow 800H. Further optimization could be investigated to lower this peak temperature: for instance, it is not obvious that the low temperature PHX design is well adapted to the high temperature PB-AHTR design variant.

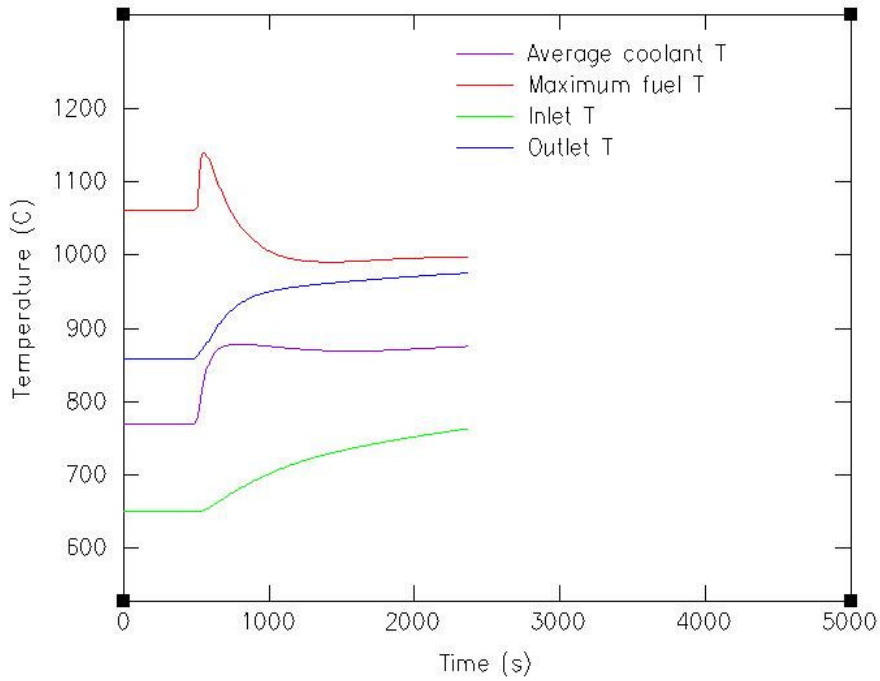

Figure 5-24: Temperatures during the ATWS transient, high T variant and annular pebbles

F. Study of power up rates for the baseline low-T PB-AHTR

Another path to exploit and further illustrate the relative gentle behavior of the low-temperature PB-AHTR is to investigate the effects of up rating the power of the annular-pebble baseline design, on the peak coolant outlet temperature and fuel temperature during LOFC and ATWS transients. If the core size can be kept constant and the total power is increased while remaining inside the temperature limits of the materials used for the high temperature components in the core outlet, this has the potential to reduce the capital cost.

This parametric study is done using RELAP5-3D by setting a higher steady state power in the input deck, and increasing proportionally the primary cooling flow rate in the IHX to match this higher heating power with the same ΔT_c. The number of emergency decay heat system PHX and DHX modules was raised proportionally to the up-rated power (from the initial 8 PHX/8 DHX modules). The following total power levels were studied parametrically:

- $P = 2400$ MW$_t$ and $\dot{m} = 9600$ kg/s (baseline design)
- $P = 3600$ MW$_t$ and $\dot{m} = 14400$ kg/s (+50% power up rate)
- $P = 4800$ MW$_t$ and $\dot{m} = 19200$ kg/s (+100% power up rate)

If we assume a power conversion efficiency of ~46%, the corresponding electric outputs are 1100 MW$_e$, 1650 MW$_e$ and 2200 MW$_e$ respectively.

1) Steady state operations

After attaining steady state conditions, the coolant temperature profile in the reactor remains virtually unchanged between the three sets of parameters. Indeed, the bypass flow outside the active core remain negligible in all three designs, which implies that the rise in reactor power is correctly balanced by the larger coolant flow in the active core region.

On the other hand, higher power results in higher temperature in the pebbles, which will have a significant impact in the transient behavior of the up-rated reactor. Table 5-5 shows the steady-state results.

	Active core flow rate (kg/s)	Outlet plenum temperature (ºC)	Pebble maximum temperature (ºC)
$P = 2400$ MW$_t$ (8 modules)	9198	704.0	875
$P = 3600$ MW$_t$ (12 modules)	13702	703.9	936
$P = 4800$ MW$_t$ (16 modules)	18157	703.9	995

Table 5-5: Selected steady state results for uprated powers, modified PHX/DHX system with more PHX and DHX modules

2) Transient operation

LOFC transient and ATWS accident simulations were run for the three designs, giving the results provided in Tables 5-6 and 5-7.

As usual, the maximum fuel temperature remains well within the 1600°C limit for the initiation of failure of the TRISO particles. For both the LOFC and ATWS transients the increase in the outlet temperature remains below the 980ºC temperature limit of Alloy 800H. Thus it is clear that, for the low-temperature version of the PB-AHTR, large increases in the core power density are likely possible, relative to the current 2400 MWt baseline reactor design.

	Peak outlet temperature (ºC)
$P = 2400\ MW_t$ (8 modules)	738
$P = 3600\ MW_t$ (12 modules)	749
$P = 4800\ MW_t$ (16 modules)	761

Table 5-6: Peak outlet temperatures during the LOFC transient (the maximum pebbles T is always below the steady state maximum pebble temperature).

	Peak outlet temperature (ºC)	Peak pebbles temperature (ºC)
$P = 2400\ MW_t$ (8 modules)	850	975
$P = 3600\ MW_t$ (12 modules)	891	1061
$P = 4800\ MW_t$ (16 modules)	948	1140

Table 5-7: Peak outlet and peak pebbles temperatures during the ATWS transient

G. Conclusions and further outlook

The LOFC transient is very mild for both the homogeneous and annular pebble designs, with the peak core outlet temperatures never exceeding 750ºC. On the other hand, the ATWS transient has the potentiality to be more severe: the homogeneous pebble design gives an outlet temperature rise to temperatures potentially as high as 900ºC, whereas the annular pebbles design outlet reaches 850ºC. This reduced peak temperature favors the annular pebble design.

Parametric studies for the annular pebbles have shown that these maximum outlet temperatures are not very sensitive to changes in the PHX design around the baseline parameters. In particular, reducing the PHX heat transfer coefficient on the primary side by a factor of 2 translates into only a +5ºC rise of the LOFC maximum outlet temperature (to ~745ºC), and in a -5ºC fall in the ATWS maximum (to ~845ºC).

On the other hand, changes in temperature feedback have significant impact on the peak outlet temperature attainable during the ATWS accident, with a range of maximum outlet from 807ºC to 869ºC. More negative coolant temperature coefficient is more effective to decrease the outlet temperature than more negative fuel coefficient.

The low temperature version of the PB-AHTR is designed to use available, ASME-code-qualified materials. Because the LOFC and ATWS transients can cause temperature excursions above the 704°C normal core outlet temperature, the current baseline construction for high temperature components (reactor cover, hot legs, primary pumps, IHX's, PHX's) uses Alloy 800H (with a maximum ASME code temperature of 980°C) with a Hastelloy N cladding for corrosion resistance.

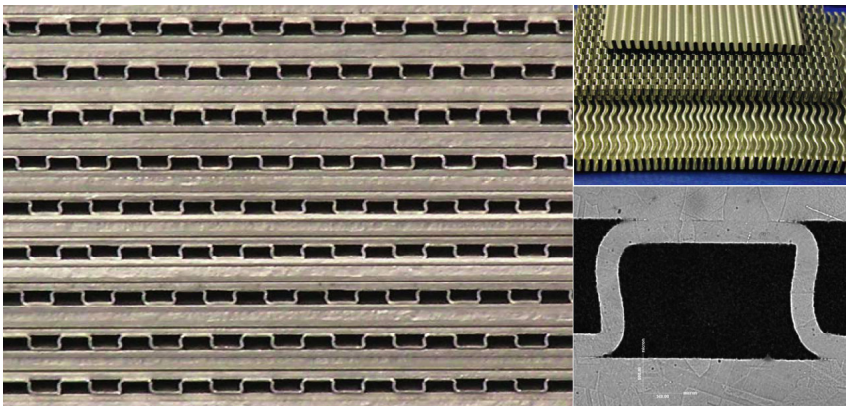

Figure 5-25: Diffusion bonded formed plate heat exchanger (FPHE) fabricated by Heatric, showing approach to fabricating an IHX heat exchanger with Alloy 800H structural material and Hastelloy N fins and cladding for plates.

Figure 5-25 shows an example construction method for a compact IHX with Hastelloy N fins and cladding of the heat exchanger plates. The Hastelloy N is ASME code qualified as a structural material only up to 704°C, but has well understood and excellent corrosion properties with clean liquid salts up to higher temperatures. Alloy 800H is code qualified for use up to 980°C, although allowable stresses are very low at

this temperature. Because Alloy 800H acts as the structural material, these high temperature components can be designed to accommodate peak temperatures for both LOFC and ATWS transients. However, it is also important to note that the effect of a failure of any of these high-temperature components would be mixing of buffer and primary salts, which would terminate any ATWS transient due to the strong neutron poisoning effect of the boron in the buffer salt.

For higher core outlet temperatures, as are required for the production of hydrogen, this preliminary study shows that this material choice is adapted to the steady state and the LOFC transient with scram, as the outlet temperature is 859ºC during steady state and rises to 883ºC during this transient. During the more severe ATWS accident, the predicted outlet temperature slightly overrides the temperature limit of Alloy 800H, with a peak outlet T of around 982ºC. Likewise, under the ATWS transient the buffer salt is driven to temperatures above the thermal dissociation temperature of the baseline sodium fluoroborate salt. Further design optimization is warranted.

Much higher powers are attainable in the annular pebble baseline version, without changing the design and the number of the PHX/DHX modules. Alloy 800H is adapted to both LOFC and ATWS transients, with outlet temperature reaching only 948ºC in the most severe case (ATWS accident with a total power of 4800 MW_t). This means that the initial choice of steady state output P = 2400 MW_t was indeed very conservative, and the current baseline PB-AHTR can handle transients starting from much higher steady state power outputs without significant design changes. This large amount of margin in the design gives the potential to reduce capital costs significantly.

Bibliography

[1] *RELAP5-3D© Code Manual, volume II: User's Guide and Input Requirements*, INEEL-EXT-98-00834 (April 2005)

[2] *RELAP5-3D© Code Manual, volume V: User's Guidelines*, INEEL-EXT-98-00834 (April 2005)

[3] *RELAP5-3D© Code Manual, Appendix A: Input Data Requirements*, INEEL-EXT-98-00834 (April 2005)

[4] P.E. MacDonald, et. al., *NGNP Preliminary Point Design - Results of the Initial Neutronics and Thermal-Hydraulic Assessments*, Idaho National Engineering and Environmental Laboratory (September 2003), INEEL/EXT-03-00870 Rev. 1.

List of tables

List of figures

Chapter 1

Chapter 2

Chapter 3

Chapter 4

Chapter 5

Annex A

Annex A: PB-AHTR design parameters

Geometric parameters

Standard pebble	
Fuel zone radius	2.5 cm
Graphite coating thickness	0.5 cm

Annular pebble	
Graphite kernel radius	1.984 cm
Fuel zone thickness	0.516 cm
Graphite coating thickness	0.5 cm

Core	
Top elevation of the active region	0 m
Active height	6.4 m
Inlet plenum height	2 m
Outlet plenum height	2.5 m
Total diameter	6.8 m
Horizontal area	36.3 m^2
Total number of pebbles	1.2 million
Bed packing fraction	60%
Pebble diameter	6 cm

Reflector	
Height	6.4 m
Inner reflector thickness	20 cm
Annulus gap thickness	0.5 cm
Outer reflector thickness	90 cm

PHX inlet/outlet pipes	
Total length	4.2 m
Total area	0.126 m^2
Number of pipes	16
Pipe diameter	10 cm

PHX modules	
Top elevation of heat transfer region	-0.53 m
Active height	3.2 m
Number of modules	8
Baffled module diameter	88 cm
Primary flow area	1.96 m^2
Number of tubes	4000

Tube diameter	2.5 m
Buffer flow area	2.94 m^2
Pitch between tubes	3.5 cm
Buffer flow hydraulic diameter	3.74 cm

Fluidic diode	
Forward head loss coefficient	1
Reverse head loss coefficient	400

Buffer tank	
Top elevation	+1.6 m
Total height	12.8 m
Horizontal area	111.2 m^2

DHX modules	
Top elevation of heat transfer region	0 m
Active height	6.4 m
Number of modules	8
Baffled module diameter	88 cm
Primary flow area	1.96 m^2
Number of tubes	4000
Tube diameter	2.5 m
Buffer flow area	2.94 m^2
Pitch between tubes	3.5 cm
Buffer flow hydraulic diameter	3.74 cm

Power distribution

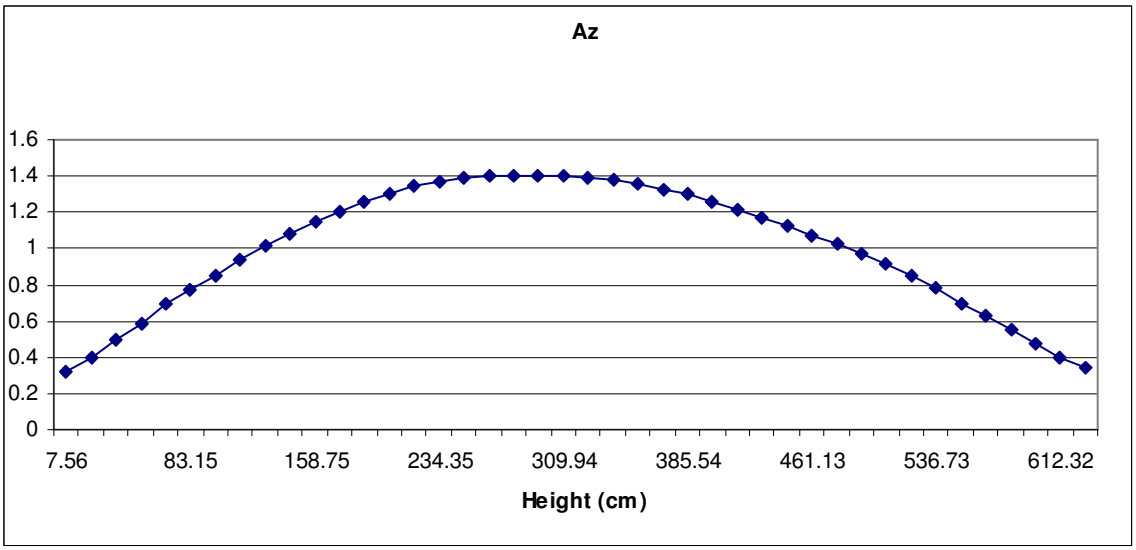

Figure A-1: Axial peaking factor

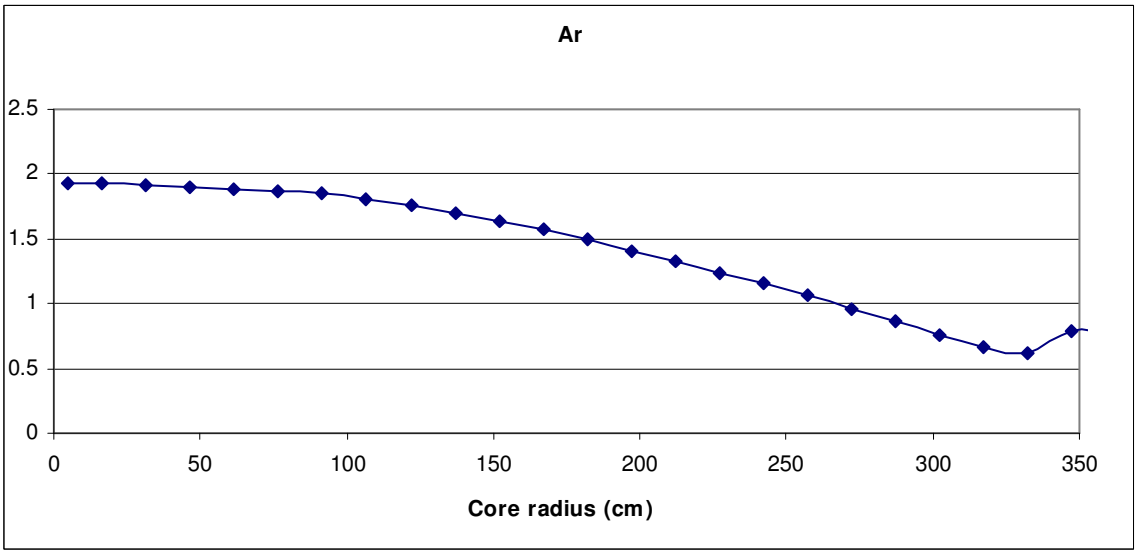

Figure A-2: Radial peaking factor

After scram decay heat curve

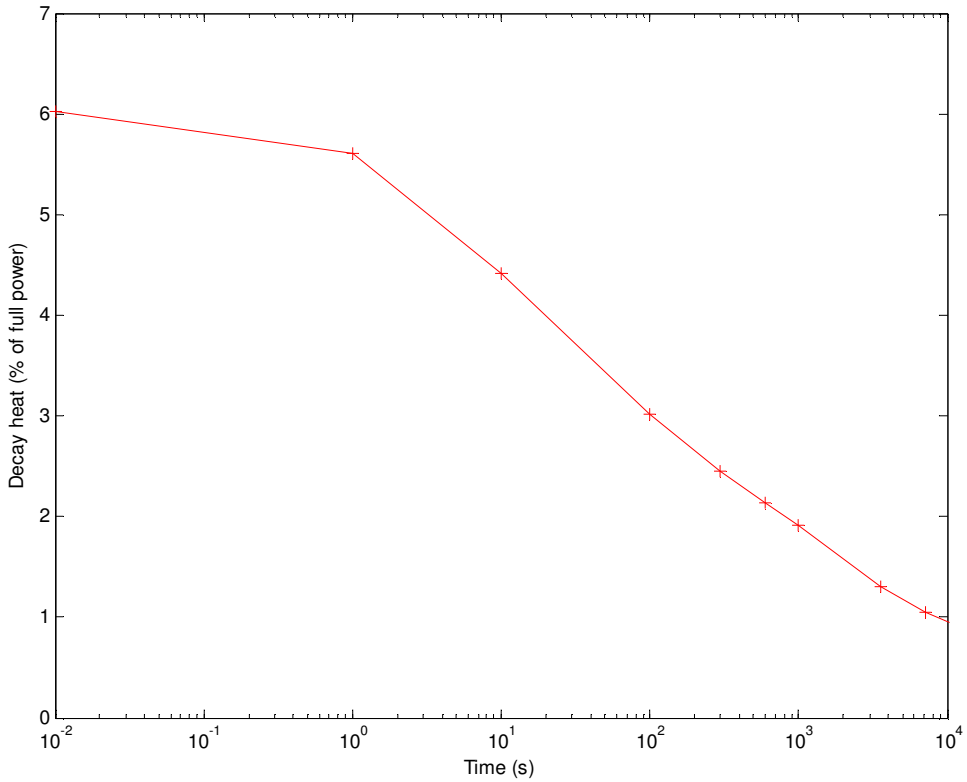

Figure A-3: Decay heat curve, from previous NGNP prismatic fuel calculation